Synthesis and Characterization of Molecular Sensors Responsive to Amino Acid Neurotransmitters for Magnetic Resonance Imaging

Dissertation

der Mathematisch-Naturwissenschaftlichen Fakultät

der Eberhard Karls Universität Tübingen

zur Erlangung des Grades eines

Doktors der Naturwissenschaften

(Dr. rer. nat.)

vorgelegt von

Đorđe Toljić

aus Vranje, Serbien

Tübingen

2024

Gedruckt mit Genehmigung der Mathematisch-Naturwissenschaftlichen Fakultät der Eberhard Karls Universität Tübingen.

Tag der mündlichen Qualifikation:	20.08.2024
Dekan:	Prof. Dr. Thilo Stehle
1. Berichterstatter:	Priv.-Doz. Dr. Goran Angelovski
2. Berichterstatter:	Prof. Dr. Martin E. Maier

Erklärung/Declaration

„Ich erkläre hiermit, dass ich die zur Promotion eingereichte Arbeit mit dem Titel: “Synthesis and Characterization of Molecular Sensors Responsive to Amino Acid Neurotransmitters for Magnetic Resonance Imaging” selbständig verfasst, nur die angegebenen Quellen und Hilfsmittel benutzt und wörtlich oder inhaltlich übernommene Stellen (alternativ: Zitate) als solche gekennzeichnet habe. Ich erkläre, dass die Richtlinien zur Sicherung guter wissenschaftlicher Praxis der Universität Tübingen (Beschluss des Senats vom 25.5.2000) beachtet wurden. Ich Amtliche Bekanntmachungen der Universität Tübingen 2015, Nr.5, S. 154 versichere an Eides statt, dass diese Angaben wahr sind und dass ich nichts verschwiegen habe. Mir ist bekannt, dass die falsche Abgabe einer Versicherung an Eides statt mit Freiheitsstrafe bis zu drei Jahren oder mit Geldstrafe bestraft wird.“

I hereby declare that the thesis I submit for my doctorate with the title: „Synthesis and Characterization of Molecular Sensors Responsive to Amino Acid Neurotransmitters for Magnetic Resonance Imaging“ is my own independent work, that I used only the sources and resources cited, and that I have clearly indicated all content adopted either word-for-word or in substance. I declare that the University of Tübingen’s guidelines to ensure good academic practice (Senate decision of 25.5.2000) have been observed. I solemnly swear that this information is true and that I have not concealed any relevant information. I am aware that making a false declaration is punishable by a fine or by a prison term of up to three years.”

Tübingen, den

Datum/Date Unterschrift/Signature

Structure and Objectives of Thesis

Recently pioneered responsive MRI CAs, comprised of a paramagnetic Gd^{3+} incorporated within a bismacrocyclic cyclen-18C6 ligand framework, were designed to reversibly convert between on/off states in response to AAs. However, their performance is limited by insufficient host sensitivity to detect biologically relevant AA neurotransmitter concentrations and lack of selectivity over the major competitive metabolite, the bicarbonate. Hence, this thesis describes efforts to address these issues with the overall aim of producing synthetic receptor for the main excitatory and inhibitory NTs, Glu and GABA, respectively.

Chapter 1 introduces the scientific topics of relevance for understanding the physics of MRI, the functioning and diversity of non-specific and stimuli-responsive MRI CAs, including small-molecule and nanosized dendrimeric constructs. It also provides a brief insight into chemical neurotransmission and a short discussion on the demands for designing MRI CAs responsive to zwitterionic amino acid transmitters. In addition, current achievements on imaging Glu and GABA by means of MR-based techniques are overviewed.

The examined bismacrocyclic CAs ligate amino acids *via* predominant Gd-$O_{carboxylate}$ interaction and multiple H-bonds between ammonium cation and the 18C6 moiety. Thus, the focus of **Chapter 2** is on chemical modification of binding sites with emphasis on the 18C6 fragment to selectively improve the affinity towards zwitterionic NTs. This approach implied the synthesis of a family of Gd-complexes with varying natures of both binding sites and revealing structure-activity relationships using various analytical techniques, including relaxometric profiling and DFT calculations.

In Chapter 2 it is revealed that recognition of AA transmitters by cyclen-18C6 chemosensors is governed by the nature of the pending arm on the 18C6 motif. Based on these findings, **Chapter 3** reports a novel design of a ditopic molecular host with improved affinity to Glu and GABA transmitters suitable for T_2/T_1w ratiometric MRI imaging. The application of a bSSFP pulse sequence on phantoms demonstrated signal enhancement for cooperatively bound Glu and GABA over hydrogen carbonate, wherein an MR signal of hydrogen carbonate remained unchanged.

After successful preparation of a synthetic host with higher selectivity for AAs over hydrogen carbonate, the focus has turned on biocompatibility improvements. Thus, **Chapter 4** describes a synthetic approach for the preparation of the first dendrimer-GBCA conjugate responsive to AAs. The previously characterized small-molecule Gd-chelate in Chapter 2 was grafted onto the end amines of the G4 PAMAM dendrimer in order to assess the impact of conjugation on binding AAs. To tune solubility at physiological pH, the conjugate was PEGylated with hydrophilic polyethylene glycol. Efficacy of the probe was evaluated in relaxometric titration with AAs and competitive metabolites, and the potential for ratiometric T_2/T_1w imaging was estimated.

Chapter 5 describes the development of a novel approach intended for ^{13}C CSI of Glu induced by the lanthanide chelate. To test the effects of lanthanide ions, a single bismacrocyclic chelator with the highest affinity to Glu and GABA (Chapter 2) was metalated with various Ln^{3+} ions, other than Gd^{3+}, to produce a series of ditopic paramagnetic receptors. The ^{13}C NMR titration of Ln-chelates performed with Gly-$^{13}C_2$ showed a stronger impact than that observed for Glu-$^{13}C_5$. The resonances of carboxylic carbons of ternary host-guest adducts exhibited the greatest signal change, presumably due to the shortest Ln-$^{13}C_{carboxylic}$ distance.

Abbreviations

AA	Amino acid
aazta	6-amino-6-methylperhydro-1,4-diazepinetetraacetic acid
ACh	Acetylcholine
BBB	Blood-brain barrier
BOLD	Blood-oxygen-level dependent
BMS	Bulk magnetic susceptibility
BPA	Blood pool agent
bs	Broad signal (NMR)
BuChE	Butyrylcholinesterase
CA	Contrast agent
Cbz	Carboxybenzyl
CD	Cyclodextrin
CE	Contrast enhanced
CEST	Chemical exchange saturation transfer
Chol	Choline
COSY	Correlation spectroscopy
CSI	Chemical shift imaging
CSF	Cerebrospinal fluid
CT	Computed tomography
D	Dendrimeric contrast agent
d	doublet (NMR)
DCC	N,N'-Dicyclohexylcarbodiimide
DIPEA	Diisopropylethylamine
DLS	Dynamic light scattering
DMF	Dimethylformamide
DOSY	Diffusion ordered nuclear magnetic resonance spectroscopy
DOTA	1,4,7,10-Tetraazacyclododecane-1,4,7,10-tetraacetic acid
DO3A	1,4,7,10-Tetraazacyclododecane-1,4,7-triacetic acid
DSS	Sodium trimethylsilylpropanesulfonate
DTPA	Diethlyenetriaminepentaacetic acid
EDTA	Ethylenediaminetetraacetic acid
EGTA	Ethylene glycol tetraacetic acid
EMA	European Medicines Agency
ENDOR	Electron-nuclear double resonance spectroscopy
Eqn	Equation
Equiv	Equivalent
ESI-MS	Electrospray ionization mass spectrometry
ESI-TOF-MS	Electrospray ionization/time of flight mass spectrometry
EXSY	Exchange Spectroscopy

FDA	U.S. Food and Drug Administration
FITC	Fluorescein Isothiocyanate
fMRI	Functional magnetic resonance imaging
G	Generation
GBCA	Gadolinium based contrast agent
Glc	Glucose
Gly	Glycine
GluCEST	Glutamate Chemical Exchange Saturation Transfer
HEPES	4-(2-Hydroxyethyl)piperazine-1-ethanesulfonic acid
HOBt	Hydroxybenzotriazole
hopo	Hydroxypyridinone
HPLC	High performance liquid chromatography
HRMS	High resolution mass spectrometry
HSA	Human serum albumin
18C6	1,10-diaza 18-crown-6 ether
CE	contrast enhanced
RF	radiofrequency
HSQC	Heteronuclear single quantum correlation
IS	Inner sphere
J	Coupling constant
MS	Mass spectrometry
LIS	Lanthanide induces shift
Ln	Lanthanide
m	Multiplet
MALDI-TOF	Matrix-assisted laser desorption/ionization-time of flight
MES	2-(H-morpholino)ethanesulfonic acid
Mmc	Methyl-7-methoxycoumarin
mMRI	Molecular magnetic resonance imaging
mPEG	Methoxy polyethylene glycol
MR	Magnetic resonance
MRI	Magnetic resonance imaging
MRS	Magnetic resonance spectroscopy
NMR	Nuclear magnetic resonance
NSF	Nephrogenic systemic fibrosis
OS	Outer sphere
PAMAM	Polyamidoamine
PBS	Phosphate-buffered saline
PET	Positron emission tomography
PPI	Polypropylene imine
PTLC	Preparative thin layer chromatography
r_1	Longitudinal relaxivity

r_2	Transverse relaxivity
RCA	Responsive contrast agent
RF	Radiofrequency
RGD	Arginine-glycine-aspartic acid
RIME	Receptor-induced magnetization enhancement
RP-HPLC	Reverse phase high performance liquid chromatography
RT	Room temperature
s	Singlet (NMR)
SAP	Square antiprismatic
SBM	Solomon, Bloembergen and Morgan (theory)
SNR	Signal to noise ratio
SPECT	Single-photon emission computed tomography
SPIO	Superparamagnetic iron oxide
SS	Second sphere
t	triplet
tacn	1,4,7-Triazacyclononane
TFA	Trifluoroacetic acid
TSAP	Twisted square antiprismatic
T_1	Longitudinal relaxation time
T_2	Transverse relaxation time
^{t}Bu	*tert*-butyl
TLC	Thin layer chromatography
USPIO	Ultra small superparamagnetic iron oxide
δ	Chemical shift

Table of Contents

1 Introduction: Molecular Sensors for Magnetic Resonance Imaging 11

1.1 mMRI: Concept and Perspectives 12
1.2 Exogenous Paramagnetic Contrast Agents 15
1.3 Paramagnetic Relaxation Enhancement 18
1.4 Responsive CAs for mMRI 28
1.5 Dendrimeric scaffolds in mMRI 36
1.6 Neurotransmitters 40

2 In-depth Study of a Novel Class of Ditopic Gd(III)-based MRI Probes Responsive to Amino Acid Neurotransmitters 45

2.1 Introduction 46
2.2 Results and Discussion 47
2.3 Conclusions 57

3 A Low-Molecular-Weight Ditopic MRI Probe for Ratiometric Sensing of Zwitterionic Amino Acid Neurotransmitters 59

3.1 Introduction 60
3.2 Molecular Design 60
3.3 Results and Discussion 61
3.4 Conclusions 67

4 Translating a Low-Molecular-Weight MRI Probe Sensitive to Amino Acid neurotransmitters into a PAMAM Dendrimer Conjugate: The Impact of Conjugation 68

4.1 Introduction 69
4.2 Molecular Design 70
4.3 Results and Discussion 71
4.4 Conclusions 75

5 Synthetic small-molecule receptors sensitive to amino acid neurotransmitters for ^{13}C NMR-based detection 77

5.1 Introduction 78
5.2 Research Design 78
5.3 Results and Discussion 79
5.4 Summary and Conclusions 82
Summary 83

6 Appendices 85

6.1 Appendix A 86
6.2 Experimental Section 86
6.3 Appendix B 110
6.4 Experimental Section 110
6.5 Appendix C 121
6.6 Experimental Section 121
6.7 Appendix D 127
6.8 Experimental Section 127
Bibliography 129

Chapter 1

Introduction: Molecular Sensors for Magnetic Resonance Imaging

Non-invasive monitoring of chemical neurotransmission is of vital importance in medical diagnostics, as the impairment in functioning of neurotransmitters is associated with a large number of neural disorders. In order to gain information at the molecular level, various imaging techniques are coupled with responsive molecular sensors to target desired neurotransmitters. These molecules transduce interactions with endogenous stimuli into a measurable signal. Among others, molecular MRI, which uses radio frequency to exploit paramagnetism of spin-active nuclei to generate a signal, is imposed as a modality of choice due to advantageous features of MRI. However, designing selective chemosensors is challenged by a plethora of competitive metabolites and unpredictability of physicochemical parameters that govern signal transduction. Therefore, development of a molecular device able to selectively recognize and report spatiotemporal patterns of desired neurotransmitter dynamics will benefit diagnosis of cerebral pathologies as well as our understanding of brain functioning.

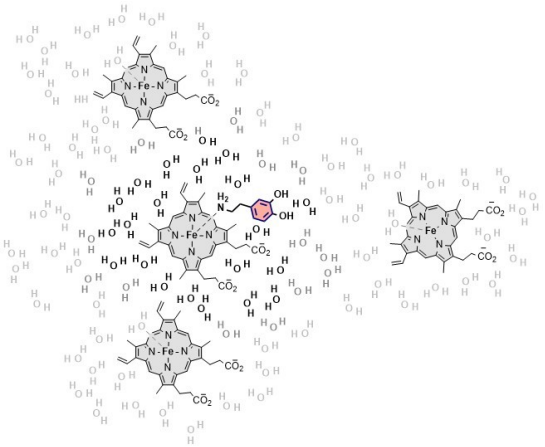

1.1 mMRI: Concept and Perspectives

Depending on the physical phenomenon, which molecular sensors exploit to produce a signal, they are classified into optical, acoustic, electrochemical, and magnetic. Owing to advantageous features of the MRI technique, magnetic probes become irreplaceable tools in modern diagnostic medicine. MRI is a *non-invasive* bioimaging modality grounded on NMR phenomena that uses spin paramagnetism to depict topological and physiological information of the body.[1-3] The conventional MRI scan generates an image contrast by measuring T_1 and T_2 relaxation times of protons across tissues, coming from water, fats, carbohydrates, proteins, and other small-molecule metabolites. Unlike the radiodiagnostic imaging modalities such as PET and SPECT, MRI excludes damaging radiation, which makes it safe for the patient. In contrast to optical and photoacoustic techniques, MRI is featured with unlimited penetration depth with extraordinarily high soft-tissue contrast. However, it suffers from low sensitivity. These limitations were addressed by administration of exogenous substances, which catalyze relaxation time of water protons. Current clinical CE MRI is non-specific, whereas CAs level up sensitivity and improve tissue specificity mainly through passive targeting.[4] Yet, alongside current applications, a further potential of mMRI is to visualize and quantify ongoing metabolic processes before the anatomical features of diseases become noticeable. To date, the application of mMRI is limited in biomedical research to facilitate investigation on e.g., gene expression[5], apoptosis[6], cell migration[7], detection of intracellular Ca^{2+} signaling[8] etc.

1.1.1 Principles of NMR Physics

The NMR phenomenon was discovered in 1946 independently by Bloch and Purcell[9, 10] represents a complex interplay between spin-active nuclei, RF radiation, and an external homogeneous magnetic field (B_0). The molecules are in constant motion, and in thermal equilibrium they display an averaged energy and no net magnetization. When immersed in the magnetic field B_0, they redistribute in energetically distinct levels, the so-called Zeeman effect (Fig. 1.1a), and precess along the z-axis, either aligned with or opposite to the B_0 vector, with the angular precession frequency (ω_0) proportional to the strength of the magnetic field [Eq. 1.1];

$$\omega_0 = \gamma B_0 \qquad [1.1]$$

where constant γ denotes the gyromagnetic ratio. The γ-value varies by atomic species, causing each type of nucleus to resonate at a specific frequency (Larmor frequency). For instance, at B_0 = 1T, the ^{1}H nuclei ($\gamma_H = 2.675\times10^8$ rads^{-1} T^{-1}) resonate at 42.6 MHz.

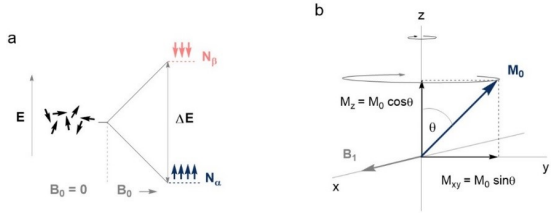

Figure 1.1. Generation of NMR signal in proton spin system. (**a**) ^{1}H polarization in the magnetic field B_0. The spin quantum number (I) of a proton is 1/2, and its magnetic quantum number has two distinct values, 1/2 and -1/2. In the absence of B_0 motion, spins are random colliding with each other having the same average energy. Upon exposure to B_0, spins absorb the energy and split into two different energy states. The α or up-spin population is aligned with the B_0 vector and lower in energy, and the β or down-spins are oriented opposite of B_0 and higher in energy. (**b**) The excess of α spins generates net magnetization (M_0). With respect to the external magnetic field, the M vector is split up in a longitudinal (M_z) and transverse (M_{xy}) component.

The ratio of spin populations can be predicted by *Boltzmann's* distribution, given for the ^{1}H nuclei in thermal equilibrium by Eq. 1.2, where N_α and N_β are low- and high-energy spin populations, respectively, ΔE is the difference between spin states, T is temperature, and k is Boltzmann's constant. The ΔE is directly proportional to the strength of the applied magnetic field, given by Eq. 1.3, where h is the Planck's constant.

$$\frac{N_\alpha}{N_\beta} = e^{\Delta E/kT} \tag{1.2}$$

$$\Delta E = E^\beta - E^\alpha = \frac{h}{2\pi}\gamma B_0 \tag{1.3}$$

If the ^{1}H spin system is exposed to a magnetic field of 2.35 T, according to Eq. 1.1, the N_α/N_β ratio corresponds to 1 000 017. The net magnetization (M_0) of magnetic moments of excess spins (N_s) is what generates a signal [Eq. 1.4]. A consequence of only a small fraction of the protons makes the NMR technique relatively low sensitivity. Magnetization is proportional to density of spins and strength of the magnetic field and inversely proportional to temperature. Furthermore, the energetic difference between spin populations given by [Eq. 1.3] falls in the range of a few μcal/mol, which is negligible compared to the thermal energy of molecules at room temperature (~600 cal/mol), owing to which MRI is a non-destructive methodology.

$$M_0 \approx \gamma^2 h^2 N_s B_0 / 4kT \tag{1.4}$$

If the same spin system is irradiated by the transverse oscillating field (B_1) with the frequency equal to the precession frequency [Eq. 1.5], they will absorb the energy tipping the M_0 into the transverse plane. This process is the resonance component in the NMR. The role of the oscillating nature of B_1 is to synchronize spins

to precess together, and the sum of their vectors is transverse magnetization (M_{xy}). Since the precession frequencies of spin-active nuclei fall within the range of radio waves (3 kHz to 300 GHz), the B_1 used to perturb bulk magnetization is also termed the RF pulse.

$$\nu = \frac{\gamma}{2\pi} B_0 \tag{1.5}$$

Interaction of bulk magnetization with RF pulses in the static magnetic field B_0 and its time decay constants are described by the Bloch equation, summarized by Eq. 1.6, where T_1 and T_2 represent longitudinal and transverse time constants, respectively. When the RF pulse is removed, the spins interact with the environment, giving away their energy until the net magnetization establishes its equilibrium magnitude M_0. This process is termed "relaxation" and is characterized by two relaxation time constants.

$$\frac{dM}{dt} = M \cdot \gamma B_0 + \frac{M_0 - M_z}{T_1} + \frac{M_{xy}}{T_2} \tag{1.6}$$

The longitudinal or spin-lattice relaxation accounts for the exponential regrowth of M_0 with B_0 with the time constant T_1, [Eq. 1.7]. It occurs when the up-spins release energy to the environment, which could be a different kind of spin-active nucleus, electron, or crystal lattice. On the other hand, the transversal component M_{xy} undergoes exponential decay with the time constant T_2 given by Eq. 1.8, implying decoherence between two spins of the same kind owing to variations in their precession frequency. Both relaxation processes are often expressed *via* relaxation rates (R_i), whereas $R_i = 1/T_i$.

$$M_z(t) = M_0 - [1 - e^{-t/T_1}] \tag{1.7}$$

$$M_{xy} = M_0\, e^{-t/T_2} \tag{1.8}$$

Due to B_0 inhomogeneity contribution to decoherence, in real systems the apparent transverse relaxation time (T_2^*) is always shorter than T_2. The relationship between them is displayed by Eq. 1.9, where the term T_{inhom} is a deviation from the ideal transverse relaxation, ΔB_0 represents the magnetic field inhomogeneity, and γ is the gyromagnetic ratio.

$$\frac{1}{T_2^*} = \frac{1}{T_2} + \frac{1}{T_{inhom.}} = \frac{1}{T_2} + \gamma \Delta B_0 \tag{1.9}$$

The magnitude of the M_0 vector (μT) is negligible compared to the strength of common clinical B_0 (> 1.5T) and is therefore measured in the transversal plane. Application of either π/2 (90°) or π (180°) RF pulse angles (θ), flips M_0 into the transversal plane, and the length of the pulse (t_p) is calculated according to Eq. 1.10; where ω_1 is the frequency of the RF pulse.

$$\theta = \omega_1 t_p \tag{1.10}$$

The M_{xy} precesses in the transversal plane, creating a small but measurable voltage on detection coils. Due to transverse relaxation, induced currents decay, also known as Free Induction Decay (FID), and are initially recorded as a function of time (t).[11] In the final NMR spectra, the time domain is translated by Fourier transform into the frequency domain (v).

1.2 Exogenous Paramagnetic Contrast Agents

When traditional MRI does not provide sufficient image clarity due to weak polarization of proton nuclei, its performances are improved by administration of exogenous CAs, which enhance contrast of an image by exploiting the differences in uptake between healthy and diseased tissues. Unlike radio diagnostic and optical imaging modalities, where the administered probes are visualized directly, in CE MRI, the effect of CAs on the signal of surrounding water protons is detected.[12] Specifically, CAs alter signals by affecting the magnetization of bulk water protons either by shortening relaxation times or by saturation transfer through chemical exchange.[13, 14] In the broadest sense, MRI CAs may be categorized according to contrast-generating mechanism into T_1 (positive) and T_2 (negative) CAs[15], and there is an additional relatively new group, which operates on the CEST principle, the so-called paraCEST agents.[16]

1.2.1 T_1-weighted CAs

Paramagnetic solutes reduce both longitudinal and transverse relaxation times, whereas the typical T_1 CAs have the r_2/r_1 ratios close to 1.[17] The T_1 CAs accelerate recovery of the M_z, where the stronger signal causes brightening on the T_1w image. Current clinical T_1 agents are mainly small-molecule chelates with MW < 1000 Da, consisting of a paramagnetic ion in-cage by a multidentate polyaminocarboxylate with relaxivity values (3-7 T) falling in the range 3-5 $mM^{-1}\,s^{-1}$.[18] Predominantly clinical T_1 CAs incorporate the paramagnetic Gd^{3+} ion, and the less common are the Mn^{2+}-based complexes.

Gd^{3+} is a trivalent lanthanide ion with 7 unpaired electrons, a large magnetic moment (7.9 μB), and a long electronic relaxation time (9^{-10} s), which makes it an effective catalyst for relaxing water protons.[13, 19] The property of GBC of vital importance for clinical application is their *in vivo* stability, which is estimated based on their kinetic and thermodynamic properties.[20, 21] The kinetic inertness presents the rates of chelation/dechelation between the ligand and the metal ion. On the other hand, thermodynamic stability refers to equilibrium concentrations of a complex on one side and a free metal ion and ligand on the other. Stability *in vivo* is important, as the free Gd^{3+} can mimic the role of Ca^{2+} in the signaling pathways due to a similar ionic radius, causing serious damage.[22] Furthermore, the median lethal dose (LD_{50}) of free Gd^{3+} observed in mice is 0.2 mmol/kg.[23] The stability of GBCAs is associated with the type of chelator, and according to their chemical structures, they are classified into linear and macrocyclic. The macrocyclic derivatives are more stable, while linear chelates are more prone to transmetallation with endogenous ions (Mn^{2+}, Cu^{2+}, Ca^{2+}, Fe^{2+} and Zn^{2+}).[24] In general, stability of clinically approved

GBCAs, by EMA and FDA, with -log K_d of 17 - 25 renders their biological inertness.[25, 26] These GBCAs are mainly derived from macrocyclic H_4dota-derived chelator in which the ligand occupies eight out of nine coordination sites on the Gd^{3+} ion, leaving a single vacant space for the coordination of water (Fig. 1.2). On the other hand, the linear analogues are based on H_5dtpa derivatives.[27]

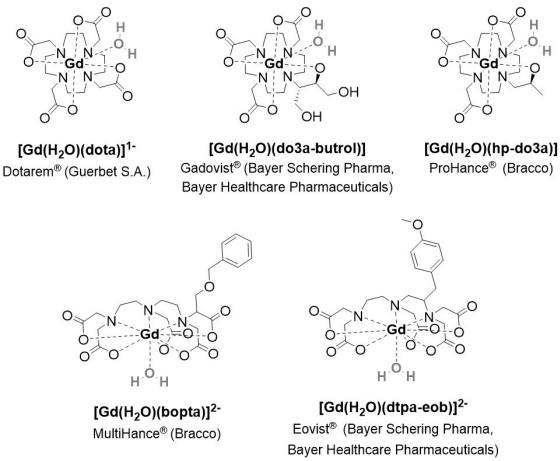

Figure 1.2. Clinically approved GBCAs by the EMA.

The paramagnetic Mn^{2+} has five unpaired electrons and is less efficient in relaxing water protons compared to Gd^{3+}. However, it has a low r_2/r_1 ratio, which makes it a less toxic alternative to Gd^{3+} ion.[28] In biological systems Mn^{2+} mimics the role of Ca^{2+}, entering neurons through the voltage-gated ion channels and moving along the axons. Owing to this property, it was previously administered as the $MnCl_2$ solution to study functional connectivity patterns *via* the so-called manganese-enhanced MRI (MEMRI).[29-31] However, these investigations are abandoned, as it was found that it accumulates in the striatum, causing death of neuronal tissue.[32, 33] The manganese-based CAs could be classified into small molecule CAs and nano-sized particles.[34] Although it is a biogenic element, a serious disadvantage of Mn^{2+} is a lack of ligands, which could yield complexes with sufficient kinetic inertness and thermodynamic stability and at the same time provide free coordinating place(s) for water molecules. While the gastrointestinal CAs $MnCl_2$ (LumenHanace®) used for oral administration is still in clinical use, the liver-specific **Mn(dpdp)** (Teslascan®), shown in Fig. 1.3, was withdrawn from the market as it was found that it mimics the activity of the enzyme manganese superoxide dismutase (MnSOD), which regulates ROS and RNS levels.[35] For the Mn^{2+}, that would be at best a six-dentate ligand, which is, however, prone to transmetallation with competitive ions e.g. Zn^{2+}.[36] A promising ligand that displayed a fine balance between coordination chemistry requirements and stability properties has been reported by Gale *et al.*, who designed a rigidified

PyC3A ligand from *N*-picolyl-*trans*-1,2-diaminocycloheane backbone.[37] The resulting Mn-PyC3A exhibited relaxivity properties similar to that of Gd(dtpa) and an elimination half-life time of 40.1 $\pm$ 3.1 min, which is comparable with that of clinical GBCAs.

The clearance half-time of low-molecular-weight GBCAs from the body occurs *via* the renal system and is an average of about 80 min.[38] These chelates are considered to be the first-generation CAs.[20] In order to prolong their retention time, the second-generation CAs (also known as the BPAs) were developed, which are designed to bind plasma proteins.[39] One representative example is the **MS-325**, which binds HSA through non-covalent interactions and is used for the diagnosis of aortoiliac occlusive disease (Fig 1.3).[40] The extended retention time makes them useful for MR angiography.

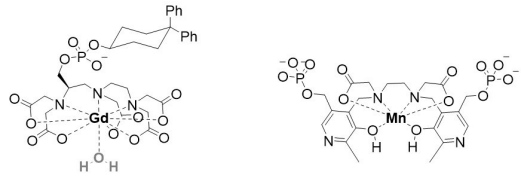

MS-325
ABLAVAR® (Lantheus Medical Imaging, Inc.)

[Mn(dpdp)]$^{4-}$
Teslascan® (GE Healthcare AS)

Figure 1.3. Chemical structures of **MS-325** and **[Mn(dpdp)]$^{4-}$**.

All the clinical GBCAs are extracellular agents; they do not cross intact biological barriers or cell membranes and are relatively safe for application as they are rapidly excreted *via* the urinary tract. The recommended dosages by EMA are the lowest amounts necessary to provide sufficient image enhancement, which is usually around 0.6 mM for GBCAs. However, the application is restricted to the patients with healthy kidney function, as it is found that patients suffering from heavy renal insufficiency develop a rarely occurring pathological state known as nephrogenic systemic fibrosis (NFS), which could be lethal.[41-43] Moreover, it was recently discovered that repetitive administration of GBCAs, in patients with healthy renal function, leads to Gd deposition in the brain.[44] The Gd distribution occurs either through a disrupted BBB or blood-CSF barrier and is correlated with chelate stability.[45-48] However, there is no clear evidence that confirms that the accumulation of gadolinium damages brain functionality.[49] To prevent the potential risk associated with Gd accumulation, in 2017 the EMA, banned most of the linear GBCAs and restricted the usage of certain macrocycles.

1.2.2 T_2-weighted CAs

T_2 or susceptibility CAs induce field inhomogeneities, reducing water proton signal intensity, which appears as darkening in T_2w and T_2^*w images.[50] The typical r_2/r_1

ratio of these CAs is > 20, and with its increase, the contrast efficacy is better.[51] In terms of chemical structure, they are manly superparamagnetic nanocomposites made of an iron oxide core, magnetite (Fe_3O_4) or its more stable form maghemite (γ-Fe_2O_3), and coated with stabilizing materials, such as PEG, silicates, PVC, starch, liposomes, dextran, or other polymers, in order to improve their biocompatibility and allow further functionalization.[52-55] According to the size of particles, they are categorized into superparamagnetic iron oxide (SPION) with diameters > 50 nm and ultra-small superparamagnetic iron oxide nanoparticles (USPIONs) with diameters < 50 nm, including their subclasses, the cross-linked (CLIO) 3 - 5 nm and monocrystalline (MION) 10 - 30 nm. The typical relaxivity of T_2 agents exhibits more than 100 mM^{-1} s^{-1} and is directly correlated with the size of particles and thickness of the coating layer. Unlike the T_1 Cas, whose detections require metal concentrations > 10 μM, the T_2 CAs allow detection at < 10 nM concentrations of nanoparticles.

The advantageous features of these particles are very high T_2 (T_2^*) relaxivity and non-toxicity for *in vivo* application since they can be degraded, whereas iron can be used by the body. However, a long-term deposition, over several months,[56] in certain organs such as the spleen and liver can cause fibrosis and inflammation. Biodistribution of IONPs is governed by their size and surface charge.[57] This is exemplified by SPIONs greater than 200 nm, which predominantly concentrate in the liver and spleen,[58] whereas USPIOs mainly invade lymph nodes.[58, 59] SPIONs are suitable for imaging cancerogenic cells and solid tumors as they accumulate through the enhanced permeation and retention effect.[60, 61] Their further functionalization towards improved sensitivity may be achieved through the introduction of a targeting ligand. This strategy is exemplified by Sun and co-workers,[62] who coupled USPIO to cyclic-Arg-Gly-Asp-D-Tyr-Lys peptide (cRGDyK) *via* 4-methylcatechol (4-MC) to obtain BPA with an overall diameter of ~ 8.4 nm (Fig. 1.4). The resulting **c(RGDyK)-MC-Fe_3O_4** displayed improved affinity to transmembrane receptor, $\alpha_v\beta_3$-integrin, which is overexpressed in tumour cells, providing a decrease of tumor MRI signal for 40%.

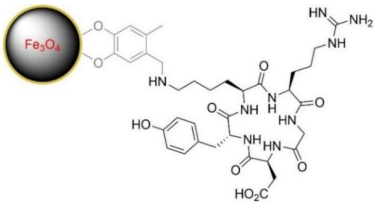

Figure 1.4. Chemical structure of the **c(RGDyK)-MC-Fe_3O_4**.

1.3 Paramagnetic Relaxation Enhancement

The paramagnetic solutes in aqueous solution undergo molecular motions that induce fluctuations of a local magnetic field with frequency and amplitude suitable

for water proton T_1 and T_2 relaxation to their magnetic equilibrium state. The overall relaxation rate enhancement $(1/T_i)_{obs}$ that bulk water protons experience is contributed by paramagnetic $(1/T_i)_p$ and diamagnetic $(1/T_i)_d$ terms [Eq. 1.11].

$$(1/T_i)_{obs} = (1/T_i)_d + (1/T_i)_p \; ; \quad i = 1, 2 \tag{1.11}$$

The diamagnetic term is an intrinsic property of media/tissues, reflecting the nature of protons. For instance, water relaxation time in the body is very long; however, due to interactions with endogenous paramagnetic small molecules such as ferritin[63] or macromolecules such as lipids and proteins[64], not all the water protons display the same relaxation values.[65] This feature of body water is responsible for the endogenous contrast. On the other hand, PRE is the result of interactions between unpaired electrons of the paramagnetic center and the nuclear dipole of water protons. The efficacy of GBCAs to catalyze relaxation rates of bulk water protons normalized to the concentration of Gd^{3+} is relaxivity (r_i, $mM^{-1}s^{-1}$), expressed by Eq. 1.12.

$$r_{i,\mathrm{p}} = \frac{(1/T_i)_p}{[\mathrm{Gd}^{3+}]}; \quad i = 1, 2 \tag{1.12}$$

In a general sense, the T_1 relaxation time of body water is 5 to 20 times longer compared to T_2, resulting in a much more pronounced effect of CAs on T_1. A suitable example is the impact of 1 mM Gd(dota) on cortical gray matter, which increases the endogenous values for T_1 and T_2 by 3.6 s^{-1} and 4.3 s^{-1}, corresponding to rate enhancements of 428 and 42%, respectively.[66] The proximate water molecules, which effectively exchange energy with CAs and contribute to relaxivity, as depicted in Fig. 1.5, originate from the following: (1) inner sphere (IS), (2) second sphere (SS), and (3) outer hydration sphere (OS).[67]

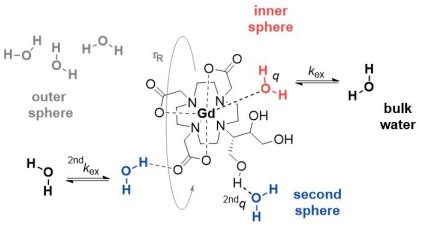

Figure 1.5. Schematic presentation of interactions between **Gd(do3a-butrol)** and water molecules**.** In the inner sphere, water molecules are directly coordinated to paramagnetic Gd^{3+}. The outer sphere is represented by the non-bound water molecules, which diffuse in the vicinity of the paramagnetic chelate. In the intermediate, the second hydration shell, water molecules are loosely bound to charged groups on the ligand via hydrogen bonds. In each hydration sphere, relaxation occurs through different mechanisms that are governed by various physicochemical parameters involving (1) the number of water molecules in IS and SS, q and q^{2nd}, respectively; (2) different electronic relaxation rates; (3) time-correlation functions that describe dynamics of CAs–OH_2 interactions, a so-called residence lifetime of

bound water molecules (τ_M), (often expressed as the water exchange rate, $k_{ex} = 1/\tau_M$); and (4) rotational diffusion of CAs (τ_R).

Their contributions to relaxation rates and the corresponding relaxivities are summarized in Eqns. 1.13 and 1.14, respectively.

$$(1/T_i)_p = (1/T_i)^{IS} + (1/T_i)^{SS} + (1/T_i)^{OS};\ i = 1, 2 \tag{1.13}$$

$$r_i = r_i^{IS} + r_i^{SS} + r_i^{OS};\ i = 1, 2 \tag{1.14}$$

The inner-sphere contribution to the overall r_1 relaxivity of the clinically approved GBCAs is approximately 60%, whereas the rest comes from the second and outer hydration spheres.[68]

1.3.1 Inner-Sphere Mechanism

The inner-sphere relaxivity (r_i^{IS}) originates from coordinated water molecules, which undergo chemical exchange with the bulk solvent, transmitting the relaxation effect.[69, 70] The two-pool exchange is given by equations 1.15 and 1.16, where P_m is the mole fraction of water coordinated directly to paramagnetic ion (=[Gd^{3+}]/[H_2O], concentration of water is 55.5 mM), T_{1m} and T_{2m} are the T_1 and T_2 and subscript "m" refers to the shift or relaxation rate of solvent molecule, q is the number of inner-sphere waters, τ_M is the residence lifetime of bound water molecules in the innersphere, and $\Delta\omega$ is the paramagnetic shift difference between the diamagnetic reference and the paramagnetic complex.

$$r_1^{IS} = \frac{P_m q}{T_{1m} - \tau_M} \tag{1.15}$$

$$r_2^{IS} = P_m q \frac{1}{\tau_M}\left(\frac{T_{2m}^{-1}(\tau_M^{-1} + T_{2m}^{-1}) + \Delta\omega_m^2}{(\tau_M^{-1} + T_{2m}^{-1})^2 + \Delta\omega_m^2}\right) \tag{1.16}$$

The overall inner-sphere relaxivity is, according to the Solomon-Bloembergen-Morgan (SBM) theory[71, 72], split into contributions originating from dipolar or through-space (dd), scalar or contact (sc), and Curie-spin (cs) interactions, as summarized by Eq. 1.17.

$$\frac{1}{T_{1m}} = \frac{1}{T_i^{dd}} + \frac{1}{T_i^{sc}} + \frac{1}{T_i^{cs}} \tag{1.17}$$

As illustrated by Eq. 1.15, when $\tau_M \ll T_{1m}$ the r_1^{IS} is directly proportional to the number of coordinated water molecules. At the clinically relevant fields (> 1.5 T), the longitudinal relaxation enhancement ($1/T_{1m}$) of GBCAs is contributed by only dipolar interactions as illustrated by SBM Eq. 1.18, whereas the scalar term is neglected due to long Gd–H_{water} distance.[73, 74] Here, μ_B is the Bohr magneton, g is the electron g tensor (for Gd^{3+}, g = 2), μ_0 is the permittivity of vacuum, r_{GdH} is the

effective distance between the gadolinium electron spin and the water proton nucleus, S is the electron spin quantum number (for Gd^{3+}, S = 7/2), ω_H (rad/s) is the proton resonance frequency, ω_S ($\omega_S = 685\omega_H$) is the Larmor frequency of the gadolinium electron spin, τ_{c1} and τ_{c2} are the overall correlation times of dipolar proton spin-electron couplings, and is the hyperfine Gd–H_{water} coupling constant.

$$\frac{1}{T_{1m}} = \frac{1}{T_1^{dd}} = \frac{2}{15}\left(\frac{\mu_0}{4\pi}\right)^2 \frac{\mu_B^2 \gamma_H^2 g^2 S(S+1)}{r_{GdH}^6}\left[\frac{7\tau_{c2}}{1+\omega_S^2\tau_{c2}^2} + \frac{3\tau_{c1}}{1+\omega_H^2\tau_{c1}^2}\right] \quad (1.18)$$

The dependence of previously mentioned physicochemical parameters on each of the relaxation mechanisms is expressed through time-dependent correlation functions. Accordingly, the dipolar mechanism is modulated by the reorientation of Gd–H_{water} vector, expressed by the reorientational correlation time, water exchange rate ($1/\tau_M$), longitudinal and transverse electron spin relaxation time, expressed by Eq. 1.19. In addition, to achieve the maximal relaxivities as predicted by the SBM theory (>100 mM^{-1} s^{-1}) the inverse of the overall correlation time term has to match the proton Larmor frequency ($1/\tau_c = \omega_0$).[74]

$$\frac{1}{\tau_{ci}} = \frac{1}{\tau_R} + \frac{1}{T_{ie}} + \frac{1}{\tau_M};\ i = 1,2 \quad (1.19)$$

The transverse relaxation enhancement term ($1/T_{2m}$), is contributed by all three mechanisms, as given by Eq. 1.20.

$$\frac{1}{T_{2m}} = \frac{1}{15}\left(\frac{\mu_0}{4\pi}\right)^2 \frac{\mu_B^2 \gamma_H^2 g^2 S(S+1)}{r_{GdH}^6}\left[\frac{3\tau_{c1}}{1+\omega_H^2\tau_{c1}^2} + 4\tau_{c1}\right] + \frac{S(S+1)}{3}\left(\frac{A}{\hbar}\right)^2 [\tau_{sc}] + \frac{1}{15}\left(\frac{\mu_0}{4\pi}\right)^2 \frac{\omega_H^4 \mu_B^4 \gamma_H^2 g^4 S(S+1)}{(3k_B T)^2 r_{GdH}^6}[4\tau_{4cs}] \quad (1.20)$$

The scalar term depends only on water residence time τ_M and electron relaxation rates. Owing to the relatively weak bond and consequently long Gd–H_{water} distance, the resulting effect is small. On the contrary, the scalar term provides a more significant contribution in the case of Fe^{3+} and Mn^{2+} CAs.

$$\frac{1}{\tau_{sc}} = \frac{1}{T_{ie}} + \frac{1}{\tau_M};\quad i = 1,2 \quad (1.21)$$

According to Gueron, the Curie-spin relaxation is the result of dipolar interaction between a large static magnetic moment (at ≥ 7T, due to strong magnetization of CAs) coming from CAs ($Ln^{3+} \neq Gd^{3+}$) electrons and the dipole of water protons. The CAs with diameters larger than 3 nm are negligible compared to dipolar and scalar contributions. On the contrary, for the CAs smaller than 3 nm, Curie-spin relaxation is the dominant mechanism. It is a function of τ_M and τ_R but independent of electronic relaxation rates.

$$\frac{1}{\tau_{cs}} = \frac{1}{\tau_{\mathrm{R}}} + \frac{1}{\tau_{\mathrm{M}}} \tag{1.22}$$

The electron spin relaxation rates depend on macroscopic parameters such as temperature and magnetic field.[75] The relation for the field dependence is described by the modified Solomon-Bloembergen-Morgan theory, which interprets spin relaxation rates $(1/T_{ie})^{\mathrm{ZFS}}$ in terms of a zero-field-splitting (ZFS) interaction[71, 76], given by Eqns. 1.23 and 1.24:

$$\left(\frac{1}{T_{1e}}\right)^{\mathrm{ZFS}} = 24\Delta^2\left(\frac{\tau_v}{1+\omega_{\mathrm{S}}^2\tau_v^2} + \frac{4\tau_v}{1+4\omega_{\mathrm{S}}^2\tau_v^2}\right) \tag{1.23}$$

$$\left(\frac{1}{T_{2e}}\right)^{\mathrm{ZFS}} = 12\Delta^2\left(\frac{5\tau_v}{1+\omega_{\mathrm{S}}^2\tau_v^2} + \frac{2\tau_v}{1+4\omega_{\mathrm{S}}^2\tau_v^2} + 3\right) \tag{1.24}$$

where Δ^2 is the mean-squared ZFS energy, and τ_v is the correlation time for the modulation of ZFS interactions. The given equations are derived for GBCAs (S=7/2).

1.3.2 Outer-Sphere Contribution

The SBM theory cannot interpret interactions between paramagnetic nuclei and water molecules from the outer hydration shell. Instead, this contribution is described by the diffusion-controlled model established by Hwang and Freed[77, 78] according to which the outer-sphere contribution (r_1^{OS}) comes from closely diffusing water molecules[74] [Eqns. 1.25 and 1.26];

$$r_1^{OS} = \frac{32\pi}{405}\left(\frac{\mu_0}{4\pi}\right)^2 \frac{\gamma_I^2\gamma_S^2\hbar^2 N_{\mathrm{A}}[\mathrm{CA}]}{1000aD} S(S+1)[3J_{OS}(\omega_{\mathrm{S}}) + 7J_{OS}(\omega_{\mathrm{H}})] \tag{1.25}$$

$$r_2^{OS} = \frac{32\pi}{405}\left(\frac{\mu_0}{4\pi}\right)^2 \frac{\gamma_I^2\gamma_S^2\hbar^2 N_{\mathrm{A}}[\mathrm{CA}]}{1000aD} S(S+1)[2 + 1.5J_{OS}(\omega_{\mathrm{S}}) + 6.5J_{OS}(\omega_{\mathrm{H}})] \tag{1.26}$$

where J_{OS} is the spectral density function that describes electronic-relaxation dependence [Eq. 1.27]; where Re stands for the "real part of".

$$J_{OS}(\omega_{\mathrm{S}}) = \mathrm{Re}\left\{\frac{1 + \frac{1}{4}\left(i\omega\tau_{\mathrm{D}} + \frac{\tau_{\mathrm{D}}}{T_{\mathrm{ie}}}\right)^{1/2}}{1 + \left(i\omega\tau_{\mathrm{D}} + \frac{\tau_{\mathrm{D}}}{T_{\mathrm{ie}}}\right)^{1/2} + \frac{4}{9}\left(i\omega\tau_{\mathrm{D}} + \frac{\tau_{\mathrm{D}}}{T_{\mathrm{ie}}}\right) + \frac{1}{9}\left(i\omega\tau_{\mathrm{D}} + \frac{\tau_{\mathrm{D}}}{T_{\mathrm{ie}}}\right)^{3/2}}\right\};\ i = 1,2 \tag{1.27}$$

This approach omits the ligand-bound waters (second sphere) and is correlated by the relative translational diffusion time τ_{R}, which depends on diffusion coefficients of CA and water molecules D and the distance of their closest approach a, as shown by Eq. 1.27.[74]

$$\tau_{\mathrm{D}} = \frac{a^2}{D} \tag{1.28}$$

The OS contribution makes a significant impact on non-hydrated or weakly hydrated small-molecule CAs. Peters and co-workers investigated the OS contribution on a series of Ln(III) complexes with q = 0.[79] The relaxivity contributions coming from different hydration spheres were measured for Ln^{3+} chelates of H_4dotp derivatives with the following pending arms: phosphinic (H_4dotp^{H}), hydroxymethylphosphinic (H_4dotp^{hm}), ethylphosphinic (H_4dotp^{Et}), phosphonate ethyl monoester (H_4dotp^{OEt}), and butyl monoester (H_4dotp^{OBu}). The $1/T_1$ NMRD profiles evidenced the OS contribution in greater than 60%.

1.3.3 Second Sphere Contribution

The strong paramagnetism of the Gd^{3+} affects water molecules beyond the inner sphere. When the Gd–H_{water} distance is between 3 and 5 Å, these waters are assigned to the second hydration shell.[80] The second-sphere contribution originates from the water molecules transiently bound to the ligand through hydrogen bonds and exchangeable protons on ligand sites. Their residence time is 20 - 30 ps, and as they tumble together, they are exposed to the influence of a fluctuating magnetic field, resulting in dipolar electron-spin relaxation. The physicochemical parameters that govern relaxation enhancement may be well described by the SBM theory, summarized by Eq. 1.28; where q_j^{SS} is the number of water molecules, T_{ij}^{SS} are the electronic longitudinal and transverse relaxation times, and τ_{mj}^{SS} is the residence lifetime of coordinated water molecules.

$$r_1^{\mathrm{SS}} = \frac{10^{-3}}{55.55} \sum_{j=1}^{\mathrm{M}} \frac{q_{\mathrm{j}}^{\mathrm{SS}}}{T_{1j}^{\mathrm{SS}} + \tau_{\mathrm{m}j}^{\mathrm{SS}}} \tag{1.28}$$

In small-molecule CAs, the r_1^{SS} contribution is usually small, owing to long distances between paramagnetic ions and water molecules and short water lifetimes. Increasing the quantity and residence time of waters through binding with hydrogen-bond acceptors installed in the vicinity of the paramagnetic center, the SS contribution may be significantly increased.[81] Caravan and co-workers carried out a study on the Gd(dota) *bis*-amide CA model where they replaced amide methyl substituents for hydrogen bond acceptors, finding out that carboxylate, phosphonate, and phosphonate esters notably prolonged the residence time of waters in the SS.[82] Substitution of acetates in Gd(dota) with phosphonates gave $[Gd(dotp)]^{5-}$, the so-called outer-sphere complex, where binding of water directly to the Gd^{3+} ion is prevented due to stereo-electronic obstacles.[79] This system exhibited an r_1 of 3.5 mM^{-1} s^{-1} with a contribution from SS of 40%. A similar observation was noticed in Gd-complexes derived from pyclen H_4pcp2a and H_6p-dtpa ligands.[83, 84] Functionalization of $[Gd(dotp)]^{5-}$ with fatty acid chains and further conjugation to HSA led to a more pronounced SS relaxivity.[85] A different approach to improve relaxivity *via* SS was illustrated by Botta *et al.,* who used a Gd(dota-mono-amide) complex where the carbonyl of the propyl amide pendant established a 5-ring

chelate with a Gd^{3+} ion.[86] The high steric demands left the inner sphere non-hydrated; however, it exhibited relatively high relaxivity, arising from the rapid exchange of waters bound to the NH group of the amide.

1.3.4 Hydration number

As previously mentioned, hydration number is the number of water molecule(s) coordinated to the paramagnetic ion. It is a physicochemical property of a complex independent of magnetic field strength. All current clinically approved CAs are monohydrated, displaying low relaxivities (4–5 mM^{-1} s^{-1}) compared to values predicted by the SBM theory. The inner-sphere relaxivity is directly proportional to *q,* and therefore, relaxivity enhancement could be achieved by increasing the number of bound waters. However, this requires reduction of ligand denticity, which comes at the expense of thermodynamic stability and kinetic inertness. This dependence is illustrated by comparing Gd-complexes derived from H_4dota ligand with its hexa- and heptadentate analogues. The eight-coordinated Gd^{3+} ion in **$[Gd(H_2O)(dota)]^-$** accommodates a single water molecule in the apical position, providing r_1 of 4.3 mM^{-1} s^{-1} and the highest thermodynamic stability of all clinically approved GBCAs with log *K* of 25 (20 MHz, 25°C).[87-89] An analogous chelate with one acetate arm less is **$[Gd(H_2O)_2(do3a)]$** which displayed increased relaxivity of 6.2 mM^{-1} s^{-1} and relatively high stability of 18.7; however, it undergoes interactions with endogenous anions.[90] The observed relaxivity enhancement originates from the second and outer sphere (50%). Further comparison with **$[Gd(H_2O)_3(do2a)]^+$**, with three waters in the inner sphere, r_1 of 6.5 mM^{-1} s^{-1} and very low stability, reveals the limiting impact of factors other than *q*-value.

Another issue associated with $q \geq 2$ complexes is the quenching effect, implying water displacement by endogenous anions (hydrogencarbonate, phosphate, etc.) or negatively charged side arms of amino acids in proteins. This issue has been addressed by the development of a few new classes of heptadentate ligands, which provided *bis*-hydrated complexes and yet preserved thermodynamic stability comparable to that of Gd(dota) (Fig. 1.6). Interestingly, their Gd-chelates do not form ternary adducts with anionic metabolites.[91] Among them are those derived from the pyridine-containing triaza macrocycle triacetate **(H_3pcta)** ligand, whose Gd-complex displayed a r_1 of 6.9 mM^{-1} s^{-1} and log *K* equal of 20.1.[92] Its high relaxivity is assigned to two coordinated waters, and high thermodynamic stability is the result of ligand rigidification due to the pyridine moiety. Substitution of acetate in the *trans* position to the pyridine moiety with the methylenephosphonate arm leads to the **H_4pcp2a** ligand, which the Gd complex shows improved r_1 (8.3 mM^{-1} s^{-1}) and log *K* (23.4).[83] The relaxivity boost is assigned to the improved fast water exchange rate and larger second hydration sphere. The Aime group introduced the heptadentate 6-amino-6-methyperhydro-1,4-diazepinetetraacetic acid **(H_4aazta)** ligand, which Gd-chelate reaches the r_1 value of 7.1 mM^{-1} s^{-1} with log*K* of 20.2.[93] Although **the $[Gd(H_2O)_2(aazta)]^-$** does not undergo transmetallation with ten-fold concentrations of Zn^{2+}, Ca^{2+}, and Mn^{2+}, it is kinetically more labile than GBCAs, due to which it is not viable for clinical application. Another promising design is *tris*-hydroxylpiridinone **(H_3tren-Me-2,3-hopo)**, developed by Raymond and co-workers.[94] Unlike the

previous ligands, here the coordinating groups are oxygens, which Gd complexes exhibited remarkably high r_1 (10.5 mM^{-1} s^{-1}), owing to longer electronic relaxation times and more optimal inner-sphere water exchange rates. On the other hand, its high conditional stability pGd of 20.3 is explained in terms of Gd^{3+} ion oxophilicity, which forms very strong Gd–O_{ligand} bonds.[95] The major drawback of **$[Gd(H_2O)_2$(tren-3,2-hopo)$]^-$**, besides its insufficient kinetic inertness, is a low solubility in biologically relevant conditions. Replacement of the ligand cap, *tris*(2-aminoethyl)amine (tren), with 1,4,7-triazacyclononane (tacn), resulted in highly soluble *tris*-hydrated **$[Gd(H_2O)_3$(tacn-3,2-hopo)$]^-$** with even higher r_1 (13.1 mM^{-1} s^{-1}).[96]

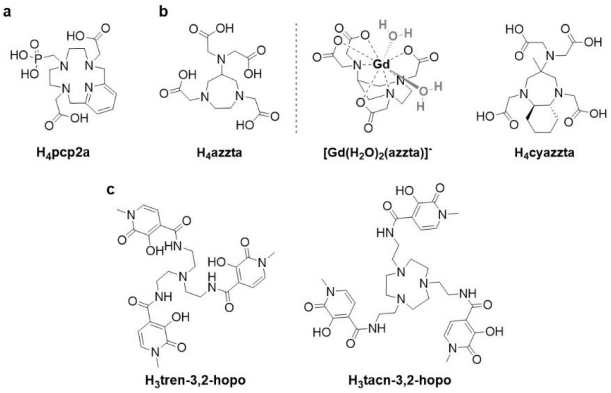

Figure 1.6. Illustration of heptadentate ligands, which provide *bis*- and *tris*-hydrated complexes.

Hydration number can be determined from the difference of luminescence lifetime decays of Eu^{3+} or Tb^{3+} analogues in H_2O and D_2O. The quenching is more effective for coordinated H_2O as the O–H oscillators absorb energy more effectively.[97, 98] This technique allows determination in the μM (indirect excitation, *via* antenna) to low mM (by direct excitation) concentration range of Ln(III)-chelates. Other less common techniques used to determine *q* value are Ln(III)-induced ^{17}O shifts measurments,[99] ^1H, and ^{17}O ENDOR spectroscopy.[100, 101] The hydration number can also be estimated by X-ray crystallography; however, the obtained values are not accurate for hydration in solution.

1.3.5 Water Exchange Rate (k_{ex})

The water exchange rate k_{ex} between the inner hydration layer and the bulk is the inverse of the coordinated water residence lifetime (τ_M). The k_{ex} limits of relaxivity are as follows: if $\tau_M < 1$ ns, the bound water molecule cannot achieve full relaxation before it detaches from Gd^{3+}, and if $\tau_M > 1$ μs, the Gd^{3+} is occupied with a relaxed water molecule for too long, preventing other water molecules from getting relaxed. For the hypothetical monohydrated CA with optimal tumbling, the SBM theory

predicts maximal values for r_1 at common clinical imaging fields (≥ 1.5 T) only if the τ_M is in the optimal range of 5 – 25 ns.[4]

The exchange rate primarily depends on the nature of the paramagnetic ion. Along the series of Ln^{3+} ions framed within the **H_3dtpa-bma** ligand, the Ln-chelates displayed from Nd^{3+} to Gd^{3+} an almost constant exchange rate, characterized by an interchange associative mechanism, and 10-fold increase to Ho^{3+} owing to a change into dissociative activation.[102] The opposite trend was observed in the case of *bis*-hydrated **Ln(pdta)** chelates, where, going on from associatively activated Gd^{3+}-chelate to dissociatively activated Yb^{3+}-chelate, the exchange rate decreased by 2 orders of magnitude, clearly suggesting dependence of metal ion size and ligand type.[103] Since that τ_M reflects the strength of $Ln–O_{water}$ bond, in the case of eight-coordinated Ln^{3+}-complexes, the water molecule dissociation can be accelerated by destabilizing this interaction. One way to achieve this is by increasing steric hindrances on the ligand. For instance, the 12-membered **Gd(dota)** displays τ_M of 122 ns, whereas replacing one acetate for a sterically more requiring propionate pending arm caused a reduction τ_M at 16.2 ns.[104] Even greater steric compression around water binding sites is observed in 13-membered **Gd(trita)** with τ_M of 3.7 ns.

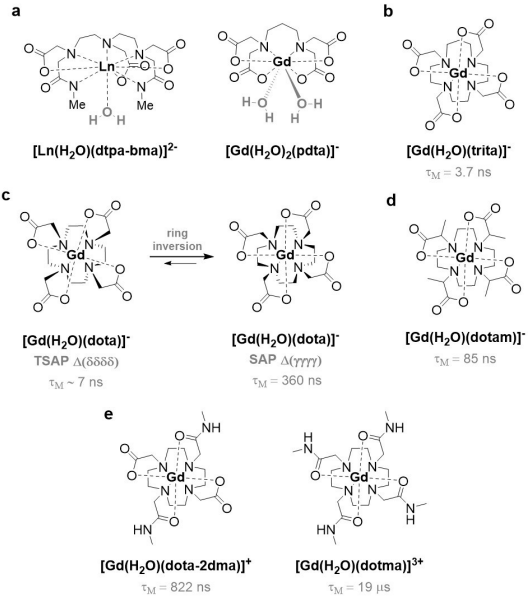

Figure 1.7. Impact of various structural features of CAs on exchange rate of inner-sphere water with the bulk.

The Gd-chelates of H_4dota-derived ligands exist in the water solution in dynamic equilibrium of two major coordination isomers, TSAP and SAP.[105, 106] In

Gd(dota), the dominant isomer is SAP (83%), in which the sterically less crowded Gd^{3+} center is more exposed for water coordination, exhibiting a slower exchange rate (360 ns) by a factor of 50 than that in TSAP, as shown by Woods and coworkers.[107] Introduction of a methyl group in the α-position of acetates gives **Gd(dotma)** favoring the TSAP isomer (81%), which is sterically more compressed, resulting in a longer Gd–O_{water} bond and consequently a more optimal τ_M of 85 ns. These strategies are useful for designing T_1w CAs since the majority of small molecule GBCAs, including the clinically approved ones, display τ_M in the 120–200 ns range, except for Omniscan (~ 1 μM).

In stark contrast to T_1w CAs, the paraCEST imaging modality requires intermediate exchange rates on the NMR time scale.[108] A straightforward way to slow exchange rates is by reducing the electron donor ability of coordinating groups, e.g., conversion of negative acetates into noncharged amides. For instance, the conversion of two negatively charged acetates in **Gd(dota)** into charge-neutral amides produces **Gd(dota-2dma)** with a lifetime of of 822 ns, whereas substitution of all four acetates results in **Gd(dotam),** which displayed a drastically longer value(19 μs).[109, 110] This is rationalized by the lesser basicity of amide oxygen that coordinatively saturates the Ln^{3+} ion to a lesser extent, which then establishes a stronger Ln – O_{water} bond, resulting in slower exchange kinetics. In addition, the exchange rates can be fine-tuned by installing electron-withdrawing groups onto amide pendants–for instance, -CN or F^-, which additionally decelerate water exchange by 324 and 148 μs, through mesomeric and inductive effects, respectively.[111] Conversely, the electron-donating groups are weakening metal-water interaction, providing faster water exchange.[110]

The water exchange kinetics are usually estimated by measuring transverse relaxation rates of water by variable-temperature ^{17}O NMR spectroscopy in the presence and absence of GBCA.[112, 113] In this experiment the transverse relaxation rates of $^{17}O_{water}$ are measured over a series of temperatures where the obtained $1/T_2$ values are proportional to the linewidth of the ^{17}O peak, which fitting derives τ_M.

1.3.6 Rotational Correlation Time (τ_R)

Reorientational correlation time is the correlation function for the Gd–O_{water} vector induced by rotational diffusion of Gd-chelate. Since it depends on magnetic fields, the optimal values predicted by the SBM theory vary with magnetic fields. In general, the ideal τ_R is equal to $1/\omega_H$ and at clinically relevant fields (≥ 1.5 T), the optimal value falls in the range 0.5–4 ns.[4] However, commercial GBCAs are fast tumbling (~100 ps), meaning that high-relaxivity CAs require longer τ_R.[74] The grounds for optimizing rotational dynamics can be rationalized by the Debye-Stokes relation, according to which the rotational diffusion coefficient (τ_D) for spherical solutes scales with molecular radius (a), which is linearly correlated to MW.[114] Accordingly, the common strategies to slow down molecular tumbling imply either conjugating a small paramagnetic CA to a macromolecule or increasing the size of a CA.[4, 68] To date, a wide array of CAs have been attached to various organic or inorganic scaffolds such as dendrimer[115], proteins, or nanoparticles[116, 117], assembled into supramolecular

polymetallic coordinative adducts[118], appended or encapsulated into micelles or liposomes[119, 120], set as a barycenter or multiple chelates attached to an organic barycenter[121, 122].

Although the attachment of small-molecule CAs to a macromolecule increases relaxivity by prolonging isotropic rotational correlation time, in very large molecules, the anisotropic motions significantly limit relaxivity.[123] The influence of molecular motions on relaxivity has been addressed by Caravan *et al*., whose study included two Gd(dtpa)-based tetramers having either one or both ends capped with a targeting vector.[124] In free forms, both probes displayed r_1 about 10 mM^{-1} s^{-1}, which, upon binding to albumin, displayed r_1, for mono- and ditopically bound tetramers, 30.7 and 41.3 mM^{-1} s^{-1}, respectively. The larger gain reflects more restricted internal motions due to ditopical binding. More recently, the same research group examined relaxivity dependence on internal rotation of the aqua ligand around Gd-O_{water}.[125] The intramolecular H-bond between the coordinated water proton and H-bond acceptors in the vicinity slows water rotation, resulting in increased relaxivity.

The first demonstration of RIME utilized **MS-325** to establish hydrophobic interactions *via* a lipophilic biphenycyclohexyl moiety to four different binding pockets in HSA with the highest K_d of 85 µM.[126] The MS-325 conjugate displayed a nearly 100-fold increase in τ_R, from 115 ps to 10.1 ns, leading to r_1 enhancement from 5.5 to 25 mM^{-1} s^{-1}. Relaxometric properties of structurally similar **MP-226** were compared to **MS-325**, where the HSA-bound form displayed reduced gain in r_1 (17 mM^{-1} s^{-1}) which is assigned to significant internal motions.[127] This is reflective of a lesser number of stabilizing interactions, as indicated by weaker K_d (110 µM). When compared to non-covalent interactions, the covalent macromolecule-CA binding provides stronger rigidification of chelates and consequently a larger boost in relaxivity. The magnitude of relaxivity change is illustrated by Wang *et al*.,[128] who synthesized and characterized a series of Gd(do3a)-derivatives conjugated to the chlorine-terminated haloalkane moiety of varying lengths (*n*-CHTGds) for covalent binding to HaloTag protein. The one with optimal chain length (**2-CHTGd**) underwent an $r_1$change from 3.8 $mM^{-1}s^{-1}$ to 22.0 $mM^{-1}s^{-1}$, indicating strong rigidification of the protein-anchored probe. Although more efficient, the covalent attachment is less desirable, as it may lead to more pronounced toxicity due to the high chance of gadolinium ion dissociation.

1.4 Responsive CAs for mMRI

Responsive CAs alter MRI signal intensity upon interaction with specific biomarkers from their microenvironment, underscoring biological processes at the molecular level.[129-131] In a mechanistic sense, the receptor interactions with stimuli induce structural changes on the receptor, which changes parameters that determine relaxivity. Strategies for activating CAs in response to stimuli are mainly grounded on variations of rotational correlation time, hydration number, and water exchange rate. These molecular sensors are in literature frequently referred to as activable or smart CAs (SCAs).[132] This chapter highlights notable strategies reported so far to activate response mechanisms of CAs.

1.4.1 τ_R-modulation

The CAs activated by tumbling rate imply a change in rotational dynamics of CAs in response to stimuli with respect to diffusion of a solvent.[126, 133-135] In this regard, the most common strategy of small-molecule CAs is through assembly into a larger supramolecular adduct. An elegant activation approach of this type has been put forward by Parac-Vogt and coworkers.[136] They designed a probe containing Gd(dtpa) and a phenanthroline chelator, which self-assemble in the presence of Fe^{2+} into a tetranuclear heterometallic self-assembled metallostar compound where the Gd-chelate tumbles with a tumbling rate of aggregate, producing an r_1 increase from 3.9 to 9.5 $mM^{-1}s^{-1}$ per gadolinium (Fig. 1.8a). A different type of assembly-triggered activation involving adducts with poor water solubility was reported by Ye *et al*.[137] They anchored two Gd(do3a-am) chelates onto an acyclic construct with an incorporated 2-cyano-6-hydroxyquinoline moiety and sensitive biothiol (Fig. 1.8b). Exposure to reductive media cleaves disulfide bonds, which promotes intramolecular macrocyclization of the acyclic precursor followed by self-aggregation of hydrophobic cyclo-adducts into Gd-NPs, resulting in amplified r_1 by 60%.

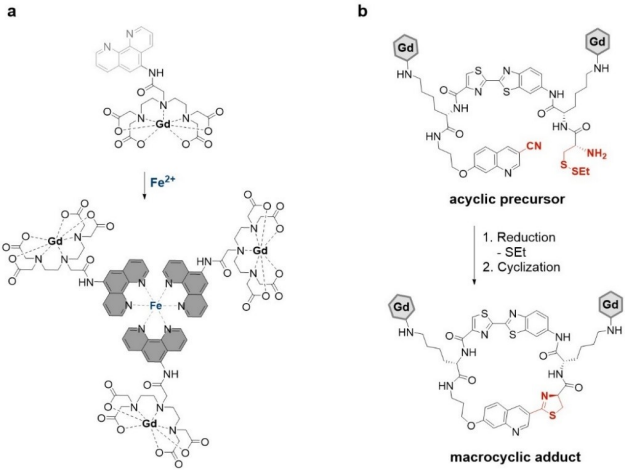

Figure 1.8. Activable CAs modulated by tumbling rates. (**a**) Change in tumbling is induced by coordination-driven self-assembly of three **[Gd(dtpa-phen)]**$^-$ units around Fe^{2+} ion into tetrametallic **[Gd(dtpa-phen)$_3$Fe]**. (**b**) Redox-triggered change in rotational dynamics exploiting argentation of poorly soluble macrocyclic adducts.

The Lepage group designed a proteinase-modulated contrast agent (**PCA-2-switch**), aiming at visualization of *in vivo* activity of the cancer marker, the matrix metalloproteinase-2 (MMP-2) enzyme (Fig. 1.9a).[138] The **PCA-2 switch** consisted of Gd-DOTAam conjugated *via* a hydrophobic C-12 alkyl chain to the N-terminus of the cleavable peptide substrate and a hydrophilic PEG_8 chain attached to the opposite

C-terminus. Upon cleavage of the peptide by MMP-2, detachment of PEG fragments caused accumulation of PCA-2 due to decreased water solubility. This is followed by a change in r_1 from 2.06 (± 0.04) $mM^{-1}s^{-1}$ for the **PCA-2 switch** to 2.18 (± 0.03) $mM^{-1}s^{-1}$ for the PCA-2. The observed increase is the result of longer τ_R, which occurred due to agglomeration. The opposite strategy, with respect to change in tumbling rate, was implemented by Catanzaro *et al.*[139] Here, the MMP-2 cleaves the hanging part of the Gd-chelate, which is partly embedded into the liposome membrane, leading to greater mobility of the released Gd-cage (Fig. 1.9b). The increase in rotational mobility of the cleaved part is analyzed by means of the R_{2p}/R_{1p} strategy, whose response is independent of the concentration of contrast agent.[140]

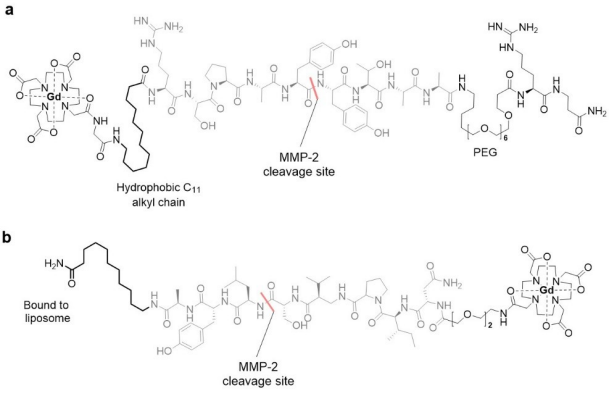

Figure 1.9. Enzyme-activated solubility-switchable CAs. In gray color are depicted the cleavable peptides, where "↓" marks the cleavage site. MMP-2-cleavable Gd-probes are activated by cleavage of (**a**) SGESPAY↓YTA and (**b**) NIPVS↓LYA peptide sequences.

Another way to reduce molecular tumbling is by changing the conformation of large molecules. A notable design was reported by Aime and co-workers, who utilized a ratiometric r_1/r_2 MRI strategy to exploit pH-dependent rotational dynamics of macromolecular probe **[(Gd(dota-am)$_{33}$ – Orn$_{205}$]**.[141] The probe is based on poly-L-ornithine, having 33 out of 205 terminal amines conjugated *via* a squarate moiety to a Gd(dota-am)-based MR reporting unit (Fig. 1.10). At pH < 9, the non-conjugated terminal amines are positively charged, giving rise to the random coil conformation, while higher pH promotes the α-helical structure.[142] At pH values of 7, 10, and 12, these two conformations exhibited global rotational correlational times of 1.0, 1.7, and 3.6 ns and local reorientational times of the chelate 0.23, 0.27, and 0.52 ns, respectively. These differences in rotational dynamics of conformers lead to a boost in the R_2/R_1 ratio over the pH range from 7 to 12.

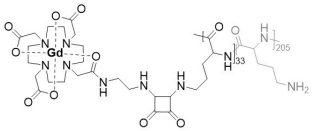

Figure 1.10. The chemical structure of **[(Gd(dota-am)$_{33}$ – Orn$_{205}$]**.

1.4.2 *q*-modulation

q-activation implies modulation of water access to chelated paramagnetic ions, triggered by stimuli, between the "on" state, which produces a strong MRI signal, and the "off" state, characterized by a low signal.[143] In this respect, the design of responsive probes requires changes in the coordination sphere, resulting in either displacement or coordination of water molecule(s). The first responsive CA designed to assess enzymatic activity was reported in 1997 by Meade *et al.*[132] The probe consisted of a Gd(do3a)-derived transducer where the access of water to the paramagnetic Gd^{3+} is restricted by a covalently bound galactopyranose ring *via* a cleavable linkage to the remaining pending arm. Exposure to the β-galactosidase cleaved the galactopyranose moiety irreversibly, producing a monohydrated cage with r_1 elevated by 20%. Opposite to the activation by irreversible changes is activation induced by reversible changes, involving dynamic systems. In the study carried out by Tircsó *et al.*[144] the Mn(II)-probe derived from the H_3(pc2a) ligand having an ethylamine arm sensitive to pH was used. The pH-dependent coordination of the ethylamine arm enabled a turn-on response at physiological pH (K_{MnL}^{H} = 6.88). The reduction of ligand denticity promoted coordination of the water ligand, the so-called turn-on mechanism, resulting in higher inner-sphere relaxivity.

Traditional design of RCAs for sensing metal ions M^{n+} includes the presence of a second chelator, which selectively binds a target cation and induces flipping of a shared pendant, which can exchange between Ln^{3+} and M^{n+} coordination spheres. In the presence of M^{n+}, the shared pendant arm flips from the MR reporter cage onto the M^{n+} chelate, increasing IS hydration, which leads to an off/on response. The very first calcium-sensitive MRI sensor for the functional imaging of the CNS was pioneered by Meade *et al.* (Fig. 1.11a).[145] This MR reporter consisted of two Gd(do3a)-derived chelates bridged by a modified BAPTA chelator with improved selectivity to Ca^{2+} over Mg^{2+} and affinity in the low μM range, coined for intracellular sensing of Ca^{2+} transients.[146] The Ca^{2+} sensor is 'smuggled' into the cell as an ester and activated by ester hydrolysis.[147] A similar example involving an Mn^{2+}-based MRI transducer and BAPTA as a Ca-responsive moiety was published by the Jasanoff lab.[8] Throughout the years an amazingly large number of low-affinity variations, employing EDTA, EGTA, and DTPA as Ca-switches, were proposed for sensing extracellular Ca^{2+} (0.1 to 2 mM).[148, 149] The same logic was used by Chang *et al.* to produce a series of GBCAs sensitive to Cu^{+} ions in the presence of Na^{+}, K^{+}, Ca^{2+}, Mg^{2+}, Fe^{2+}, Fe^{3+}, Cu^{2+}, and even ten-fold concentrations of competitive Zn^{2+} ion.[150] The opposite sensing strategy has been explored on a Gd-DTPA-derivative, in which two carboxylates were functionalized with Zn^{2+}-chelating units (Fig. 1.11b).[151] In the

absence of the Zn^{2+} ion, the aminocarboxylates assist the binding of Gd^{3+}, whereas in the presence of Zn^{2+}, they rearrange by forming the Zn-chelate, which blocks access of water molecules to Gd^{3+}.

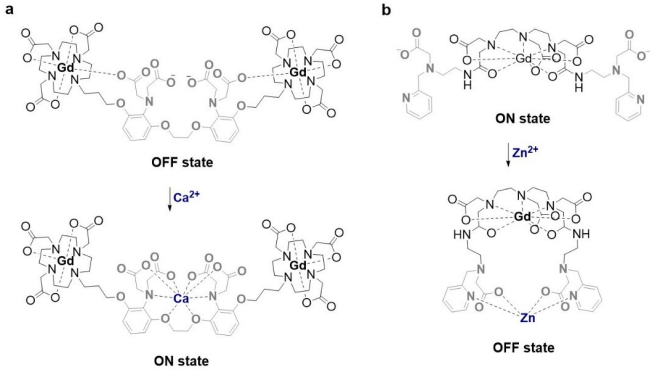

Figure 1.11. *q*-modulated activation of responsive CAs induced by M^{2+} ions**.** (**a**) The turn-on mechanism is featured by a reduction in ligand denticity. The Ca-free form is off-state, where the water coordination is impaired due to steric hindrances coming from Gd-bapta interactions, resulting in a weak MRI signal. Binding of calcium disturbs Gd-acetate(bapta) interactions, promoting inner-sphere hydration and thus a stronger signal. (**b**) The turn-off mechanism is triggered by coordination of Zn^{2+}, inducing steric hindrances that block water from binding Gd^{3+}.

Unlike previous turn-on designs triggered by Ca^{2+} ions and enzymatic cleavage, where selectivity is defined by the BAPTA affinity to calcium and enzyme specificity, respectively, the main contributing interactions in the turn-off mechanism, in the case of polycharged guests, are Gd-analyte bonds, whereas the selectivity between different guests is governed by additional stabilizing interactions.[152, 153] On account of this goes a notable example of intermolecular ligation demonstrated by Lee *et al.*[154], who developed genetically engineered metalloprotein sensor **BM3h-9D7** from the paramagnetic heme protein of bacterial cytochrome mutant P450-BM3[155], sensitive to dopamine with a K_d of 1.3 μM. In the DA-free state, the **BM3h-9D7** exhibited a r_1 of 0.83 mM^{-1} s^{-1}, whereas in the presence of DA, it decreased to 0.10 mM^{-1} s^{-1}. Measured optical spectra of protein revealed that dopamine binds in the BM3h binding pocket as an axial ligand by directly coordinating the heme Fe^{3+} cofactor, reducing the *q*-value from 1 to 0. Selectivity over structurally similar guests is achieved due to greater complementarity of the binding pocket for binding DA.[156] Very recently, Clark and co-workers reported that the ACh-responsive nanosensor **ACh-MRNS** consisted of a nanoparticle composed of a polyvinyl chloride core coated by amphiphilic DSP-PEG-lipid, onto whose surface were co-immobilized a pH-responsive Gd-based MR transducer and the enzyme butyrylcholinesterase (BuChE) (Fig. 1.12).[157] The enzymatic cleavage of ACh into choline (Chol) and acetic acid, whereas the pH drop in the microenvironment of the Gd(do2a)-based reporter protonates the coordinated phenoxide, causing its further

detachment and consequent increase of $1/T_1$ relaxation rate by 20% due to higher inner-sphere hydration.

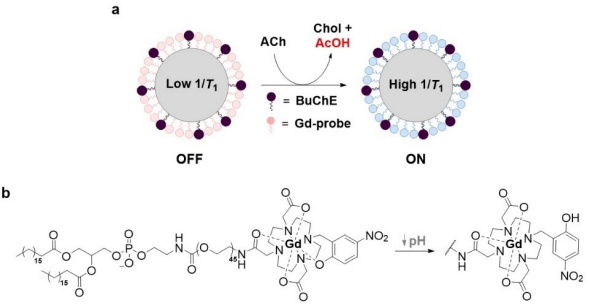

Figure 1.12. Chemical structure and mechanism of an Ach-responsive nanosensor. (**a**) activation mechanism of the **ACh-MRNS** and (**b**) *q*-modulated response mechanism of covalently attached pH-sensitive Gd(do2a)-based chelate. The role of the nanoplatform is to keep the two components, BuChE and the MRI transducer, in close proximity.

1.4.3 Miscellaneous Activation Mechanisms

In this section are discussed responsive CAs, which could not be classified in either of the previously described groups, including fluorinated, paraCEST, and hyperpolarizable CAs.

High interest in the development of ^{19}F MRI probes is due to the lack of background signal in humans and the high sensitivity of ^{19}F nuclei, comparable to that of protons ($\gamma(^1H)/\gamma(^{19}F) \sim 1.06$).[158] Most of the current examples can be summarized into two categories, which make use of conceptually different effects.[159] The first strategy implies modulation of fluorine signal sensitivity *via* PRE, which is practically achieved by alternating the distance between the paramagnetic metal ion and ^{19}F. Yu *et al.*[160] exploited the paramagnetism of Fe^{3+} to develop a non-magnetic ^{19}F-based probe responsive to β-galactosidase. Enzymatic cleavage of the sugar moiety unmasks the chelator, which, in the presence of Fe^{3+}, assembles into a dimeric chelate, shortening the T_2 value of the nearby ^{19}F label. Another notable design was demonstrated by Sakamoto's group,[161] who used a Gd(do3a)-chelate functionalized with ^{19}F end-labeled oligodeoxyribonucleotide (ODN) motif to visualize *in vivo* gene expression (Fig. 1.13). The second strategy is grounded on ^{19}F LIS, which exploits a large spectral range of ^{19}F.[162] Parker and co-workers implemented ^{19}F LIS to develop a pH-responsive Ho(do3a) derivative featured by a fluorinated ethylamine sulphonamide pending arm.[163] At pH < 5, the coordinated sulfonamide group detaches due to protonation, causing ^{19}F LIS by 40 ppm. The same group reported numerous Ln(III)-based responsive probes incorporating Ca^{3+}, citrate, and esterase switches.[164] Further variation of the ^{19}F LIS effect is reported by Blackburn *et al.,* who demonstrated ^{19}F CEST of free fluoride ions using a strongly

paramagnetic Yb(dotma) platform, which induced Δδ between free and bound F^- of 736 ppm.[165]

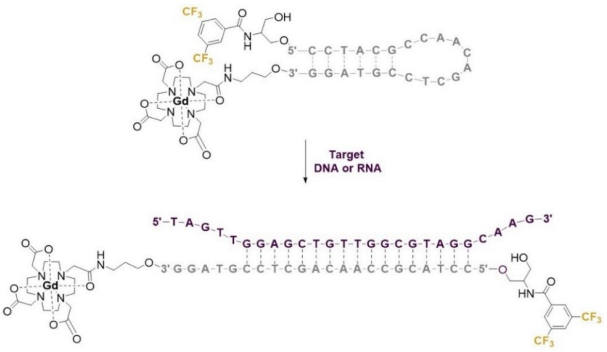

Figure 1.13. PRE activation of fluorinated probe. The fluorinated self-immolative ODN motif is folded, placing ^{19}F in the vicinity of Gd^{3+}, which has a much more pronounced effect on T_2 shortening over T_1. The resulting low T_2/T_1 ratio leads to a broadening and disappearance of the ^{19}F signal in both MRI and MRS. The addition of a probe with complementary ODN increased the Gd–^{19}F distance, resulting in a greater T_2/T_1 ratio and, consequently, a more intense ^{19}F signal (turn-on mechanism).

To date, numerous responsive paraCEST probes have been developed where the CEST is modulated by the oxidation state of the paramagnetic center. Morrow *et al.* introduced the CoCEST-responsive probe, which switches between the CEST-active paramagnetic Co^{2+} and silent Co^{3+} forms.[166] The complex is made of a TPT ligand, whose paramagnetic form is characterized by the appearance of ^1H signals at 140 ppm coming from exchangeable amine groups on pyrazole pending arms. Exposure to O_2 conditions converts Co^{2+} into diamagnetic form, leading to loss of proton resonances. Another type of redox-activatable paraCEST CA has been reported by Sherry and co-workers, who constructed a Eu^{3+} complex derived from the H_4(dota)(gly)$_4$ framework in which two pendants were functionalized with *N*-methylquinolinium moieties that mimic the oxido/reductive role of the redox couple [NADH]/[NAD^+].[167] Reduction of the quinolinium moiety by β-NADH into dihydroquinoline induced changes in the coordination environment of Eu^{3+}, resulting in a CEST increase from 2 to 15% for the metal-bound water molecule and a signal shift change from 43 to 50 ppm. Traditional lipoCEST agents display two water resonances, corresponding to intra- and extra-liposomal bulk water, where the selective saturation of intraliposomal water and exchange through the liposomal bilayer transfers saturation into the extra-liposomal compartment.[168] A clever strategy to exploit the CEST effect combined with Gd-doped liposomes into a dual ^1H T_1-CEST agent was introduced by Terreno *et al.*[169] The dual probe consists of an encapsulated paramagnetic CEST agent, **Tm(dotma)**, and a Gd(do3a) chelate immobilized on the surface through a cleavable disulfide linkage (Fig. 1.14). When the Gd-probe is attached at the surface, it relaxes the bulk water protons, which

impairs the CEST effect. In the presence of a reductive stimulus, a **Gd(do3a)**-derived chelate is detached as the SS bond gets cleaved, which activates lipoCEST.

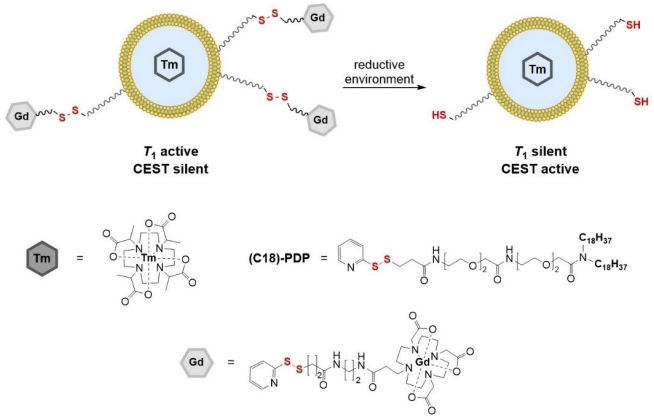

Figure 1.14. Dual-modal LipoCEST contrast agent. The activation mechanism is triggered by cleavage of the disulfide bond. Chemical structures of: (i) Tm(dotma) is the ^{1}H CEST active component; (ii) the reactive C18-PDP moiety was used to bridge the liposome, *via* aliphatic alkyl chains, with Gd-chelate, through disulfide linkage; (iii) the T_1-active component is the Gd(do3a)-derived chelate.

The spin hyperpolarization technique is readily combined with molecular sensors to enhance the sensitivity of conventional MRI by several orders of magnitude. In 2006, Pines and co-workers pioneered the concept of HyperCEST, intended for gas-phase NMR-based imaging.[170] This approach combines different types of xenon sensors with affinity tag[171-175] and the hyperpolarizable ^{129}Xe isotope with CEST imaging,[176] allowing detection in the nM concentration range[177] and short acquisition times. The inner cavity of encapsulating hosts is crafted to accommodate ^{129}Xe, providing exchange rates with media suitable for CEST.[178] An additional benefit of ^{129}Xe is that it produces very high SNR since it is not a biogenic element. Further advances in terms of targeted imaging have been put forward by Francis *et al.*[179] who developed a CB6 rotaxane host for ^{129}Xe hyperCEST responsive to MMP-2. The different approach involving hyperpolarization of ^{13}C nuclei by the DNP technique was recently reported by Westmeyer and co-workers.[180] They demonstrated usage of **^{13}C-EGTA** and **^{13}C-EDTA** as hyperpolarizable MRI probes responsive to divalent metals M^{2+}; biologically important (Ca^{2+}, Zn^{2+}, Mg^{2+}) and the common toxic ions (Cd^{2+}, As^{2+}, Pb^{2+}). In response to complexation with M^{2+}, the hyperpolarized chelators undergo conformational changes displaying carboxylic ^{13}C resonances specific for each M^{2+}- bound adduct (Fig. 1.15a).[181] These probes allowed faster detection in the μM range after dynamic nuclear polarization. The drawback of hyperpolarization is primarily limited by the rapid T_1 magnetization decay. This issue has been addressed by the Nonaka lab.[182] aiming at detection of Ca^{2+} by ^{15}N hyperpolarized CAs, with extended time over several tens of minutes, due to long ^{15}N T_1 of 815 s at 1.51 T (Fig.

1.15b). A different approach relying on the application of complex compounds has been reported by Kovaćs *et al.,*[183] who used ^{89}Y(III) nuclei as an alternative with long T_1 relaxation to develop an **^{89}Y(do3a-NTs)** pH-responsive hyperpolarizable CA (Fig. 1.15c).

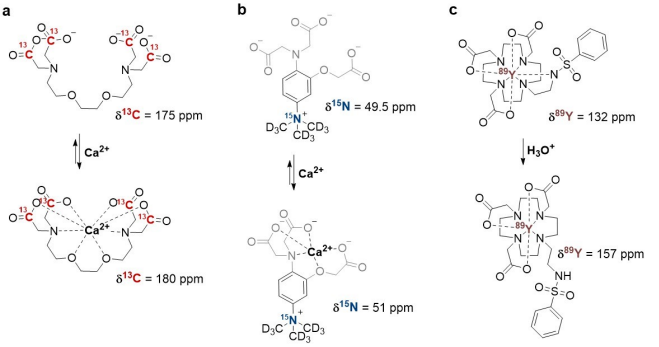

Figure 1.15. Responsive hyperpolarizable sensors for NMR-based detection**.** Interaction with stimuli induces conformational changes that modify chemical and magnetic properties of hyperpolarizable labels, resulting in shift changes. (**a**) In the case of Ca^{2+}, the binding to **^{13}C-EGTA** induced a Δδ of ^{13}C carbonyls for 5 ppm. (**b**) Binding of Ca^{2+} evokes deshielding of hyperpolarized ^{15}N-label, causing Δδ of 1.5 ppm. (**c**) Response of ^{89}Y-based sensor to pH.[183] At pH 4 the coordinated sulfonamide is shielding the hyperpolarized ^{89}Y-label; upon change of pH to 9, nitrogen detaches due to protonation, resulting in an ^{89}Y Δδ of 25 ppm downfield.

1.5 Dendrimeric scaffolds in mMRI

Dendrimers are well-defined, multivalent, radially layered polymers with tunable physicochemical properties, which makes them suitable for biomedical applications.[184] The name "dendrimer" was introduced by Tomalia et *al*.[185], tailored from the Greek words "*dendro*" and "*meros,*" giving prominence to the branched-like shape of molecules. Although less frequently, in the literature can be found other terms referring to dendrimers, such as "cascade polymer" and "arborols." In the following subchapter, dendrimeric structural features of importance for drug delivery and their impact on properties of conjugated small-molecule responsive MRI contrast agents are discussed.

1.5.1 Pharmacokinetic properties of dendrimers

Regarding the molecular design, dendrimers consist of the following components: (1) a central core, which could be a small functional molecule[186, 187], metal-based[188], polymer[189] or a nanoparticle[190]; (2) repeating building blocks covalently attached in a cascade pattern from the core towards the exterior; and (3) end-groups, which are of vital importance for pharmacokinetic properties.[191] The example of dendrimeric

architecture is illustrated in Fig. 1.16, for the case of the poly(propylene imine) (PPI) dendrimer, **Am-DAB-32**.

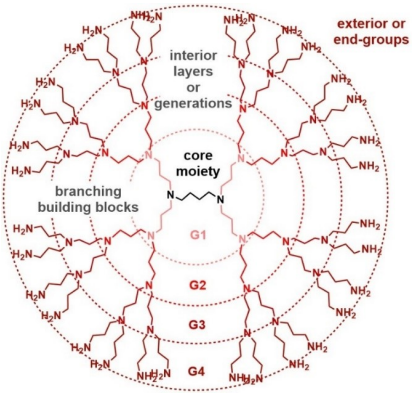

Figure 1.16. Structural properties of dendrimers illustrated by **Am-DAB-32**. The PPI dendrimer consists of the following structural fragments: (1) DAB core, abbreviated from diaminobutane; (2) propylene imine branching units, radially spreading from the core towards the surface; and (3) amine terminal or end groups (Am), in this case corresponding to 32, which is equivalent to the fourth generation (G4) of interior layers. Dendrimers are also featured with internal cavities of different dimensions, which could accommodate various small guest molecules.

Properties such as polydispersity, a large number of surface groups and ease of their functionalization, a polycharged interior, and tunable toxicity give rise to a practical application of dendrimers as versatile molecular scaffolds for insoluble pharmaceutical agents. The importance of surface morphology and hydrodynamic radii are decisive factors for biodistribution and blood circulation. In general, particle sizes of hydrodynamic radii less than 4 nm are rapidly filtered off by kidneys.[192] The amine-terminated G4 PAMAM dendrimers with positively charged surfaces establish electrostatic interactions with anionic proteoglycans, leading to a rapid accumulation in the liver, spleen, and lungs, which makes them more toxic.[193] To increase biocompatibility, the surface charge is usually being neutralized by coating with peptides, polysaccharides, or PEGylation.[194] In addition, PEGylation prolongs circulation time, leading to less accumulation in the liver and kidneys and elevated preferences towards tissues with leaky vasculature, such as inflamed[195] or cancerogenic tissues[196], through so-called passive targeting. Moreover, active targeting of a specific tissue can be achieved *via* additional functionalization with a targeting moiety.[197]

1.5.2 Dendrimers as Nano-Carriers Dendrimers as Nano-Carriers

In recent years, dendrimers have attracted a lot of attention as versatile nanocarriers for poorly soluble and toxic therapeutics that are prone to hydrolysis under

physiological conditions.[198] Dendrimer-drug conjugation provides enhanced solubility, improved stability, and therapeutic effects. The active pharmaceutical compounds can be loaded into dendrimers by inclusion, physical adsorption, or covalent attachment (Fig. 1.17).[199-201] The internal voids bind small guests by establishing hydrophobic interactions[200], hydrogen bonds[202] or electrostatic interactions with the charged interior.[203, 204] In addition, dendrimers can function as unimolecular micelles[205], where the polar surface provides good solubility in hydrophilic media while the hydrophobic interior entraps and solubilizes nonpolar guests.[206]. Depending on the type of dendrimer, dendrimer-drug complexation through electrostatic interactions can take place with a charged surface as well.[207] Covalent conjugation implies attachment of target molecules onto the surface.[208] These dendrimer-drug conjugates could be designed to release tail groups in response to stimuli. For instance, Zhu *et al*. demonstrated acid-triggered release of the anti-cancer drug doxorubicin, previously functionalized to PEGylated PAMAM dendrimeric end groups *via* an acid-sensitive *cis*-aconityl amide linkage.[209] On the other hand, periphery has been modified by various groups to improve targeting[210] and cell internalization[208].

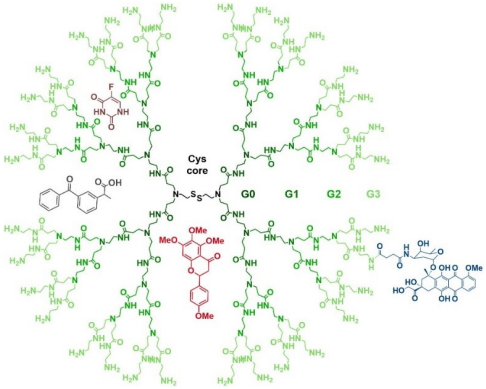

Figure 1.17. Types of interactions of G3 PAMAM-dendrimer with various guest molecules. (1) Entrapment of 5-fluorouracil (brown) is supported by interactions mediated through close-contact events and short-lived H-bonds[206], and ketoprofen (grey) is dominated by dispersion terms and weak H-bond interactions[211, 212]; (2) covalent conjugation of dox (blue) to the peripheral amines.[208]

Furthermore, multivalency of dendrimeric external groups has been exploited to prepare various dendrimer-conjugated MRI CAs. Rajca *et al.* introduced the G4 PPI-conjugate as the metal-free organic radical contrast agents (**ORCAs**) in which the paramagnetic nitroxide free radicals are conjugated to the surface of the G4 PPI dendrimer (Fig. 1.18a).[213] Loading capacity of free radical and mPEG units was estimated to be 12.6 and 35.8, respectively, providing an r_1 of 5.0 mM^{-1} s^{-1}. Conjugation of a large number of paramagnetic units increases a local concentration of MRI reporters and thus signal intensity, with, however, a lack of specificity. This issue could be resolved by functionalization with a targeting moiety. For instance,

Baker and co-workers specifically targeted tumor cells expressing folate receptors by introducing folic acid as a tag next to a Gd(dota)-derived MRI transducer (Fig. 1.18b).[214] Next to surface functionalization, dendrimers with cleavable cores are readily used to produce dendrons, offering additional branching points for further functionalization. One of the works previously conducted within our lab demonstrated usage of a surface-functionalized G4 PAMAM dendrimer with a non-sensitive Gd-chelate to obtain a dendron-like multimodal CA (Fig. 1.18c).[215] Namely, the reductive cleavage of the disulfide core provided a G4 PAMAM dendron derivative, which was further functionalized with a lysine spacer bearing a biotin tag and FITC dye.

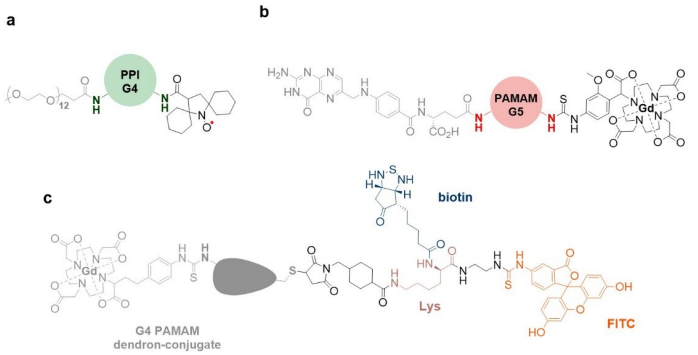

Figure 1.18. Multivalent conjugation of dendrimeric terminals. (**a**) A G4 PPI-conjugate bearing PEG units (grey) and a free radical (right) as the paramagnetic MR reporter. (**b**) G4 PAMAM-conjugate having attached folic acid as the transfection component (gray) and a Gd(dota)-derived MR reporter (black). (**c**) Multi-modal G4 PAMAM dendron-like CA for targeted MRI and optical imaging.

Günduz *et al.* extended the scope of dendrimeric CAs to Ca^{2+}-responsive PAMAM-conjugates.[216] The design consisted of a Gd(do3a)-derived MR transducer bridged to PAMAM amine terminals by a modified EGTA chelator as a Ca^{2+}-switch, whose affinity is suited for sensing transient concentrations in extracellular space. Upon saturation with 2.0 equiv. of Ca^{2+}, the induced rigidification of the EGTA moiety caused an increase in the hydrodynamic diameter of the PAMAM-conjugate from 5.4 to 8.3 nm for the Ca-bound form. These changes were followed by the co-existence of non-synchronized changes of r_1 and r_2 relaxivities, resulting in the r_2/r_1 increase of over 100%. In similar fashion, Sherry and co-workers, coupled a pH-responsive Gd-chelate onto a PAMAM dendrimer, where the synergy of altered tumbling and proton exchange rates enhanced responsiveness to pH by more than a factor of 2.[217] To improve the solubility of dendrimeric-CA conjugates, the hydrophilic PEG is often co-attached onto the dendrimeric surface. However, oxygen from the PEG unit may interfere with relaxation properties by establishing weak Gd–O_{PEG} interactions.[218] Another interesting example of dendrimer application comes from Bulte *et. al.*[219] who employed a carboxylate-terminated G4.5 PAMAM dendrimer to stabilize magnetic SPIOs, as illustrated in Fig. 1.19, and deliver the resulting **γ-Fe_2O_3** NPs,

which are stable over a wide range of pH values and temperatures, into the cell. The magneto-dendrimers displayed remarkably high r_2 relaxivity, reaching 200–400 mM^{-1} s^{-1}.

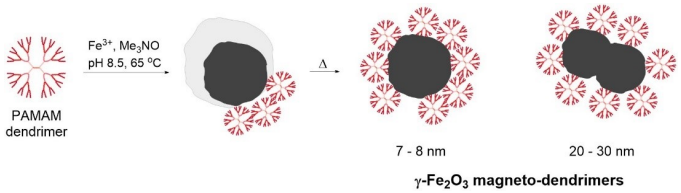

Figure 1.19. Schematic depiction of **γ-Fe_2O_3** stabilization into nanoparticulate magneto-dendrimers. The procedure consists of coating superparamagnetic **γ-Fe_2O_3** NPs with carboxyl-terminated G4.5 PAMAM dendrimers into magnetodendrimers with a core size of 7–8 nm, which aggregates into 20–30 nm core-sized superparamagnetic nanocomposites.

In summary, the positive aspects of paramagnetic sensors conjugated to dendrimer terminals are: (1) improved biocompatibility arising from the dendrimeric component, (2) increased local concentration of Cas, (3) altered T_1 and T_2 relaxivities, and (4) the ability to load various types of pharmaceutically active components, which opens the possibility to easily prepare multimodal nanoconjugates. On the contrary, the main disadvantage is a potential interaction of non-functionalized terminals with the paramagnetic chelates, which could diminish catalytic activity towards the bulk water protons.

1.6 Neurotransmitters

Neurotransmitters are molecular messengers that carry information across the brain, from the presynaptic to the postsynaptic neuron to the final effector cells, glands, or muscle. This communication occurs through ports termed synapses, where the messenger molecules exit the intracellular compartment and bind to the membrane receptor of another cell, triggering its biochemical response.[220] The circuit of NTs starts in the presynaptic neuron, where they are synthesized and stored in synaptic vesicles.[221] During neuronal activation, an action potential depolarizes the presynaptic membrane, resulting in an influx of Ca^{2+}, causing vesicles to fuse with the plasma membrane, followed by a burst of NTs into a 20 nm narrow gap called the synaptic cleft.[222, 223] Released NTs diffuse towards the postsynaptic neuron, where they bind receptors on the membrane, either exciting or inhibiting their function. This causes the appearance of action potential, after which transmitters detach. The freed NTs are removed by NT transporters and recycled or diffuse away from the synaptic cleft and get degraded by enzymes.

In a broad sense, NTs are classified into small-molecule NTs and neuropeptides. However, the focus of this study is set on low-molecular-weight amino acid transmitters (Gly, Glu, Asp, and GABA) depicted in Fig. 1.20, with the emphasis on the main excitatory and inhibitory ones, Glu and GABA, respectively. The amino acid NTs regulate various processes such as breathing, digestion, mood,

memory, and sleep, and besides their regulatory role, some NTs are important intermediates in biosynthesis.[224-226] Consequently, any abnormality in their functioning manifests in the appearance of various psychiatric and neurological disorders such as Huntington's chorea, Alzheimer's disease, and epilepsy, which make NTs irreplaceable biomarkers for reading out physiological and pathological brain conditions.[227]

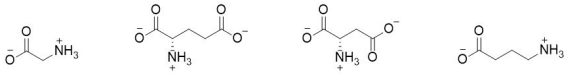

Figure 1.20. Chemical structures of amino acid NTs at physiological pH.

Concentration of neurotransmitters in the synaptic cleft is not constant, but it changes dynamically during synaptic activity. For instance, in the basal state, the concentration of Glu is in the low μM range,[228] whereas during synaptic activation, it increases drastically by more than 100-fold, peaking at 1.1 mM, and stays elevated on the millisecond time scale (0.7–2 ms).[229-232] In addition, Jahr and Dzubay claim an extrasynaptic Glu concentration of 190 μM.[230] The AAs transients are well into ranges detectable by mMRI.

1.6.1 NTs as endogenous contrast agents

The MRI modality for direct imaging of transmitters is diamagnetic CEST, where the NTs play the role of frequency labeled endogenous CAs. The NTs-based CEST exploits the exchangeable amine protons to enable visualization in an indirect manner by monitoring the decrease in the water signal.[233] In the case of Glu, the exchange rate of amine protons at pH 7, which corresponds to the physiological intracellular pH of neurons[234], is intermediate to slow ($2000 \pm 500\ s^{-1}$) on the NMR timescale[235], resonating at 1.2 ppm downfield to the bulk water resonance (37°C, 7 T). Having that at 7 T, the $\Delta\omega = 5700\ rad\ s^{-1}$, GluCEST imaging can be performed successfully at $B_0 \geq 7T$.[233, 236] The exchange rate is also pH-dependent, and in the case of Glu, the CEST is maximal at pH 6. Reddy *et al.* demonstrated GluCEST *in vivo*, where it was established that 70-75% of CEST comes from Glu, with the remaining 25-30% coming from exchangeable protons with similar resonant frequency, creatine, GABA, and other biomacromolecules.[233] The same group used the GluCEST technique to measure concentrations of Glu in humans and as a pH marker for brain tumors and ischemia,[237] reporting signal contaminations to be between 25 and 30%. So far, GluCEST MRI has been successfully applied to study various neurodegenerative diseases involving tauopathy[238], epilepsy[239], traumatic brain injury[240], Alzheimer's disease[241], schizophrenia[242], Huntington's disease[243], and to visualize distribution of Glu in the brain. In addition, Wu and co-workers have recently demonstrated the application of CEST MRI for GABA imaging *in vivo* on rat models with brain tumors.[244]

In clinical imaging, GluCEST is often supplemented by the complementary technique the MRS.[245, 246] The MRS acquisition approach provides information on chemical composition in ROI. The detection principle relies on capturing chemical shifts of spin-active nuclei present in endogenous metabolites, such as ^{1}H, ^{13}C, ^{19}F, and ^{31}P.[247-249] Imaging NTs by ^{1}H MRS is impaired due to non-selectivity, as the resonances of a large number of metabolites resonate in a span of 4-5 ppm, resulting in overlapped signals. On the other hand, ^{13}C MRS offers a chemical shift range of around 200 ppm, which comes at the expense of decreased sensitivity, as the γ (^{13}C) comes about ¼ of γ (^{1}H). Besides, the intrinsically low sensitivity is additionally weakened due to the low natural abundance of the ^{13}C isotope (1.1%) and signal splitting owing to coupling. However, the ability to enrich brain metabolites with a ^{13}C label has made this technique suitable for *in vivo* imaging of humans. Labeling of NTs is achieved by administration of a ^{13}C-labeled precursor (glucose or acetate), which, upon the TCA cycle, yields ^{13}C-labeled NTs. Since that mechanism of the TCA cycle is well investigated, choosing the position of a label in the substrate allows precise labeling of the final NTs (Glu and Gln). For instance, administration of 1,6-$^{13}C_2$-Glc upon the first turn of the TCA cycle provides 4-^{13}C-Glu.[250] As the glucose is dominantly taken up by neurons and acetate by astrocytes, the choice of substrate enabled functionality assessment of neuronal and glial dysfunction, respectively. For instance, measurements of C2-Glu and C2-Gln metabolic loads, indicative of neurons and glial cells, respectively, revealed a reduced Glu/Gln ratio in patients with Alzheimer's disease.[251] This finding is indicative of a faster TCA cycle in glial cells. Despite the fact that these studies allowed dynamic monitoring of Glu metabolism in the human brain, due to low SNR or ^{13}C nuclei, the potential of ^{13}C MRS is not fully exploited. One way to additionally enhance the ^{13}C signal is through the DNP process. However, an attempt to hyperpolarize glucose was unsuccessful, as the time for conversion overexceeds the lifetime of hyperpolarized ^{13}C nuclei due to the short T_1 of glucose. On the other hand, approaches that imply the usage of hyperpolarized Glu are impractical due to the inability to pass through the BBB.

1.6.2 Synthetic receptors for Amino Acid neurotransmitters

Early designs of molecular hosts for AA neurotransmitters recognize the importance of polytopic binding.[252] This comes from the fact that at physiological pH (7.4), AAs exist in a form of zwitterion in which solvation and interaction with various metabolites compete with molecular sensors. An interesting host model is a two-component system comprised of lipophilic and electrophilic aldehyde and squaramide, used to transfer highly polar Gly across the vesicle membrane.[253] The necessity of matching the spatial arrangement of binding sites within a polytopic receptor for the chemical resolution of structurally similar guests has been demonstrated on a fluorescence anthracene-based bis(trifluoroacetylcarboxanilide) sensor, which selectively binds α-amino acids over their β- and γ-homologues.[254] In addition, Yashima and Nonokawa designed a stereoregular poly(phenylacetylene) functionalized with crown ether pendant arms for binding amino acids. This host showed high sensitivity to amino acid chirality as it forms a one-handed helix exhibiting an induced circular dichroism upon complexation with L-amino acids.[255] A more recent example introduced by Delgado and co-workers introduced a

heteroditopic crown-cyclen framework receptor that displayed strong interaction with Gly, established *via* hydrogen bonds between a carboxylate and a protonated cyclen and an α-ammonium cation and an 18C6 anchor receptor.[256] A shift towards metal-based binding platforms was made by Anslyn *et al.*, who reported a receptor comprised of a Zn^{2+} ion framed in a 2,2':6,2-terprydine ligand and two guanidinium groups, which exhibited high affinity to Asp of 1.5 x 10^5 M^{-1} (HEPES, pH 7.4).[257] Receptor-Asp interactions involved cooperative chelation of carboxylate and amine[258] to the Zn^{2+} additionally contributed by interaction of side-chain carboxylate and guanidinium motif.

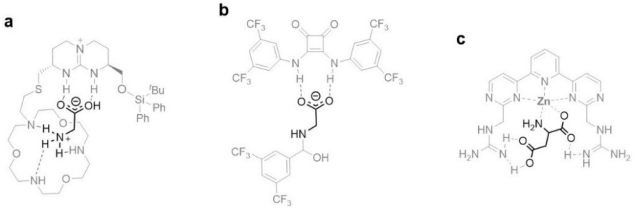

Figure 1.21. Schematic summary of polytopic chemosensors with AA selectivity, depicting multiple interactions between hosts (gray) and the different AAs (black).

Further steps towards translation of metal-based molecular sensors for functional MR imaging of Glu neurotransmitter have been made by Mishra *et al.*[259, 260] Similar to the displacement approach utilized for PET tracers[261], a series of Gd-chelates were appended to various antagonists to tag $mGluR_5$-expressing cells. In cell-bound form, the probe bearing the dipyridyl amide agonist (Fig. 1.22a) displayed a cellular r_1 of 7.4 mM^{-1}. Upon synaptic activation release, Glu displaced the Gd-complex, causing an increase of $R_{1,cell}$ by 28% due to faster tumbling and slower water exchange rates accompanied by detection in the μM range. In the follow-up study, a biotin variant of the lead compound was prepared and used to verify binding specificity and reversibility towards $mGluR_5$ by exploiting conjugation with highly emissive AvidinAlexaFluor448 dye.[262] A similar study targeting the N-methyl-D-aspartate (NMDA) receptor was accomplished by employing a probe containing bicyclic NMDA receptor agonists.[263] A conceptually different approach aiming at direct detection of extracellular amino acid NTs was pioneered in 2014 by Oukhatar and coworkers.[152] A series of T_1 Gd platforms were designed to simultaneously bind carboxylate and ammonium groups of AAs, featured by a turn-off q-modulated response (Fig. 1.22b).[153] These probes are featured by relatively high initial r_1 values, exceeding 9 mM^{-1} s^{-1}, and change in response to Aas by 75%, displaying detection in the mM range. The main drawback is low sensitivity and lack of selectivity of structurally similar metabolites. Yet another undesirable property is intrinsically low thermodynamic stability, as the probes are derived from the H_2do2a ligand. Most recently, the same lab reported on a dual-modal variant of the probe, designed to exploit RIME to HSA for optical and MR imaging.[264]

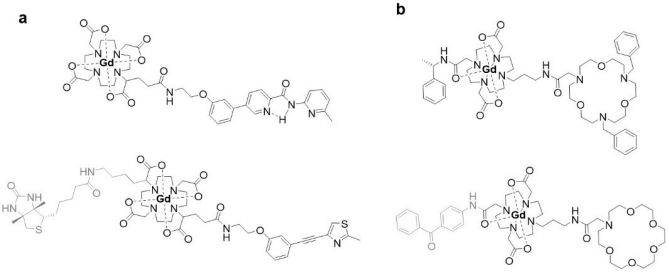

Figure 1.22. MRI sensors responsive to amino acid. (**a**) Gd-probe for visualizing the interaction of a Glu with a postsynaptic cell, having a dipyridyl amide $mGluR_5$ agonist (top image) and additionally attached biotin moiety to act as a dual-mode probe for optical and MRI imaging (bottom). (**b**) Gd(do2a)-based sensors for direct imaging (top) and additionally functionalized with a hydrophobic benzophenone moiety to exploit the RIME effect by binding HSA (bottom).

Chapter 2

In-depth Study of a Novel Class of Ditopic Gd(III)-based MRI Probes Responsive to Amino Acid Neurotransmitters

The efficacy of small-molecule ditopic MRI sensors on binding polycharged AAs relies on the ability of a receptor to form a structural and functional complementary binding pocket. However, due to their relatively complex structure, the amino acid zwitterions are rather challenging molecular targets. In this work, we focus on tuning the binding sites of the Gd^{3+}-based host platform, comprised of a ditopic cyclen-crown ligand framework, to increase the affinity toward AAs. Our approach implied structural modifications of binding sites, designed to simultaneously bind carboxylate and ammonium cations. We prepared and investigated a family of Gd^{3+} complexes with diverse properties, two of which displayed stronger affinity towards glutamate and glycine over metabolic competitors. The thorough investigations involving relaxometric titrations, luminescence, and NMR diffusion experiments, as well as DFT calculations, revealed that the host-guest recognition is controlled by the pending arm on the 18C6 receptor.

Published as:
Front. Chem. **2019**, *7*, 490
https://doi.org/10.3389/fchem.2019.00490
Đorđe Toljić, Carlos Platas-Iglesias, Goran Angelovski*

2.1 Introduction

Some of the most common neural disorders are associated with disturbance in secretion of NTs into the synaptic cleft, which in abnormal amounts triggers a plethora of processes resulting in partial impairment or death of nerve cells.[265] For instance, the excessive release of Glu or GABA causes an imbalance in the excitation level of the brain, leading to various diseases, such as epileptic seizures, which degenerate neuronal tissue.[266] Thus, decoding the spatiotemporal patterns of brain chemodynamics could imply a connection with related diseases. For this reason, the amino acid neurotransmitters are recognized as irreplaceable biomarkers for monitoring neuronal activity. Currently, non-invasive imaging techniques based on MR, *i.e.*, diaCEST and ^{13}C MRS, are preferred due to good spatiotemporal resolution and depth of penetration.[233, 267] However, they do not distinguish between intra- and extracellular concentrations of zwitterionic neurotransmitters and have insufficient chemical resolution and low sensitivity.[268] A promising way to address these issues involves the administration of a paramagnetic sensor capable of altering image contrast upon interaction with a targeted metabolite.[269] Therefore, the development of MR imaging probes responsive to extracellular transmitters is of emerging importance.

To date, direct sensing of NTs has been approached with two distinct designs: *via* genetically engineered metalloproteins and by small-molecule ditopic paramagnetic probes.[155, 270, 271] Although the large-molecule CAs tailored for monoamine neurotransmitters were shown to be capable of detecting target metabolites in the μM range[154], further improvement of small-sized probes is imperative due to issues associated with translation into biological systems. Previously introduced ditopic probes, consisting of a cyclen-based Gd(III)-chelate as the MR reporting unit covalently linked by an amide linker with the 18-crown-6 ether derivative as the ammonium binding site, were shown to be sensitive to Gly, Glu, GABA, and Asp.[270, 271] Unlike the common designs for the Ca^{2+} and enzyme responsive CAs, where sensitivity is governed by the BAPTA chelator affinity to calcium[145] and β-galactosidase specificity[132], respectively, in this approach, recognition of NTs is non-specific, as the selectivity towards AAs is driven by the interactions between the 18C6 motif and ammonium cation.

As a continuation of a study on small-molecule CAs, aiming at selectivity improvement, we set the focus on optimization of a host binding pocket. Specifically, we wanted to reveal which structural factors contribute to the binding of AAs and thus potentially design the probe to be selective to Glu or GABA. Therefore, through a set of chemical modifications, we prepared differing probes with varied sizes and charges of substituents on recognition sites. The host-guest binding affinity was extracted *via* water proton longitudinal relaxation time measurements in response to analytes. Diffusion NMR and fluorescence spectroscopy techniques, as well as DFT calculations, were employed to reveal mechanistic and structural aspects of the recognition process, including changes in the Ln^{3+} coordination environment and the impact of diverse remote groups on solution structures, including the free form of various host molecules and their ternary adducts with structurally different guests.

2.2 Results and Discussion

2.2.1 Molecular Design

We implemented a diversity-oriented synthetic strategy to produce a set of six novel ditopic MRI probes consisting of cyclen-based Gd-chelate and various 18C6-derived ammonium receptors (Fig. 2.1). The **GdL^{1}** chelate combines the common Gd(do3a) cage with the mono N-benzylated 18C6 moiety, whereas complexes **GdL$^{2\text{-}6}$** consist of the H_2do2a-based Gd-chelator and 18C6 binding site with appended substituents of different charge and size **GdL$^{2\text{-}4,6}$** or without substituent **GdL^{5}**. The rationale behind the design of **GdL^{1,2}** is to test the impact of Gd-cage net charge on binding. Here, a non-charged and small benzyl substituent is expected to allow a facile approach of the ammonium cation. Complexes comprising the Gd(do2a) reporter and negatively charged substituents on 18C6, the acetate in **GdL^{3}** and the phosphonate in **GdL^{4}** were designed to assess the role of charge on binding the ammonium end of NTs. These examples are to test the feasibility of replacing hydrogen bonds with stronger electrostatic interactions.

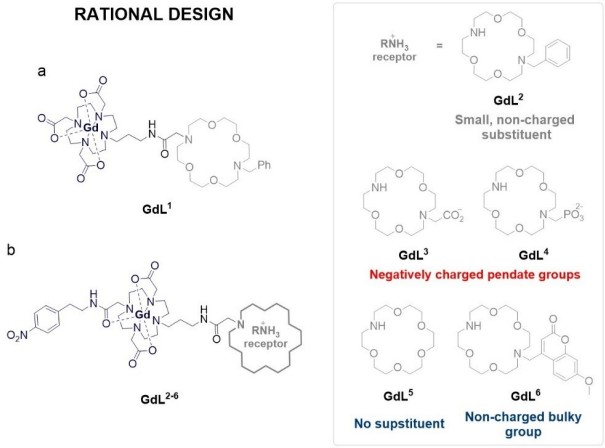

Figure 2.1. Design of ditopic MRI molecular sensors **GdL$^{1\text{–}6}$.** The structures consist of (**a**) Gd(do3a) and (**b**) Gd(do2a)-derived MR transducers (dark blue) and various 18C6-derived receptors for the NH_4^+ group (gray), bridged by the flexible amide linker (black). The receptor exploits the turn-off response mechanism. A GdL-free form displays a strong MRI signal due to water coordination to coordinatively unsaturated Gd^{3+}. When the transmitter binds the receptor, the established Gd-carboxylate interaction displaces bound water molecule(s), decreasing the MRI signal intensity.

In the second approach, the **GdL^{5,6}** were designed to explore the effect of remote substituent size on conformational organization of the binding pocket in the host, which is crucial for guest recognition. The previous studies evidence shows that the carbonyl group of the propyl-amide linker is weakly coordinated to Gd(III), causing cyclen-crown sites to adopt a half-opened shell-like conformation, which is

well suited for binding an amino acid functional group.[270, 271] Accordingly, the **GdL^5** with no substituent was designed to favor strong amide linker coordination as the steric hindrances were minimized. On the contrary, a sterically bulky substituent, Mmc, in **GdL^6**, could theoretically disturb this interaction due to increased steric constraints. In addition, the Mmc is known to bind the amino group of NTs, and thus, the strong fluorescence emission properties of the Mmc group could enable additional interaction studies.

2.2.2 Synthesis of GdL$^{1\text{-}6}$

The preparation of ligands **L$^{1\text{-}6}$**relies on the convergent synthetic strategy, linking cyclen-derived bromides with mono N-substituted 18C6 fragments by direct N-alkylation. The synthesis of bromides **2** and **5** is summarized in Scheme 2.1.

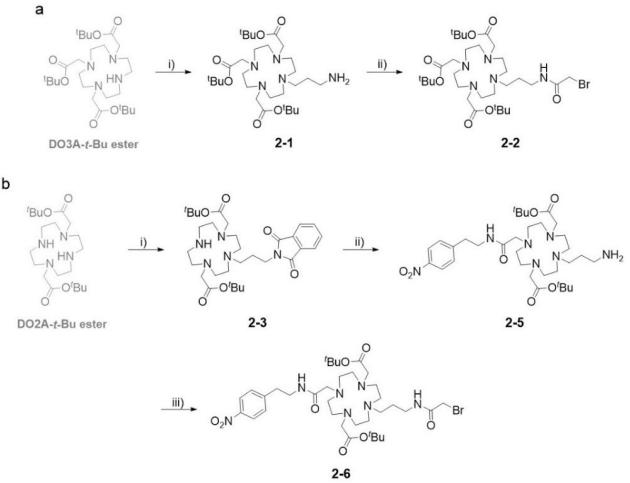

Scheme 2.1. Synthesis of bromide fragments **2-2** and **2-6**. *Reagents and conditions:* (**a**) i) *N*-(bromopropyl)phthalimide, MeCN, K_2CO_3, 45ºC; ii) *i*-PrOH, EDA, 60 ºC, 75% (over two steps); iii) CH_2Cl_2, DCC, bromoacetic acid, 75%. (**b**) i) *N*-(bromopropyl)phthalimide, MeCN, $NaHCO_3$, 3 days, 65%; ii) **2-4**, MeCN, K_2CO_3; iii) *i*-PrOH, EDA, 65% (over two steps); iv) CH_2Cl_2, DCC, bromoacetic acid, 52%.

The bromo fragment **2** was prepared in 4 steps, starting from cyclen. In the first step, cyclen was converted into DO3A *tert*-butyl ester in a one-step procedure,[272] followed by the subsequent N-alkylation with *N*-(3-bromopropyl)phtalimide and mild deprotection of Phth with ethylenediamine to afford the propyl amine derivative **2-1**. The amine **2-1** was coupled with bromoacetic acid in the presence of *N*,*N*'-dicyclohexylcarbodiimide (DCC) to furnish bromide **2-2**.[273] In a similar fashion, the DO2A *tert*-butyl ester was synthesized in 3 steps according to a previously published procedure.[274] The DO2A *tert*-butyl ester was first functionalized with the *N*-(3-bromopropyl)phtalimide to yield **2-3**, followed by

subsequent introduction of the **2-4** in trans position and cleavage of Phth to yield the amine **2-5**, which was subjected to the same treatment as the DO3A analogue to prepare the desired DO2A *t*-butyl ester-derived bromide **2-6**.

The synthesis of the 18C6-derived fragments **2-7, 2-8, 2-10,** and **2-11** commenced from the common precursor 1,10-diaza-18-crown-6-ether (Scheme 2.2). The direct N-alkylation with the corresponding alkyl halides, *tert*-butyl bromacetate, benzyl bromide, and Br-Mmc gave the corresponding products **2-7**, **2-8**, and **2-11**, respectively, in moderate to good yields. The adduct **2-9** was generated under the *Kabachnik-Fields* reaction conditions, followed by the catalytic debenzylation in Parr's hydrogenator to afford the mono *N*-phosphonated derivative **2-10**.

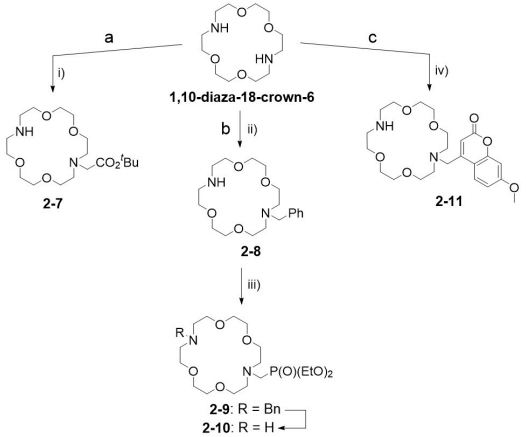

Scheme 2.2. Syntheses of 18C6-derived fragments **2-7**, **2-8**, **2-10,** and **2-11**. *Reagents and conditions*: (a) i) *tert*-butyl bromoacetate (0.95 equiv.), $CHCl_3$, Et_3N, 62%, RT, 2 days. (b) i) BnCl (0.95 equiv), $CHCl_3$, Et_3N, RT, 60 h, 58%; ii) $(C_2H_5O)_2P(H)O$, CH_2O, CH_2Cl_2, $BF_3{\cdot}Et_2O$, Na_2SO_4 anh., 65°C, 60%; iii) H_2, $Pd(OH)_2/C$, EtOH, 3.1 bar, 94%. (c) i) Br-Mmc, MeCN, $NaHCO_3$, RT, 40%.

In general, bridging bromides **2-2** and **2-6** with crown fragments (**2-7**, **2-8**, **2-10**, and **2-11**) (Scheme 2.2), owing to slow kinetics and the tendency of bromides to undergo hydrolysis, required between 3 and 5 days of stirring in dry DMF and N_2 atmosphere to acquire **2-12** to **2-17** in acceptable to good yields of 25 – 75%. Then, the obtained *tert*-butyl esters (**2-12, 2-13, 2-14, 2-16**, and **2-17**) were hydrolyzed with formic acid at 60°C for 16 h into the final ligands $\mathbf{L^{1\text{-}3,5,6}}$ (Scheme 2.3). Deprotection of **2-15** required first transesterification with $BrSiMe_3$, followed by hydrolysis of trimethylsilyl esters to give $\mathbf{L^4}$. The purity of ligands $\mathbf{L^{1\text{-}6}}$ was determined with respect to the nitrogen content obtained by CHN analysis, and the amount of the corresponding $LnCl_3$ salt for the complexation was calculated accordingly in a stoichiometric ratio of 1:1. The complexation of $\mathbf{L^{1\text{-}6}}$ was performed in water, maintaining pH ~ 7.2 at 60°C for 16 h to ensure formation of the thermodynamically

favored cyclen in-cage coordination and yield the final paramagnetic complexes **GdL**$^{1\text{-}6}$.

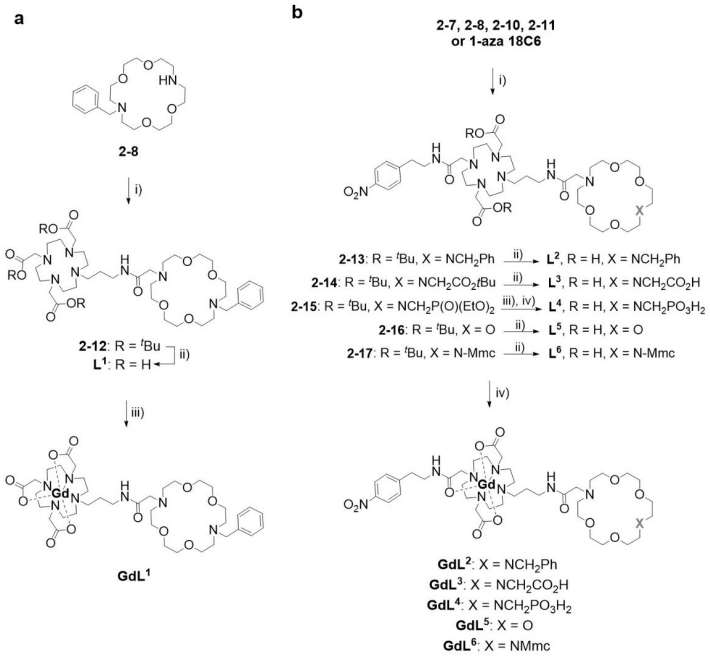

Scheme 2.3. Synthesis of complexes **LnL**$^{1\text{-}6}$. *Reagents and conditions:* (**a**) i) **2-2**, dry DMF, N_2, $NaHCO_3$, 3 days, 70%; ii) HCO_2H, overnight, RT, 76%; iii) $GdCl_3 \cdot 6H_2O$, pH ~ 7.2, 60°C, 16 h. (**b**) i) **2-6**, dry DMF, N_2, $NaHCO_3$, 3 – 5 days, 25 – 78%; ii) HCO_2H, 32 h, 60°C, iii) TMBS (16 equiv.), dry DCM, N_2; iv) H_2O, 50%; v) $GdCl_3 \cdot 6H_2O$, pH ~ 7.2, 60°C, 24 h.

2.2.3 Relaxometric Characterization

The efficacy of the complexes **GdL**$^{1\text{–}6}$ was evaluated in NMR relaxometric titration with the three most abundant AA NTs: Gly, Glu, and GABA; the non-zwitterionic neurotransmitter ACh; and the competitive bicarbonate. The main contributing factor to r_1 relaxivity of bulk water protons is the hydration state of the paramagnetic label.[275] Thus, upon addition of the analyte (A), the hydrated chelate **GdL**(H_2O) associates into the ternary adduct **GdL**(A)**,** in which the coordinated water molecule(s) are displaced to a different extent. This results in a longer T_1 of bulk water protons, that is, reduced longitudinal relaxivity r_1. Furthermore, plotting the r_1 values *versus* the amount of the added analyte and fitting the obtained curves to a modified *Michaelis-Menten's* kinetic model provides the affinity constants for the formed ternary complexes.

The magnitude and curvature of change in r_1 for **GdL$^{1–6}$** upon titration with Gly (0 to 50 equiv.) revealed that recognition is governed by the substituents at both binding sites (Fig. 2.2). Specifically, the observed downward trends are controlled by the size and charge of the 18C6 pendant arm, according to which **GdL$^{1–6}$** were classified in three groups. The first group consists of complexes having the noncharged and sterically small benzyl substituent **GdL^{1,2}** or no substituent **GdL^{5}** at the 18C6. These complexes exhibited a high initial r_1 of over 9.0 mM^{-1} s^{-1}, which decreased to 30, 31, and 36% of the starting value upon saturation with Gly, respectively. In the second group are complexes with negatively charged pendants **GdL^{3,4}**, which displayed relatively high initial relaxivities of 6.88 and 7.14 mM^{-1} s^{-1}, respectively. However, the relaxivity drop until the saturation point is halved when compared with the first group, corresponding to a decrease of 30 and 37%, respectively. In the third group is **GdL^{6}**, functionalized with a sterically bulky and non-charged Mmc moiety, which exhibited the lowest initial r_1 of 6.08 mM^{-1} s^{-1} and a decrease of 63%, which is comparable to that of **GdL^{1,2,6}**.

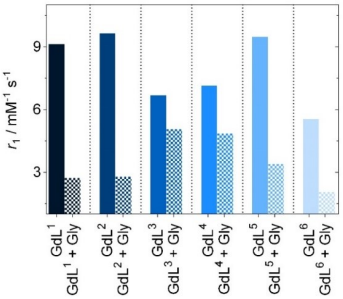

Figure 2.2. Relaxometric characterization of **GdL$^{1–6}$** in response to Gly. r_1 relaxivity values for 3.0 mM **GdL$^{1–5}$** and 1.0 mM **GdL^{6}** in 50 mM HEPES (**a**) before (solid bars) and (**b**) upon saturation with 50 equiv. of Gly (stripped bars) at 25°C (pH 7.4, 300.17 MHz). For the saturation, , the addition point of Gly was taken, after which the further addition produced a change in relaxivity less than 10%.

Table 2.1. Binding affinity (K_a) and relaxivity (r_1) decrease for complexes **GdL$^{1–6}$** upon saturation with 50 equiv. of Gly.[a]

	GdL^1	**GdL^2**	**GdL^3**	**GdL^4**	**GdL^5**	**GdL^6**
K_a [M^{-1}]	47	73	25	17	75	69
-Δ r_1 [%]	70	69	26	31	64	63

[a] K_a values were calculated using modified *Michaelis-Menten's* model (Eq. S2.2).

The affinities towards Gly showed slightly different trends with respect to their amplitudes of r_1 change (Table 2.1). The highest affinities were observed for complexes derived from Gd(do2a) as the MR reporting unit and 18C6 moiety appended with non-charged benzyl **GdL^{2}** and Mmc **GdL^{6}** or no substituent **GdL^{5}**. The lower affinities for **GdL^{1}** over its analogue **GdL^{2}** were evidenced across the series of evaluated guest molecules (Table S2.1). A change in charge of the MR reporting

moiety from positive Gd(do2a) to neutral Gd(do3a) logically reduced the affinity towards negatively charged groups in guests. On the other hand, the negatively remote pendants in complexes **GdL^{3,4}** exhibited the lowest affinities, whereby the more negatively charged phosphonate group influenced **GdL^{4}** to yield the lowest K_a values. This suggested that the increased charge of the 18C6 substituent caused stronger electronic repulsions with guests when approaching the paramagnetic label.

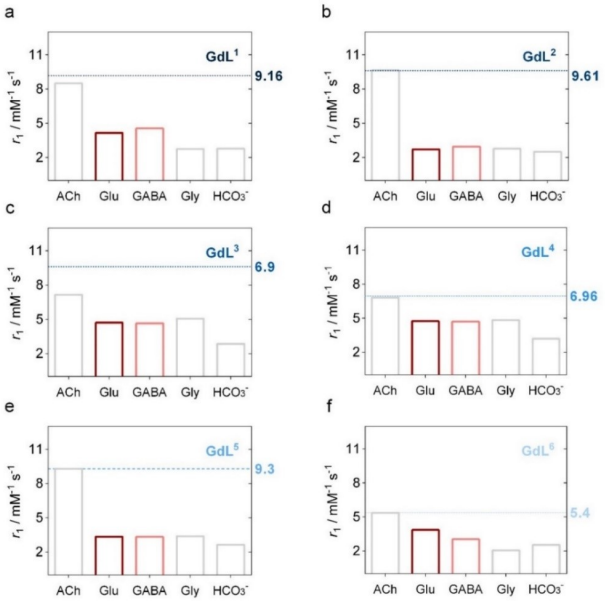

Figure 2.3. Relaxivity response of **GdL$^{1-6}$** to various analytes. (**a**)–(**e**) r_1 relaxivity of 3.0 mM **GdL$^{1-5}$** and (**f**) 1.0 mM **GdL^{6}** in 50 mM HEPES after the addition of 50 equiv. of various analytes at 25°C (pH 7.4, 300 MHz). Horizontal dotted lines illustrate the initial relaxivities of **GdL$^{1-6}$**. The values were obtained by the T_1w NMR titration, and the molar relaxivities were calculated according to Eq. S2.1.

In terms of specificity, it is found that **GdL^{1,2}** displayed greater affinity towards Glu over other NTs and hydrogencarbonates, yielding values of 72 and 311 M^{-1}, respectively, while all the synthesized complexes were ACh-insensitive (Figs. 2.3, S2.1, and Table S2.1). It was also noticed that **GdL^{6}** exhibited a higher affinity towards sterically less demanding Gly over GABA and Glu. The observed diversity in affinity patterns of **GdL$^{2-6}$** suggested a synergistic effect of several factors involved in the recognition process. More specifically, the milder downward trends and lesser change in r_1 for **GdL^{3,4}**, as well as the lower initial relaxivity for **GdL^{6}**, indicated that

an increase in size or the net negative charge of the 18C6 substituent impedes the interaction of NTs.

2.2.4 Luminescence Studies

The luminescence studies on **EuL^{3,5}** were performed to examine their solution structures and the impact of remote pendants on binding Gly.[276] In the first step, the luminescence emission spectra of both complexes before and upon addition of Gly were measured. The **EuL^{3}** complex showed more intense emission than **EuL^{5}**; however, upon saturation with Gly, the ternary adduct **EuL^{5}**(Gly) displayed more intense emission (Fig. 2.4). A recent study involving similar receptors evidenced that binding of NTs to the Eu^{3+}-chelate induced hyperchromicity of the hypersensitive $^5D_0 \rightarrow {}^7F_2$ transition at ~ 615 nm.[270] This increase is assigned to the coordination of carboxylate, which displaces the inner-sphere water(s), reducing the quenching rate of the $^5D_0$ excited state of Eu^{3+} ion.[98]

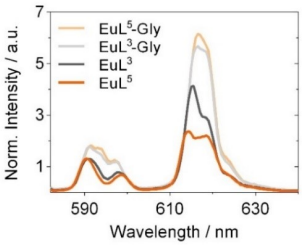

Figure 2.4. Luminescence characterization of **EuL^{3,5}** in response to Gly. The luminescence emission spectra of 5 mM **EuL^{3,5}** in HEPES (50 mM, pH 7.4), in the absence (solid lines) and after saturation (pale lines) with 50 equiv. of Gly at 25ºC. The maximal intensity of emission bands centered at 616 nm, corresponding to the $^5D_0 \rightarrow {}^7F_2$ transition of Eu^{3+}, was obtained upon direct excitation at 395 nm. Spectra were background corrected ($F\text{-}F_{HEPES}$).

In the following step, the non-radiative rate constants that characterize the depopulation of the $^5D_0$ excited state in H_2O and D_2O media were measured, and the hydration numbers were calculated for both hydrated complexes **EuL^{3,5}** and adducts **EuL^{3,5}**(Gly). The calculated *q* value for **EuL^{5}** yielded 1.76, which is twice as high as that of **EuL^{3}**. Furthermore, the addition of Gly decreased the hydration numbers of both complexes (Table 2.2). The greater drop of 0.87 occurred for **EuL^{5}**, pointing out that H_2O is displaced more readily than in the **EuL^{3}**, in which the change in hydration of 0.1 is almost negligible. The hydration number of **EuL^{5}** suggests the presence of two water molecules bound to the metal ion, which would imply that the oxygen atom of the propylamide group is not coordinated. This is in contrast with previous findings observed in structurally similar systems. These results indicate that small structural changes in the ligand may have a significant impact on the structural organization of the complexes.

Table 2.2. Luminescence lifetimes of complexes **EuL^{3,5}** before and after the addition of Gly (50 equiv.) measured at 616 nm from the decay profile of the $^5D_0$ excited state and the corresponding hydration numbers q.[a]

Complex	No neurotransmitter			+ 50 eq. Gly			
	τ_{H2O} [ms]	τ_{D2O} [ms]	q[b]	τ_{H2O} [ms]	τ_{D2O} [ms]	q[b]	Δq
EuL^3	0.51	1.11	0.81	0.52	1.07	0.71	0.1
EuL^5	0.4	1.44	1.67	0.58	1.55	0.80	0.87

[a] Conditions: ([**EuL^{3,5}**] = 5 mM, 50 mM HEPES, pH 7.4, 298 K). [b] q values were calculated using the modified Horrock's equation (Eq. S2.3).

The metal-centered emission spectra revealed diverse coordination environments for the hydrated complexes.[276, 277] Namely, **EuL^3**(H_2O) exhibited a larger intensity ratio for the magnetic-dipole transition $^5D_0 \rightarrow {}^7F_1$, which is almost insensitive to the local coordination environment, than for the electric dipole $^5D_0 \rightarrow {}^7F_2$ transition, which is strongly affected by the local symmetry of the Eu^{3+} ion and consequently by the nature of ligand atoms (Table S2.2).[278] These findings are suggestive of a **EuL^3**(H_2O) form in which a more polarizable ligand than water coordinates Eu^{3+}, which partly inhibits binding of Gly. Relying on these observations, it is hypothesized that the 18C6 acetate establishes a weak interaction in an intra- or intermolecular fashion with the Eu^{3+}, favoring a form in which the lanthanide ion is shielded, thus impeding the water coordination. If this is the case, the more polarizable Gly-carboxylate replaces the remote acetate pendant by disrupting this interaction, which should induce major conformational changes in **EuL^3** when Gly is added. However, the exchange of the acetate ligand with Gly in the coordination sphere of Eu^{3+} excludes water involvement, leading to small changes of q-value observed by time-resolved emission decay measurements.

Furthermore, **EuL^6**, having the coumarin-derived fluorophore, was characterized by fluorescence spectroscopy. However, the complex turned out to be non-emissive when the metal center was excited directly or via the chromophore. In addition, the fluorophore on **EuL^6** exhibited strong fluorescence emission intensity at 420 nm when excited at 330 nm, typical for coumarin derivatives (Fig. S2.2). The steady-state fluorescence emission experiments were also repeated in the presence of Gly or Glu, resulting in identical spectra to that of hydrated **EuL^6**.

2.2.5 Diffusion Studies

Diffusion-ordered 2D NMR spectroscopy allows separation of NMR signals based on the molecular diffusion.[279] Owing to the correlation between self-diffusion and the size/shape of molecular species ^{1}H DOSY-NMR is a readily used technique to disperse ^{1}H resonances along the diffusion axis, relating signals with differently organized forms of a solute.[280] To verify the hypothesis brought upon luminescence measurements, the ^{1}H NMR diffusion measurements on paramagnetic complexes **EuL^{3,5}** and their ternary adducts **EuL^{3,5}**(Gly) were performed, and the calculated hydrodynamic radii, assuming spherical shape of species (Table 2.3), were compared.[275, 281, 282] Firstly, the ^{1}H DOSY-NMR experiments on aqueous solutions of complexes **EuL^3** and **EuL^5** were recorded, as shown in Fig. S2.3. The obtained pseudo-

2D spectra for **EuL^3** identified two distinct sets of ^{1}H resonances with corresponding different diffusion constants (*D*), while the hydrated **EuL^5** complex resonated along one diffusion value. Following this step, the diffusion measurements were repeated after the addition of Gly (50 equiv.), revealing the disappearance of the resonances corresponding to the faster-diffusing form in **EuL^3**(Gly). On the contrary, no changes in diffusion of the slower diffusing form in **EuL^3**(Gly) or diffusion of **EuL^5**(Gly) were observed. These results indicate that two solution forms of **EuL^3** are in dynamic equilibrium, in which the form with a smaller hydrodynamic radius underwent structural changes in the presence of Gly. The presence only of a form with the greater hydrodynamic radius eliminated the probability of **EuL^3** aggregates self-organizing intermolecularly into dimeric form. Indeed, it becomes clear that the formation of **EuL^3** with a smaller diameter is due to the weak intramolecular coordination of 18C6 acetate to coordinatively unsaturated Eu^{3+}, which brings closer the two binding sites, establishing a sort of folded conformation with reduced hydrodynamic radii. Addition of Gly displaces the 18C6 acetate from Eu^{3+}, resulting in the formation of the ternary adduct **EuL^3**(Gly), as illustrated in Fig. 2.5.

Table 2.3. Diffusion coefficients (*D*) obtained in ^{1}H DOSY NMR experiments and the corresponding calculated hydrodynamic radii (R_h).[a][b]

Complexes	EuL^3	EuL^3 + Gly	EuL^5	EuL^5 + Gly
D / (10^{-10} m^2 s^{-1})	2.57 3.19	2.57	3.81	3.81
R_h / (nm)	1.91 1.54	1.91	1.29	1.29

[a] Conditions: [**EuL^{3,5}**] = 10 mM in D_2O, pD 7.8, 298 K, 300 MHz; [b] Hydrodynamic radii R_h are calculated according to the Einstein-Stokes relation (Eq. S2.4).

These observations are in good agreement with results obtained in the relaxometric titrations and luminescence emission experiments. Namely, the existence of dynamic equilibrium in **LnL^3**, involving folded and non-folded forms, resulted in lower hydration and consequently lower initial r_1 relaxivity. The changes of r_1 observed upon addition of Gly likely occurred due to displacement of inner-sphere water in the non-folded **EuL^3** form, eventually leading to disappearance of the intramolecular self-assembly. On the contrary, the **GdL^5** exists only in the non-folded conformation, leading to the higher initial relaxivity, the greater change in *q*-value, and the corresponding drop in r_1 relaxivity upon saturation with analytes.

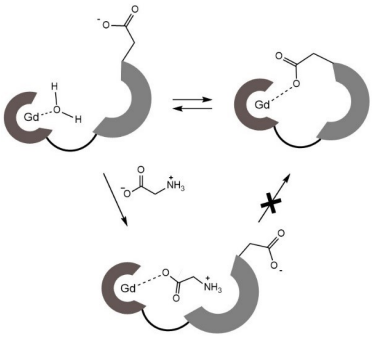

Figure 2.5. Schematic presentation of two forms of the hydrated complex **EuL³** and the proposed binding mechanism with Gly. In Gly-free form, receptor **EuL³** exists in a dynamic equilibrium of two forms: open and intramolecular self-assembled, where acetate on 18C6 ether binds Gd^{3+}, blocking water coordination. The addition of Gly disturbs Gd-acetate interactions, shifting equilibrium towards the **EuL³**(Gly) adduct, followed by the disappearance of intramolecular self-assembly.

2.2.6 DFT Calculations

Theoretical calculations were carried out to rationalize the different behavior of the **GdL³** and **GdL⁵** complexes and provide support to the interpretation of relaxometric, luminescence, and ^{1}H DOSY experiments. First, it analyzed the feasibility of the acetate pendant at the 18C6 moiety to coordinate paramagnetic ions in an intramolecular manner. Then, the [**GdL³**$(H_2O)_2 \cdot 4H_2O$] system was modeled, which included two water molecules coordinated to the metal ion and four additional second-sphere water molecules. The explicit inclusion of a few second-sphere water molecules was done because it was previously found to be essential for providing a good description of the $Gd-OH_2$ distances and the spin densities at the ^{17}O nucleus.[283,284] The calculation provided an energy minimum that contained two water molecules coordinated to the Gd(III), which presents the typical capped SAP coordination environment in this type of complex. Next, we explored the potential energy surface by approaching the remote carboxylate group to the metal ion, which eventually leads to a second energy minimum in which the carboxylate group coordinates to Gd^{3+} by replacing the coordinated water molecule, as shown in Fig. 2.6. Indeed, these calculations indicated that coordination of the remote carboxylate group is feasible. Moreover, DFT predicts a very small energy difference between the two energy minima (folded and non-folded species), favoring the open form by only 1.4 kJ mol^{-1}. Calculations performed on the **GdL⁴**$(H_2O) \cdot 5H_2O$ system (Fig. 2.6b) also suggested that coordination of the phosphonate group attached to the crown moiety is likely responsible for the lower binding affinity of this complex toward NTs.

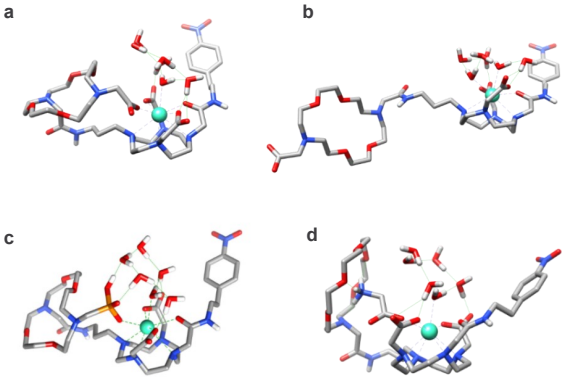

Figure 2.6. DFT computational studies of interactions between hosts **GdL^{3,4,5}** and Gly guest. Calculated structure of the modeled **GdL^{3}**$(H_2O)_2{\cdot}4H_2O$ system illustrating (**a**) the self-assembled form where the acetate on 18C6 coordinates the metal ion and (**b**) the hydrated open form (right). (**c**) Self-assembly of the **GdL^{4}**$(H_2O){\cdot}5H_2O$, showing coordination of the remote phosphonate group to the metal ion. (**d**) Structure of the **GdL^{5}**$(Gly)(H_2O){\cdot}5H_2O$ system depicting ditopic binding of Gly.

Calculations were performed on the [**GdL^{5}**$(H_2O)_2{\cdot}4H_2O$] and [**GdL^{5}**$(Gly)(H_2O){\cdot}5H_2O$] systems to gain insight into the molecular recognition process. The calculations were done by using three model systems with the Gly guest interacting with either the 18C6 binding site or the lanthanide ion and a third form in which Gly is ditopically bound, shown in Fig. 2.6. The corresponding energy differences provided an estimate of the contributions to the overall recognition process of the coordination to the metal ion and the hydrogen bonding interaction with the 18C6 moiety, which turned out to be 17.3 and 9.7 kJ mol^{-1}. Thus, these calculations indicate that binding to the coordinatively unsaturated Gd(do2a) unit represents the major driving force of the molecular association process, though the hydrogen-bonding interaction with the 18C6 moiety also provides a sizeable contribution to the overall binding energy.

2.3 Conclusions

Herein, the scope of Gd-based ditopic MRI probes sensitive to amino acid NTs was expanded, and the structure-affinity relationship through the relaxometric response was revealed. The results indicated that the charge-neutral H_3do3a-derived **GdL^{1}** displayed reduced affinity over H_2do2a-based analogue **GdL^{2}**, while adding the negative charge on the 18C6 binding site reduced the affinity towards guests. The key finding in this study was that **GdL$^{2-6}$** provided relaxometric response in a manner governed by the nature of the 18C6 pendant. Specifically, the substituent at the 18C6 moiety favors disposition of the binding sites in a charge/size-dependent manner,

which governs recognition of the guests. The observed Δr_1 trends revealed that increases in the size of the pendant elevate steric hindrances, resulting in lower initial relaxivities but only slightly diminishing the strength of interactions with guest molecules. Besides the steric hindrances, the electronic factor in the complexes with negatively charged pendants **GdL^{3,4}** unfavored host-guest association to a greater extent. In addition, the achievement of great importance in the study is finding that **GdL$^{1-2}$** displayed higher affinity towards Glu over competitive bicarbonate. The findings present a breakthrough in understanding the nature of interactions between the ditopic MR platforms consisting of DO3A-/DO2A-derived units and 18C6 derivatives with the NTs. Owning the ability to produce an excellent change in relaxivity, these MRI probes present a potent concept for further development of bioresponsive CAs that can visualize fluctuations in synaptic concentration of the most abundant NTs by means of T_1w MRI. In addition, the results of this study can be used as a guideline for the development of novel concepts within functional MRI for sensing chemical neurotransmission.

Chapter 3

A Low-Molecular-Weight Ditopic MRI Probe for Ratiometric Sensing of Zwitterionic Amino Acid Neurotransmitters

Non-invasive mMRI is often impaired by a lack of selectivity of chemosensors for the desired guest molecule. The host-guest selectivity between a molecular sensor and a target biomarker could be achieved by careful design of receptor sites of a host to match complementary groups of a guest. Here we report the synthesis and evaluation of a novel Gd(III)-based probe for multipoint binding to zwitterionic amino acid neurotransmitters crafted for ratiometric MRI imaging. The probe showed increased binding affinity to Glu and GABA, displaying co-occurrence of non-synchronized, concentration-dependent changes of the r_1- and r_2-relaxivity. Through the application of a T_2/T_1-weighted MRI strategy, we demonstrated signal enhancement for cooperatively bound Glu and GABA over bicarbonate, which remained MR silent.

Published as:
Chem. Commun. **2019,** *15,* 11924-11927
https://doi.org/10.1039/C9CC06463J
Đorđe Toljić, Goran Angelovski*

3.1 Introduction

Signal intensity of *in vivo* CE MRI involving responsive CAs, among the properties of a probe, depends on the actual concentration of the imaging probe and the volume of the observed region. This makes it difficult to quantify the target stimuli since it is impossible to measure the exact concentration of CA due to various processes occurring in the body.[140] Since that concentration of CA is not homogenous through the observed region, the signal intensity will differ from voxel to voxel, which in turn will lead to a wrong conclusion on the concentration of the interacting stimuli. This issue is successfully resolved through the implementation of a ratiometric T_2/T_1 MRI pulse sequence, which eliminates the concentration factor. In addition, the other benefit of MRI ratiometry is sensitivity improvement of synthetic sensors in response to environmental stimuli over conventional T_1- and T_2-weighted MRI approaches.[216]

Molecular recognition between magnetic host sensors and guest molecules occurs *via* the formation of a ternary adduct, and it is evaluated through binding affinity.[285, 286] In the case of a turn-off response host-guest design, the interaction of biomarkers with the coordination cage of an MR probe restricts water accessibility to the paramagnetic center, resulting in a signal decrease. In terms of host–guest interaction, the low-molecular-weight ditopic sensors responsive to AAs are bismacrocyclic Gd(III)-based complexes with a DO2A derived chelator, whose geometry allows for easy access to small anions. In particular, the selectivity of the current sensors is greatly hindered by HCO_3^-, which binds in a similar fashion as the AAs. Owing to a high extracellular concentration of ~25 mM, small molecular size, and consequently low steric hindrances, it predominantly binds to the paramagnetic label, thus preventing selective interaction with amino acid NTs.[271] On the other hand, the advantageous feature of NTs is their existence in the form of an ion-pair entity at physiological pH, which opens the possibility of exploiting a ditopic platform to strengthen binding through cooperativity.[287]

In accordance with this, different binding modes may unequally affect parameters such as inner-sphere water exchange rate or molecular tumbling, which determine both r_1 and r_2 relaxivities. In turn, the occurrence of non-synchronized changes of r_1 and r_2 would allow for the utilization of the ratiometric r_2/r_1 MRI approach.[139-141, 288] In order to develop such a sensor, it is necessary to evoke non-synchronized stimuli-induced changes of parameters that determine r_1 and r_2. Therefore, we set out to exploit the cooperative binding potential of a ditopic low-molecular-weight Gd(III)-chelate to improve the sensing of NTs. In support of this study design is the claim that the rate of water exchange in cationic Gd-complexes is dependent on the nature of the counter-anion.[289]

3.2 Molecular Design

The probe design consists of a bismacrocyclic framework, providing receptor sites to favor cooperative ion-pair binding of amino acid NTs. The host-guest interactions involve simultaneous coordination of the carboxylate to coordinatively unsaturated

Gd^{3+} and multiple hydrogen bonds established between the 18C6-derived receptor and the NH_4^+ terminal of NTs (Fig. 3.1).

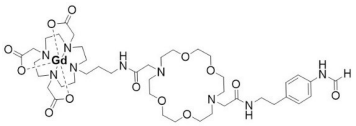

GdL^7

Figure 3.1. Chemical structure of the proposed ditopic MRI chemosensor, **GdL^7**. The design rationale for the probe with improved selectivity to GABA and Glu is based on findings achieved in Chapter 2.

The choice of an H_3dota-derived ligand for a Gd-based MR transducer over the coordinatively less saturated H_2do2a is due to its higher selectivity towards carboxylates from NTs over HCO_3^-, owing to stronger electronic repulsions from the acetate pendant arms. To reinforce the affinity towards the ammonium cation, the formanilide pendant that bears two amide groups, one proximate and one distant to the 18C6 ring frame, was introduced. Relying on findings observed in previous studies involving similar MRI sensors in which the two binding sites adopt a shell-like conformation, which brings a remote pendant into the vicinity of binding pocket[152], it is anticipated that the amides could engage as the H-bond donors and additionally contribute guest to recognition. The role of the flexible amide linker is to preserve the high degree of conformational mobility of the two binding sites, providing an adoptable geometry for cooperative binding of zwitterions.

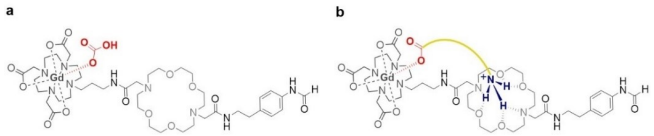

Figure 3.2. Binding modes of **GdL^7** depicting interactions with structurally different guests. (**a**) Monotopically bound HCO_3^- and (**b**) ditopically bound amino acid NTs.

3.3 Results and Discussion

3.3.1 Synthesis of ditopic receptor GdL^7

The bismacrocyclic complex **GdL^7** is synthesized by bridging two macrocyclic components, followed by complexation with Gd^{3+} (Scheme 3.1). The 18C6 fragment **3-1** was prepared by direct mono N-alkylation of 1,10-diaza-18-crown-6 ether with **2-4**, while the DO3A *tert*-butyl ester-derived bromide **2-2** was prepared according to the previous procedure introduced in Chapter 2. The macrocyclic precursors **3-1** and **2-2** were covalently linked to form bismacrocyclic derivative **3-2.** As the preparation of bismacrocycles of this type is often limited by a bridging step, the yield of 62% can

be considered excellent. In the following step, the aromatic nitro group of **3-2** was subjected to $Pd(OH)_2$/C-catalyzed hydrogenation to afford the amine **3-3.** Simultaneous hydrolysis of the *tert*-butyl esters and conversion of the amine into formamide were conducted in formic acid to obtain the final ligand **L^7** with a yield of 64% and a ratio of isomers of 28:72. The complexation was performed in water media at neutral pH with $GdCl_3$ to give the corresponding complex **GdL^7**. To avoid entrapment of a Gd^{3+} within the 18C6 component, the complexation was performed using a ligand-to-Gd ratio of 1.0:0.8, and the excess of ligand was effectively removed by the reverse-phase HPLC. The absence of free Gd ions was additionally confirmed by the xylenol orange test.[290]

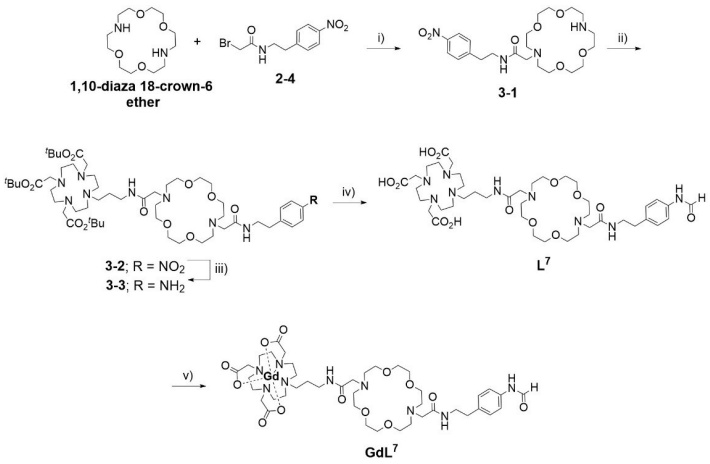

Scheme 3.1. Synthesis of **GdL^7**. *Reagents and conditions:* i) $NaHCO_3$, MeCN, 45ºC, 52%; ii) **2-2**, DMF, $NaHCO_3$, RT, 3 days, 62%; iii) H_2, $Pd(OH)_2$/C (20 wt. %), EtOH, 3.1 bar, 84%; iv) HCO_2H, 65ºC, overnight, 64%; v) $GdCl_3$, H_2O, pH 7.2, 60ºC, 4h, 74%.

3.3.2 Relaxometric Properties of the GdL^7

The formation of ternary adducts of **GdL^7** with different analytes, the amino acid NTs (Glu, Gly, GABA), non-zwitterionic transmitter Ach, and competitive metabolite HCO_3^-, were monitored by measuring T_1 and T_2 relaxation times of surrounding bulk water protons in relaxometric titrations, and the corresponding molar r_1 and r_2 relaxivities were calculated to Eq. S2.1. The initial values calculated for r_1 and r_2 were 10.14 and 13.46 mM^{-1} s^{-1}, respectively, whereas titration with analytes yielded downward trends revealing that **GdL^7** is ACh-insensitive, while the HCO_3^- exhibited a comparable drop in r_1 (69%) to the NTs that induced r_1 decrease, ranging from 61 to 69% (see Figs. 3.3 a,b, and S3.1). However, notably diverse r_2 changes between HCO_3^- and NTs were observed. Upon saturation with the guests (60 equiv.), the r_2 of ternary

adduct **GdL^7**(HCO_3^-) was 3.69 mM^{-1} s^{-1}, while the values for the -Gly, -Glu, and -GABA adducts were 5.64, 5.78, and 5.89 mM^{-1} s^{-1}, respectively. The gathered results are in agreement with the simulations performed for low-molecular-weight GBCAs at high magnetic fields (> 1.5 T).[4] Namely, the T_1 is relatively constant over a broad range of values for the τ_m and τ_R parameters. On the contrary, for the same parameters, T_2 undergoes a rather drastic change. Hence, the co-occurrence of non-synchronized changes of T_1 and T_2 opened the possibility to implement an r_2/r_1 ratiometric MRI strategy.[141, 288] When presented as the r_2/r_1 ratio, there is an increase from the initial value of 1.32 for **GdL^7** to 1.7, 1.9, and 2.1 in the presence of Gly, Glu, and GABA, respectively (Fig. 3.3c,d). In the case of HCO_3^-, the decrease in r_1 is followed by a proportional decrease in r_2, resulting in insignificant fluctuations for the r_2/r_1 values over the entire titration range.

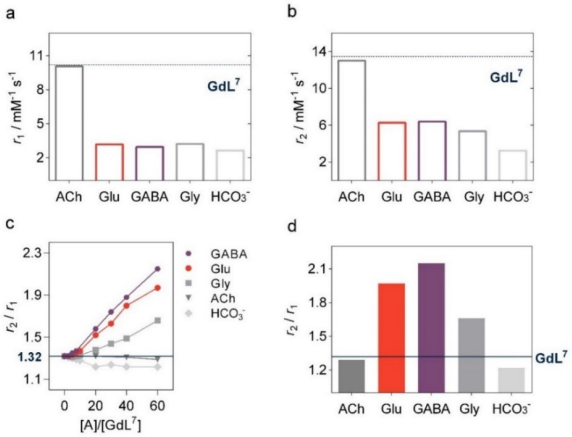

Figure 3.3. Relaxometric characterization of **GdL^7**. The schematic depiction of measured (**a**) longitudinal (r_1) and (**b**) transverse (r_2) relaxivities for 2.5 mM **GdL^7** in the presence of 60 equiv. of analyte in 50 mM HEPES (pH 7.4, 300 MHz) at 25°C. The horizontal dotted lines represent the corresponding relaxivities in the absence of analytes. (**c**) Ratiometric r_2/r_1 stimuli-dependent response over the range of added analytes from 0 to 60 equiv. (**d**) Corresponding calculated r_2/r_1 ratio after the saturation point is reached (60 equiv.). The horizontal full lines represent the r_2/r_1 ratio in the absence of analytes.

The binding affinities were obtained from the mono-exponential fit of r_1 curves to Eq. S2.2 (Table 3.1). Comparison of affinity constants revealed higher values of 116 and 106 M^{-1} for GABA and Glu, respectively, over HCO_3^- and Gly, which were 86 and 64 M^{-1}, respectively. The observed trends suggested greater structural complementarity of the receptor-binding pocket to the long-chain NTs, Glu and GABA. The decreased affinity of Gly compared to GABA and Glu is likely due to the absence of cooperative host-guest binding, as the carboxylate-amine terminals in GABA and Glu are more suited to the spatial disposition of binding sites within **GdL^7**.

Table 3.1. The water proton r_1 decreases and affinity constants (K_a) for the ternary complexes **GdL^7**(A) in 50 mM HEPES (298 K, pH 7.4, 300 MHz).[a]

analyte (A)	Gly	Glu	GABA	ACh	HCO_3^-
K_a [M^{-1}]	64	106	116	N/A	86
-Δ r_1 [%]	68	69	71	N/A	75

[a] The complex to analyte ratio is 1:60.

3.3.3 Conformational mobility of 18C6 motif in response to analytes

The conformational mobility of the binding sites in the host molecule is affected by the interactions with guest molecules.[291, 292] Therefore, to gain insight into the host-guest binding modes, various NMR studies were performed involving the diamagnetic yttrium(III) analogue, **YL^7**. High-resolution ^{1}H NMR spectra were recorded with **YL^7** in the presence of 20 equiv. of Glu or HCO_3^-. The complexation-induced resonances of both ternary complexes shifted upfield, with a more pronounced effect for Glu, which suggests its stronger host-guest interactions (Fig. S3.2). Furthermore, splitting of a broad signal at 1.69 ppm in ternary adducts, corresponding to the methylene $CH_2\underline{CH_2}CH_2$ of the amide linker that connects the two binding sites, suggested the existence of two conformers, corresponding to both bound and non-bound forms.[293] Overall, this revealed host-guest binding with a slow exchange rate and a greater magnitude for **YL^7**(Glu) interaction. Anion binding to the paramagnetic label coordinated by DO3A-based chelates is well documented,[294, 295] and thus, we focused on the investigation of interactions that involve the 18C6 binding site. The 2D EXSY NMR spectra displayed conformational diversity for the 18C6 moiety within the ternary adducts (Figs. 3.5 and S3.10 to S3.12). The greater density of cross-peaks in **YL^7**(Glu) pointed towards a binding mode that involves multiple interactions between the 18C6 and the NH_4^+.[296] Conversely, the more defined cross-resonances for 18C6 in **YL^7**(HCO_3^-) were assigned to Na^+ inclusion (bicarbonate was added as the monosodium salt).[297] Moreover, no change was observed in the ratio of isomers in the ^{1}H NMR spectra, which excluded involvement of the formanilide pendant in binding.

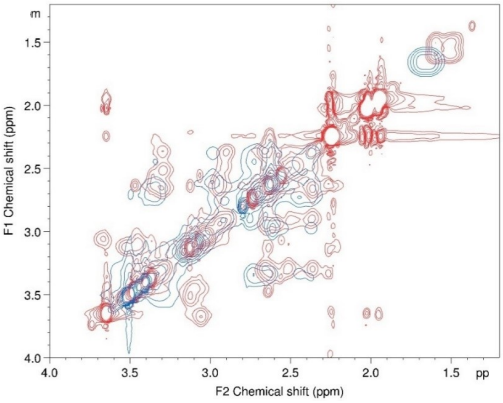

Figure 3.5. Partially overlapped 2D EXSY NMR spectra of **YL^7** (gray) and **YL^7**(Glu) (red) in D_2O (pD 7.8, 800 MHz) at 25°C.

Another parameter sensitive to molecular motions of bound protons is the T_1 relaxation time.[291] Thus, to quantify the observed conformational flipping, the T_1 values of protons in the $NCH_2\underline{CH_2}O$ groups within the 18C6 fragment and *meta*-H in the remote pendant (Table 3.2 and Fig. S3.3) were measured. The acquired T_1 values for the 18C6 moiety in the **YL^7**(Glu) and **YL^7**(HCO_3^-) were 692 ms and 651 ms, respectively, whereas the one for binary **YL^7** was measured to be 628 ms. The elevated T_1 value in the presence of Glu indicated a higher rate of conformational exchange of the 18C6 binding site. This was rationalized as the impact of reversible interactions of multiple bifurcated hydrogen bonds between NH_3^+ of the zwitterion and free electronic pairs on the heteroatoms in the 18C6 receptor.[298, 299] Slightly increased mobility of the 18C6 moiety in monotopically bound **YL^7**(HCO_3^-) is likely related to stronger interaction with entrapped Na^+. The identical trend of mobility was observed for the 18C6 pendant (Table 3.2), which is in alignment with a higher degree of freedom for linear compounds. Clearly, the observed trends in spin-lattice relaxation times pointed to the involvement of both binding sites within the MRI host in the case of **YL^7**(Glu), which is suggestive of a ditopic binding mode.

Table 3.2. Fitted T_1 values measured for the $NCH_2\underline{CH_2}O$ fragment within the 18C6 ring frame and for the *meta*-H of the remote pendant. [a][b]

Complexes	$T_{1,\ (CH_2)}$ / (ms)	$T_{1,\ meta\text{-}H}$ / (s)
YL^7	628	2.82
YL^7(HCO_3^-)	651	2.89
YL^7(Glu)	692	3.08

[a] [**YL^7**] = 15 mM, pD 7.8, 298 K, 800 MHz. [b] **YL^7** to analyte ratio 1:20.

^{1}H DOSY NMR measurements provided insight into host-guest association in solution.[300] The obtained self-diffusion constants displayed faster translational motion for the ternary adducts, **YL^7**(Glu) and **YL^7**(HCO_3^-)**,** compared to the binary **YL^7** (Table 3.3 and Fig. S3.4). The corresponding hydrodynamic radii, calculated using Eqn S2.4, shrunk from 1.54 nm to 1.29 nm upon moving from the binary complex to the ternary species, suggesting a different spatial arrangement of **YL^7** prior to its interaction with guests. These values excluded the formation of aggregates or intermolecular self-assembly. The rotational correlation times (τ_R) were identical for the ternary complexes (243 ps), which ruled out tumbling as the explanation for the observed diversity in T_2 trends.

Table 3.3. Self-diffusion coefficients (*D*) obtained in the ^{1}H DOSY NMR experiment and the calculated hydrodynamic radii (R_h) and rotational correlation time (τ_R) for **YL^7**(H_2O) and ternary adducts **YL^7**(Glu) and **YL^7**(HCO_3^-).[a]

Complexes	**YL^7**(H_2O)	**YL^7**(Glu) [b]	**YL^7**(HCO_3^-) [b]
Diffusion coefficient ***D*** (x 10^{-10} m^2 s^{-1})	3.19	3.81	3.91
Hydrodynamic radii R_h (nm)	1.54	1.29	1.29
Rotational corr. time τ_R (ps)	414	243	244

[a] [**YL^7**] = 15 mM, pD 7.8, 298 K, 300 MHz. [b] Host-to-guest ratio 1:20.

3.3.4 MRI Phantoms

To capitalize on this effect, the selectivity of the **GdL^7** probe was tested by comparing the signal enhancements of T_1w and T_2w with T_2/T_1w[301] images of MRI tube phantoms in a 7.05 T MRI scanner (Fig. 3.5, S3.5, S3.6, and Tables 3.4 and S3.1). The contrast enhancements were calculated as differences in obtained SNR. The T_1w image gave negligible ΔSNR for Gly, GABA, and Glu with respect to the signal enhancement produced by HCO_3^-, which are in the range 1–4%. On the other hand, HCO_3^- caused greater MRI signal alteration in the T_2w images, thus masking the effect of other NTs. Specifically, Gly, GABA, and Glu only reached 70, 47, and 57% of the signal enhancement observed for HCO_3^-, respectively. In contrast to the results obtained using T_1w and T_2w MRI protocols, the T_2/T_1w phantoms gave more intense signals for GABA, Glu and Gly (11, 10, and 4%, respectively). Moreover, HCO_3^- remained completely MRI silent with the ΔSNR equal to that of **GdL^7**. In addition, comparing the greater potential of the T_2/T_1w MRI protocol to the commonly used T_2w analogue to produce images with greater SNR, it should be noted that effective discrimination of HCO_3^- was successfully achieved under the physiologically relevant conditions.

Table 3.4. The SNR changes (ΔSNR) obtained in T_1w, T_2w, and T_1/T_2w MRI phantom experiments for **GdL^7** versus **GdL^7**-analytes in the ratio 1:60. [a]

ΔSNR	GdL^7/GdL^7(HCO_3^-)	GdL^7/GdL^7(Glu)	GdL^7/GdL^7(Gly)	GdL^7/GdL^7(GABA)
T_1w	47	43	45	46
T_2w	188	107	131	89
T_1/T_2w	0	10	4	11

[a] ΔSNR values were calculated using the following formulas: i) T_1w: ΔSNR = (|1-SNR **GdL^7**(analyte)/SNR **GdL^7**|)·100; i) for T_2w and T_1/T_2w: ΔSNR = (|1-SNR**GdL^7**/SNR**GdL^7**(analyte)|)·100.

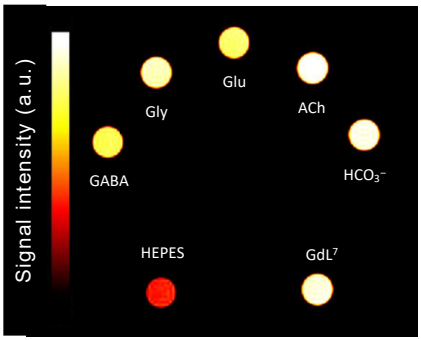

Figure 3.5. T_1/T_2w MRI phantom image of 1.5 mM **GdL^7** in the presence of various NTs and competitive metabolites (60 equiv.) in 50 mM HEPES (pH 7.4, 7 T) at 25°C. The image was acquired using a Steady State Free Precession (bSSFP) pulse sequence.[301]

3.4 Conclusions

The novel ditopic Gd(III)-based MRI probe with an increased binding affinity towards GABA and Glu was developed, and the r_2/r_1 imaging strategy was employed to discriminate from their physiological competitor, HCO_3^-. It is demonstrated that cooperative binding of bidentate guests induced co-existence of uneven changes of r_1 and r_2 in the supramolecular adducts. Unlike the long-chain NTs, the monotopically bound HCO_3^- induced a proportional decrease in both r_1 and r_2, whose ratio remained equal to that of unbound **GdL^7**. Hence, the greater SNR changes were observed for GABA and Glu in MRI phantoms and were less emphasized for Gly. Overall, these findings establish an efficient strategy to sense polydentate metabolites by employing low-molecular-weight polytopic MRI probes. It is anticipated that the introduced concept of utilizing a polytopic host with a ratiometric imaging methodology will be beneficial in the future development of MRI probes for quantification of polycharged guest molecules.

Chapter 4

Translating a Low-Molecular-Weight MRI Probe Sensitive to Amino Acid neurotransmitters into a PAMAM Dendrimer Conjugate: The Impact of Conjugation

The application of MRI CAs to diagnose neurodegenerative diseases requires the ability of CAs to cross the blood-brain barrier. Towards resolving this issue, the present approach is designed to investigate the impact of the G 4.0 PAMAM dendrimer scaffold, as a biocompatible carrier, on the performance of a surface-conjugated Gd-based bismacrocyclic sensor sensitive to amino acid neurotransmitters. In this work, we investigated the effect of dendrimeric surface morphology on the initial r_1 and r_2 relaxivities and induced relaxivity in response to structurally similar guest molecules. However, this approach requires a minimal structural modification on a small molecule necessary to provide a functional group for anchoring to the nano-scaffold, which in turn might affect the overall performance of the obtained MRI-responsive nanoconjugate.

Published as:
ChemNanoMat. **2019**, *5*, 1456-1460
https://doi.org/10.1002/cnma.201900552
Đorđe Toljić, Goran Angelovski*

4.1 Introduction

Multicomponent supramolecular systems are increasingly used in drug delivery and targeting applications as they are capable of overcoming obstacles that are beyond the limits of monocomponent small-molecule entities.[302, 303] In this sense, the synergistic functionality of nanosized carriers and responsive MRI-active low-molecular-weight receptors integrated as biocompatible conjugates provides advantageous features over a single MR-responsive entity.[304, 305] For instance, Gunduz *et al.* demonstrated improved sensitivity of Ca^{2+} MRI-responsive dendrimeric sensor conjugate over a non-conjugated sensor.[216] The common approaches used to translate small-sized MRI CAs into bioresponsive NPs are *via* the incorporation of a probe as a structural element,[306] physical encapsulation into an internal void through non-covalent interactions[307] and covalent attachment[308]. However, loading of responsive CAs by attaching them onto the surface of NPs is always challenging, as the responsive MR conjugate should keep its functionality, *i.e.,* remain exposed to the desired stimuli in its microenvironment.[169, 309]

One of the drawbacks associated with the low-molecular-weight Gd-based MRI CAs is fast clearance from the body.[310-312] A straightforward way to overcome this issue is *via* conjugation to a slow-diffusing nanosized carrier.[303, 313-315] Towards this goal, a suitable choice of nano-sized scaffold is the family of well-investigated water-soluble PAMAM dendrimers of higher generations, owing to properties such as high loading capacity, biocompatibility, stability, and ease of functionalization.[199, 316] For this reason, the PAMAM dendrimers were imposed as the appropriate candidates to be used as nano-scaffolds.[317] However, the dendrimeric surface charge plays an essential role in the pharmacokinetic properties.[318] Considering toxicity, negatively charged peripheral groups are more desired; nevertheless, negative charges on the terminals, for instance, carboxylate groups, are likely to interfere with the paramagnetic label incorporated within the MRI-responsive chelates.[319] On the other hand, a positively charged surface appended with, e.g., amine groups, is more toxic but would not interfere with the paramagnetic cations and their performance.[320] In addition, dendrimers with the charge-neutral surface exhibited affirmative biocompatibility profiles and were considered as carriers for imaging agents.[218, 321] Hence, the development of stimuli-responsive nano-sized conjugates requires a compromise between solubility, toxicity, and sensitivity towards the target molecules.

Although the dendrimeric tail-conjugates might be designed to release payload in response to biological stimuli[322] the previously reported non-degradable Ca-sensitive PAMAM-CAs conjugate coined for the ratiometric r_2/r_1 MR imaging strategy displayed improved sensitivity to Ca^{2+}.[216] Additionally, investigation into small-sized ditopic MR receptors evidenced their potential to selectively bind zwitterionic NTs *via* cooperative ion-pair binding.[270, 271] These responsive, small-sized GBCAs shown to be a promising tool for visualization of Glu and GABA by means of a ratiometric T_1/T_2 approach (Chapter 3). One negative aspect associated with these types of small-molecule charged MRI probes is their intrinsic incompatibility with penetrating the BBB and reaching the region of interest, which limits their

application to terminal experiments in biomedical research. Hence, an improvement in biocompatibility is an imperative.

4.2 Molecular Design

To prepare the nano-sized probe of interest, a G4 PAMAM dendrimer with a cystamine core and 64 amine terminals was used as a multivalent binding platform for conjugation with a small-sized Gd(III)-chelate sensitive to AAs (Fig. 4.1). For the molecular MRI-active component, the previously developed bismacrocyclic receptor described in Chapter 3 was used. The flexible pending arm attached to the 18C6 moiety was chemically modified and used for bridging *via* covalent linkage to the primary amine terminals on the PAMAM dendrimer. To neutralize the surface charge and increase solubility at physiologically relevant pH, the remaining non-functionalized peripheral amines were capped with the mPEG-6 units.[323] The short chain length for the hydrophilic mPEG unit, consisting of six repeating building blocks, was chosen to minimize steric hindrances and thus ease the accessibility of guest molecules to the receptor binding sites. The detection principle is based on the *q*-modulation principle, involving reversible binding of the AAs with the appended ditopic chelate in an ion-pair cooperative manner.[324]

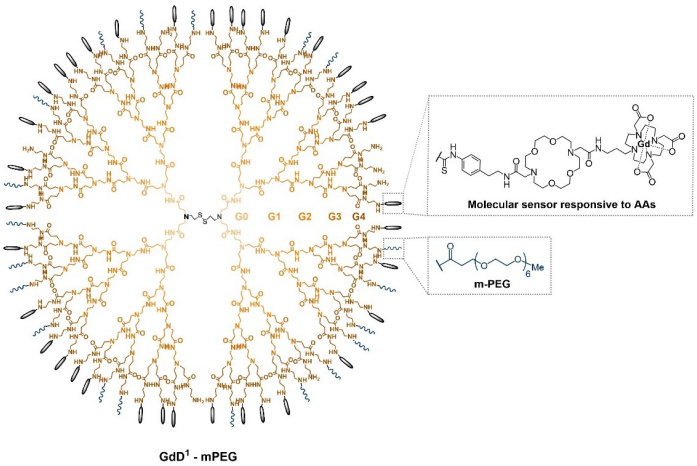

Figure 4.1. Structure of nano-sized MRI probe sensitive to AAs, **GdD^1-mPEG**. The G4 PAMAM dendrimer represents a nano-scaffold onto whose surface were co-attached the responsive MR transducer **GdL^7** and the hydrophilic PEG component.

4.3 Results and Discussion

4.3.1 Synthesis and Structural Elucidation

The multi-step synthetic route for the preparation of the dendrimeric-conjugate **GdD^1-mPEG** consisted of the synthesis of *tert*-butyl ester protected and bismacrocyclic isothiocyanate **4-1** (Scheme 4.1), followed by its attachment onto the G4 PAMAM surface, hydrolysis, metalation, and PEGylation (Scheme 4.2). In the first step, the precursor for the bismacrocyclic chelator, the amine **3-3** (Scheme 3.1 in Chapter 3), was reacted with $CSCl_2$ to yield the isothiocyanate **4-1**. The choice of isothiocyanate as the desired functional group for the conjugation to the primary amine surface was made, as it is known to undergo reaction in a facile manner under mild conditions.

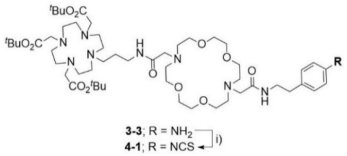

Scheme 4.1. Synthesis of isothiocyanate **4-1**. *Reagents and conditions.* i) $CSCl_2$, CH_2Cl_2, Et_3N, 4 h, RT, 47%.

In the following step, **4-1** was covalently attached to the amine-terminated surface of a G4 PAMAM dendrimer through the formation of thiourea bridges to yield the dendrimeric conjugate **4-2**. Subsequently, the *tert*-butyl esters were cleaved in formic acid to afford the corresponding PAMAM-conjugated ligand **D^1**. The complexation of ligand **D^1** was carried out with $GdCl_3$ at pH 7.2, providing the nanoconjugate **GdD^1**. The final product was subsequently treated with EDTA to remove the excess of free Gd^{3+}. Due to its tendency to precipitate in HEPES-buffered media at physiological pH, the remaining positively charged dendrimeric amine surface was neutralized by PEGylation with hydrophilic mPEG-6-NHS ester units to yield the final PAMAM-conjugate **GdD^1-mPEG**.

The average number of conjugated NT-responsive units per G4 PAMAM dendrimer core in **GdD^1-mPEG** was determined by ^{1}H NMR analysis in two different stages in the synthesis of the nano-conjugates. For the dendrimeric intermediates **4-2** and **D^1**, an average functionalization of 36 peripheral amines out of 64 (56%) was estimated. An average mass of conjugates calculated according to the dendrimeric loading estimated *via* the ^{1}H NMR experiment was shown to be in good correlation with the mass distribution peaks obtained from MALDI-TOF analysis. However, due to peak broadening, which is a consequence of a wide mass distribution range, this type of analysis prevented more precise characterization. The groups conjugated on the periphery in higher-generation dendrimers are known to be densely distributed, and therefore, partial occupancy exceeding 50% is satisfactory for these types of Gd-chelates. In addition, when compared to the similar but sterically smaller MR

chelates,[325] it is clear that sterically bulky **4-2** is causing steric hindrances, which prevent loading of a greater number of chelates.

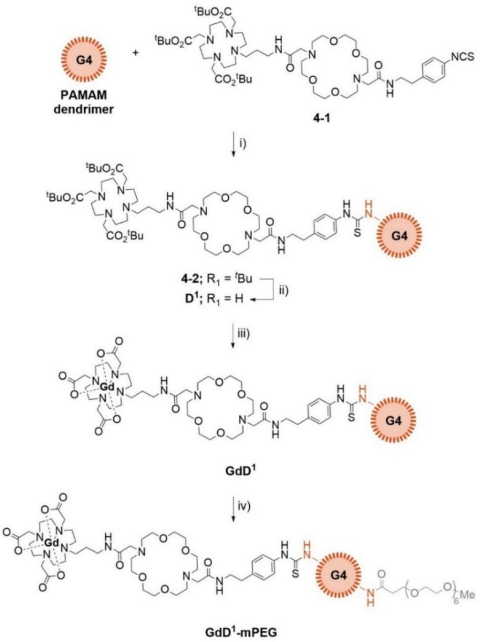

Scheme 4.2. Synthesis of the **GdD^1-mPEG**. *Reagents and conditions:* i) dry DMF, Et_3N, 45°C, 56 h, loading 56%, yield 63%; ii) HCO_2H, 60°C, quantitative yield; iii) $GdCl_3$, pH 7.2, 60°C, 65%; iv) m-PEG6-NHS ester, pH 8.0 (0.1 M HEPES), 24 h, 78%.

4.3.2 Relaxometric Properties of PAMAM-conjugates

It is known that the charged interior of PAMAM dendrimers has the ability to entrap zwitterionic guest molecules, resulting in swelling/deswelling and thus evoking the analyte concentration-dependent changes of dendrimeric properties. On the other hand, it is evidenced that the influence of surface groups governs charge-specific interactions with charged hosts.[326, 327] Therefore, to better understand the impact of intrinsic properties of PAMAM G4 constructs on relaxometric responses, we compared the initial T_1 and T_2 values and the magnitude of their changes upon interaction with Glu. The comparison was performed involving both negatively charged and non-charged surface PAMAM conjugates.

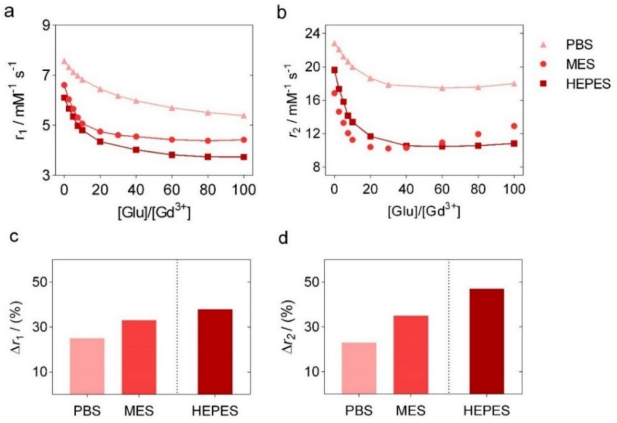

Figure 4.2. Relaxometric response of **GdD¹** and **GdD¹-mPEG** to Glu in different buffers. Bulk water proton (**a**) r_1 and (**b**) r_2 relaxometric titration of 2.5 mM **GdD¹** in 50 mM MES or PBS buffers (pH 6.4) and 2.5 mM **GdD¹-mPEG** in 50 mM HEPES (pH 7.4) with increasing amounts of Glu (0-100 equiv.) at 25ºC (300 MHz). The symbols are experimental data, and the lines represent fits calculated to *Michaelis-Menten's* model (Eq. S2.2). The data for r_2 relaxometric titration in MES is not fitted, as the applied fit is inappropriate. (**c**) and (**d**) are the corresponding relaxivity changes (in %) induced upon saturation with 60 equiv. of Glu.

The obtained r_1 and r_2 relaxometric titration responses to Glu were compared for **GdD¹**, the MR probe with a negatively charged surface, as well as for its PEGylated, charge-neutral analog **GdD¹-mPEG**. Once dissolved at physiological pH (7.4), the **GdD¹** showed a tendency to precipitate, and thus, to preserve high solubility, it was investigated at pH 6.4 in two different buffers, MES and PBS. The initial r_1 and r_2 values obtained in MES, 6.61 mM^{-1} s^{-1} and 16.85 mM^{-1} s^{-1}, respectively, were lower than in PBS, reaching the r_1 and r_2 values of 7.57 mM^{-1} s^{-1} and 22.84 mM^{-1} s^{-1}, respectively (Fig. 4.2). Upon saturation with 60 equiv. of Glu, both r_1 and r_2 in MES decreased by ~25% (Table 4.1). Similarly, the observed response in PBS was slightly stronger for both, r_1 and r_2, providing a relaxivity decrease of ~35%. The initial r_1 and r_2 values in HEPES-buffered medium (50 mM, pH 7.4) slightly exceeded 6.0 and 19.0 mM^{-1} s^{-1}, respectively. However, the changes of r_1 and r_2 to Glu were greater (37 and 48%, respectively). Such behavior in different buffers was assigned to diverse interaction with the water medium. Although the electron-donating end-amines might electrostatically attract coordinatively unsaturated Gd-core and decrease r_1 relaxivity,[328] the higher initial r_1 value for non-PEGylated conjugate is likely due to stronger interaction with water molecules, which slow down molecular tumbling and consequently result in increased initial relaxivities.[329]

The capacity of **GdD¹-mPEG** to recognize structurally different guests was estimated through the analyte-induced relaxivity decrease and binding affinity of the corresponding ternary adduct. In the first step, the water proton r_1 and r_2 relaxometric titrations were conducted in buffered HEPES-buffered medium, with i)

the amino acid NTs of interest: GABA, Glu, and Gly; ii) the ACh as an example of a non-zwitterionic transmitter and thus a non-responding analyte; and iii) the competitive metabolite HCO_3^-. The analytes were added in amounts up to 100 equiv., and the T_1 and T_2 relaxation times were measured upon each addition. The obtained data were plotted as r_1 and r_2 versus the amount of added analyte, and subsequently the K_a values were acquired from the nonlinear fitting of the r_1 (Table 4.1).

Table 4.1. Affinity constants (K_a) and change in r_1 and r_2 for **GdD[1]-mPEG** upon the addition of 60 equiv. of different analytes. [a]

Analytes	Gly	Glu	GABA	HCO_3^-	ACh
$-\Delta r_1$ (%)	34	38	40	51	2
$-\Delta r_2$ (%)	41	47	45	76	4
K_a (M^{-1})	15	40	23	30	N/A

[a] K_a-values were obtained by fitting r_1 to Eq. S2.2.

As expected, the obtained r_1 and r_2 relaxometric curves displayed downward trends, which is typical for the *q*-modulated strategy that operates *via* a turn-off mechanism (Fig. 4.3). The PEGylated conjugate displayed absolute discrimination for the non-zwitterionic ACh, while the competitor, HCO_3^-induced a decrease in r_1 of 51% upon saturation, which is greater than values observed for the NTs, ranging between 34 and 40%. The envisaged r_1/r_2 ratiometric response similar to that observed by Gunduz *et al.*[216] in the case of calcium-responsive PAMAM conjugates was not obtained (Figs. 4.4 and S4.4). In general, the observed affinities are lower than those observed in similar types of chelates non bound to NPs. This indicated greater electronic and steric hindrances in the proximity of the binding pocket, caused either by the PEG chains or the dendrimeric branches. In addition, the ditopic receptor is likely hidden in the interior of the dendrimeric branched sphere due to the greater length of PEG units, and thus, the approach of a guest molecule is to some extent obstructed. Since the binding affinities represent the free energy difference between the bound and non-bound states, it is assumed that the slightly stronger binding in the case of Glu over hydrogencarbonate occurs due to cooperative binding of ion pairs. Similar behavior was previously observed for the analogous small-molecule ditopic MRI receptors, characterized in Chapter 3, in which the nature of the remote pendant attached to the 18C6 moiety drove the affinity towards NTs. In accordance with this, the slightly disturbed host-guest association could be resolved by keeping the responsive chelate at a greater distance from the dendrimeric scaffold using a long-chain spacer.

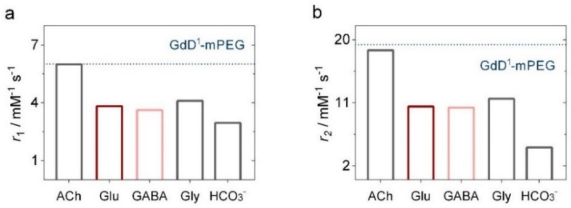

Figure 4.3. Relaxometric response of **GdD¹-mPEG$_6$** to various analytes. (**a**) Longitudinal r_1 and (**b**) transverse r_2 relaxivities of 2.5 mM **GdD¹-mPEG$_6$** in 50 mM HEPES upon addition of 60 equiv. of analytes (300 MHz) at 25ºC. Horizontal blue lines represent the corresponding initial relaxivities.

Furthermore, when compared to the relaxometric response profile of the non-bound low-molecular-weight MRI sensor introduced in Chapter 3, which is structurally identical to the surface-bound ditopic Gd-chelate, the **GdD¹-mPEG** displayed a lower initial r_1 value and weaker response to the same group of analytes. This finding suggests interaction of the oxygen atom within the mPEG chains with the MR-responsive receptor by establishing a weak Gd–O_{mPEG} interaction, which partly displaces the inner-sphere water molecule and thus decreases the initial r_1 relaxivity.[218] On the contrary, the initial r_2 value in the nanoconjugate is higher for 41% which is undoubtedly assigned to a slow molecular tumbling contribution, which is a characteristic feature of large molecules.

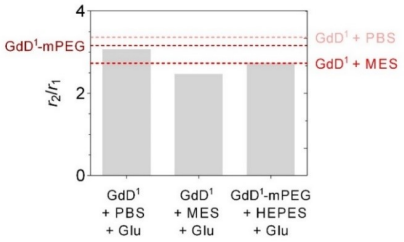

Figure 4.4. Relaxometric r_2/r_1 response of PAMAM-conjugated MRI CAs to Glu in different buffers. The calculated r_1 and r_2 values for **GdD¹** in 50 mM MES or PBS (pH 6.4) and for **GdD¹-mPEG** in 50 mM HEPES buffer (pH 7.4) at 25ºC ([Gd^{3+}] = 2.5 mM, 300 MHz). The calculated ratiometric r_2/r_1 values in the absence of analytes are depicted as horizontal dotted lines.

4.4 Conclusions

In summary, the first example of a PAMAM-conjugated MRI probe responsive to zwitterionic NTs was synthesized, and its relaxometric responses towards NTs and biologically relevant competitive metabolites were investigated. Findings gathered

in *in vitro* evaluation revealed that diversity in peripheral morphology of dendrimeric conjugates has a profound impact on initial relaxivities and efficacy to bind guest molecules. The positively charged surface of **GdD^1** exhibited slightly higher initial r_1 and r_2 relaxivities but poor solubility at physiological pH, while the surface-neutral PEGylated analogue **GdD^1-mPEG** provided excellent solubility under biologically relevant conditions and a stronger response towards analytes. In terms of selectivity, the PEGylated conjugate is ACh-insensitive, whereas the affinity towards Glu is the highest. These findings provided insights into common obstacles that could be encountered when transferring an Ln-based small-molecule sensor onto NPs. Moreover, the comparison of the responsiveness of the ditopic low-molecular-weight MRI chelate as an independent host and when incorporated into the PAMAM scaffold provided information on structure-functionality dependence. This could result in a useful guide to predict the effects of incorporating a small-sized molecular sensor into a nano-sized carrier. Overall, this work provided helpful hints to approach the design of a polytopic nano-conjugated MRI probe for sensing polycharged guests.

Chapter 5

Synthetic small-molecule receptors sensitive to amino acid neurotransmitters for ^{13}C NMR-based detection

A series of Ln-chelates involving the previously reported ligand **L^5** were synthesized. The ability of complexes **LnL^5** to modulate the chemical shift of AAs was evaluated by ^{13}C NMR titration with Glu and Gly. It was observed that the chemical shift of carboxylic carbon changed in a lanthanide-dependent manner. In addition, it was evidenced that LIS of carboxylic carbons, which bind Ln^{3+} ions, also depends on the type of guest molecule. Although the amino acids establish interactions with Ln-complexes via the Ln-$O_2{}^{13}C$ bond, placing the carboxylic carbon further away from the Ln(III)-ion, it is evidenced that shift modulation of carboxylic carbons is practically feasible. Overall, these findings set the grounds for future development of a non-invasive ^{13}C MRS/I strategy that aims at resolving spatial distribution of neurotransmitters.

5.1 Introduction

In stark contrast to MRI, which provides anatomical information where an image contrast depicts differences in density and relaxivity properties of bulk water protons within a tissue, MRS measures the concentration of different metabolites, representing a functional image that reflects metabolic activity. In this context, ^{13}C MRS is widely used to study cell neuroenergetics and Glu cycling in humans.[267, 330, 331] However, during the neuronal activation, Glu transients in the brain are spread between vesicular, synaptic, and extrasynaptic, whereas quantification of pathophysiologically relevant extracellular Glu is compromised by intracellular pools as they resonate at identical frequencies.[332] Indeed, a large discrepancy for extracellular Glu concentration of over three orders of magnitude between minimally invasive microdialysis (2–6 μM)[333, 334] and that estimated by non-invasive ^{13}C MRS (≥ 10 mM)[335-337] was reported. This is partly due to the inability of MRS to distinguish between extra- and intracellular Glu pools.

Lanthanide shift agents are commonly used to facilitate elucidation of molecular structure in solution. Although these agents are chemically inert, when placed in the vicinity of other substances, they alter ^{13}C signals *via* lanthanide-induced shift (LIS), which is predominantly contributed to by pseudo-contact shift.[338] Thus, the paramagnetic Ln-chelates could be used to differentiate overlapped signals coming from the two pools by affecting only those in the extracellular compartment. In analogy to shift agents, it is speculated that previously introduced ditopic molecular sensors responsive to AAs (Chapter 2) may be suitable for determining extracellular Glu levels. It is reasoned that paramagnetic features of lanthanide ions other than Gd^{3+} could provide a basis for capturing chemical shift modulation of nearby carboxylic carbon with ^{13}C MRS/I modality.

In this work, a study towards a hybrid approach to spatially resolve Glu pools in the brain by combining shift agents sensitive to amino acid NTs with NMR-based shift detection is described. In biological systems the labeled ^{13}C-Glu is produced in the TCA cycle when using either labelled glucose or acetate as metabolic precursors.[339] By establishing an Ln-$O_2$$^{13}C$ bond between **LnL^5** and ^{13}C-Glu, it is envisioned that carboxylic carbon signal modulation could be achieved either *via* lanthanide-induced ^{13}C-shift or PRE effect.[340-344] In either case, the extracellular Glu could be estimated from the difference upon measuring intracellular Glu, which is not affected by exogenous CAs.

5.2 Research Design

To date, the reported approaches that employ paraSHIFT agents measure change in chemical shifts of spin-active nuclei, most commonly ^{19}F, ^{1}H, and ^{31}P, incorporated within a ligand framework of a chelate.[345-347] These platforms alter the signal in response to stimuli by changing the intranuclear distance from the paramagnetic ion to the reporter group. On the contrary, Tori and Lenkinsk reported the impact of various paramagnetic reagents on nitrogen-containing chains with significant shift changes on α, β, and γ carbons, transferred through contact contribution.[348, 349]

According to Pearsons, the amino acids are hard acids and are naturally prone to establishing strong bonds with oxophilic Ln^{3+} ions.[350] In addition, Leite and co-workers evidenced that coordination of free Eu^{3+} and Tb^{3+} with L-phenylalanine (Phe) and L-tryptophan (Trp) affects chemical and magnetic properties of carboxylate and α-carbon signals.[351] In a mechanistic sense, the coordination of carboxylate oxygen to the coordinatively unsaturated Eu^{3+} strips the electron density off carboxylic carbon, whereas the α-carbons get more shielded, causing signals to shift downfield and upfield, respectively.[352, 353] However, no cases were reported on responsive paramagnetic CAs used to induce ^{13}C chemical shift of amino acid NTs. Therefore, the feasibility of this approach was questionable. Herein, a novel strategy that conveys information on the chemical shift of ^{13}C-labeled target NTs upon interaction with paramagnetic RCAs is tested. Theoretically, this approach on living subjects would involve two independent steps: implementing the administration of a ^{13}C-labelled substrate (^{13}C-glucose or ^{13}C-acetate) and monitoring their ^{13}C signal shifts of produced ^{13}C-labelled Glu. Since *in vivo* labeling of Glu is a well-established procedure, to assess the feasibility of the proposed approach, we simulated interactions of the paraSHIFT agent with the AA NTs.

The previously introduced bismacrocyclic ligand **L⁵** (Chapter 2), metalated with various Ln^{3+} ions with different paramagnetic properties, is taken as the molecular sensor. Since it is known that pseudocontact shift depends on the angle and distance between the observed spin and the paramagnetic ion, the different lanthanide complexes with common ligands are expected to have varying magnetic properties. Hence, the aim is to reveal which Ln^{3+} ion induces the largest shifts of carbons in Glu. A particular focus was set on monitoring quaternary carbons, as the binding of Glu to the receptor involves coordination of carboxylate oxygen with paramagnetic metal ions, which places carboxylic carbon in close proximity and thus greater exposure of Ln^{3+} ions.

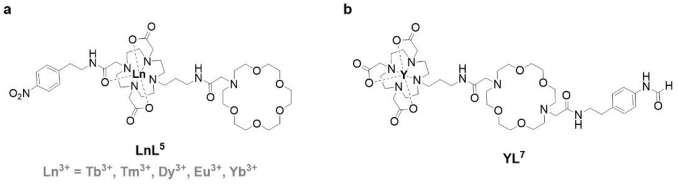

Figure 5.1. Chemical structure of paramagnetic **LnL⁵** and diamagnetic **YL⁷** chelates. (**a**) A series of paramagnetic complexes were derived from H_2do2a-derived ditopic ligand **L⁵** metalated with various lanthanides. They were synthesized according to the previously reported procedure (Scheme 2.3b, Chapter 2). (**b**) The diamagnetic chelate **YL⁷** was previously described in Chapter 3 (Scheme 3.2).

5.3 Results and Discussion

In the first step, a host-guest system involving free Eu^{3+} and Glu was studied to test the capacity of paramagnetic trivalent lanthanides to induce shift change of carboxylic carbons. Upon the addition of Glu into an aqueous Eu^{3+} solution, it was

observed that there was an unequal impact on the carboxylic carbon of carboxylates involved in binding. The C5 carbon is more strongly affected, with Δδ being ~ 5 ppm when compared to that of C1, which displayed Δδ of ~ 1 ppm. Presumably, this is caused by weaker coordination of C1-carboxylate, which is destabilized by the positively charged ammonium cation. Since those carboxylic carbons in bound Glu are close enough to the Eu^{3+} ion, experiencing a significant shift change, this experiment verified the candidacy of paramagnetic Ln-chelates as potential molecular sensors capable of modulating the chemical shift of the carboxylic ^{13}C-atom within the amino acid guest.

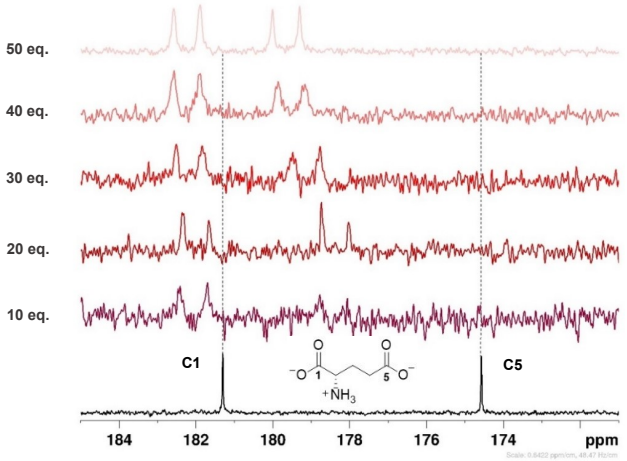

Figure 5.2. Chemical shift changes of Glu carboxylic carbons induced by Eu^{3+}. Partial ^{13}C NMR spectra displaying 40 mM Glu and 5 mM [Eu^{3+}] in the presence of 10, 20, 30, 40, and 50 equiv. of Glu-$^{13}C_5$ at 300 MHz (H_2O, pH 7.4, 25°C). To simplify comparison of Glu signals, the reference taken was the non-labelled Glu displaying two singlets, corresponding to C1 and C5 carboxylic carbons.

In the following step, the impact of various Ln^{3+} ions incorporated within ligand **L**[5] on ^{13}C NMR signals of Gly ($K_{d(Gly)}$ = 13 mM, Chapter 2) was evaluated (Fig. 5.3). The obtained results showed that different Ln^{3+} ions affect carbon resonances in a different manner, including signal intensities and changes in chemical shift. This observation is in agreement with findings demonstrating the uneven impact of various lanthanide(III) ions, incorporated within the common ligand, arising from different magnetic anisotropy effects specific for each Ln^{3+}.[354] The line broadening and loss of signals in the case of **DyL**[5] and **YbL**[5], respectively, are due to rapid relaxation of the T_2 component, which is a typical feature of lanthanides.[355] For the rest of the complexes, the trends of signal shifts towards lower magnetic fields, in the case of Gly, increased with the following order of lanthanides: $Tm^{3+} < Tb^{3+} < Eu^{3}$. That signal broadening and chemical shift change are exclusively induced by lanthanides is confirmed by measuring the impact of diamagnetic **YL**[7], with a K_d of

9.4 mM (Chapter 3), which is comparable to that of **LnL^5**, on the ^{13}C resonance of Glu (Fig. S5.2).

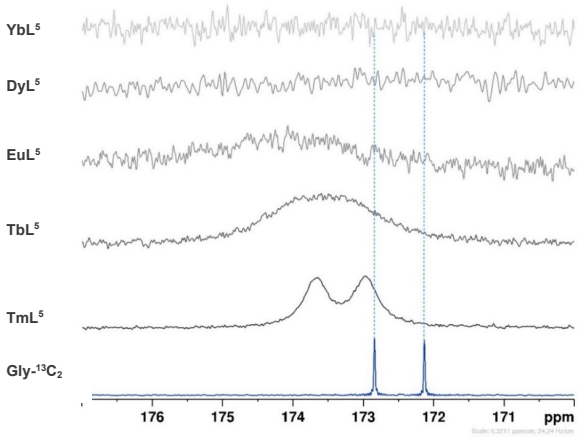

Figure 5.3. Evaluation of ^{13}C NMR shift changes of Gly induced by various **LnL^5** complexes. ^{13}C NMR cut-off spectra of a solution containing 10 mM **LnL^5** saturated with 40 equiv. of Gly at 300 MHz. (H_2O, pD 7.4, 25°C).

NMR titration of **LnL^5** with Glu led to a trend resulting in more intense peaks coming from the CH_2/CH groups and low intensity of carboxylate peaks (Fig. S5.1). This is suggestive of a more pronounced impact on carboxylic carbons as they are closer to the Eu^{3+}/Yb^{3+} ion in the ternary adduct. The choice of **EuL^5**, which worked the best in the case of Gly, is not the most effective for Glu. The ^{13}C NMR of Glu in the presence of **YbL^5** displayed a concentration-dependent signal shift with, however, only a small Δδ of approximately 0.5 ppm. This is likely due to a differently perturbed ligand field, as the binding modes are different, which is clearly indicated by the higher host affinity towards Glu (Chapter 2, Table S2.1). In addition, the observation that signals of both carboxylates are equally shifted indicated that both carboxylates bind **YbL^5**. However, lesser broadening of the C5 carboxylate suggested unequal binding strength. Moreover, the loss of multiplicity for C1 is likely due to stronger exposure to PRE of Yb^{3+} ion.

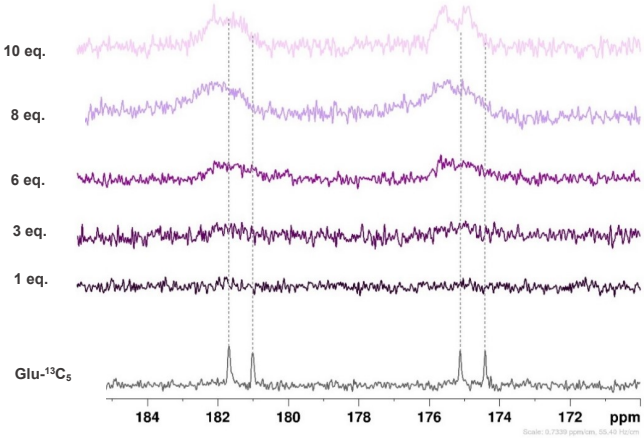

Figure 5.4. ^{13}C NMR chemical shift of Glu induced by **YbL^5**. Partial ^{13}C NMR spectra of a solution containing 10 mM **YbL^5** in the presence of 1, 3, 6, 8, and 10 equiv. Glu at 300 MHz (H_2O, pH 7.4, 25°C).

5.4 Summary and Conclusions

In this study, we investigated the suitability of paramagnetic Ln(III)-based probes, sensitive to amino acid NTs, to impact the ^{13}C chemical shift of Glu and Gly. In general, the Gly and Glu exhibited changes in signal broadening and shifts observable by NMR-based detection. Interpretation of NMR spectra evidenced that the **LnL^5** probe induces shift changes sufficient for differentiation of overlapped signals under the physiological conditions. However, in the case of more relevant Glu transmitters, the observed changes are less emphasized. Namely, the magnitudes of Δδ for the carboxylic carbon of Gly were ≥ 1 ppm (Ln = Tm^{3+}, Tb^{3+}, Eu^{3+}), whereas that of Glu gave the most obvious results for the **YbL^5** inducing Δδ of around 1 ppm. These findings supported the expectation that the ditopic Ln-chelates sensitive to AAs could be used to resolve intra- from extracellular Glu pools in the brain by means of MRS/I-based detection. Since the monitored components are neurotransmitters, this approach eliminates sensitivity issues associated with detection limits of contrast agents in the case of the classic MRI approach. Overall, this study paves the way towards the development of a hybrid imaging approach combining responsive shift reagents with ^{13}C-labeled endogenous markers and NMR-based shift detection.

Summary

This doctoral research was designed to deepen the study on paramagnetic receptors sensitive to amino acid neurotransmitters intended for application in biomedical research as molecular amplifiers for MRI visualization.

In **Chapter 1**, the responsive MRI contrast agents relationship, describing the impact of physicochemical parameters on the efficacy of contrast agents and their practical implementation to detect various stimuli, is thoroughly described. The physicochemical characteristics of PAMAM dendrimers of importance for effective design of dendrimer-conjugated MRI contrast agents were critically evaluated. In addition, concentrations and synaptic lifetimes of Glu and Gly were given, as they represent important parameters for designing molecular sensors. Moreover, the evolution of polytopic binding platforms sensitive to amino acids is summarized. At the end of the chapter, the drawbacks of existing paramagnetic complexes designed for recognition of amino acid neurotransmitters, together with limitations for practical applications, are identified.

The aim of **Chapter 2** was to thoroughly investigate the molecular structure-affinity relationship of a series of bismacrocyclic hosts with AA neurotransmitters and competitive metabolites. The molecular framework of ditopic Gd-probes inserts two orthogonal cyclen- and 18C6-derived binding sites with an on-off response to AA neurotransmitters. The implemented synthetic approach implied modification of a net charge of Gd-chelate *via* changing ligand denticity and pending arm on the 18C6 motif in terms of its size and charge. Relaxometric response to various analytes revealed that the positively charged Gd(do2a) transducer displayed higher affinities due to stronger Gd-$O_2C_{analyte}$ interactions. Complexes with sterically small benzyl or without 18C6-pendate displayed high initial relaxivities and significant decrease upon saturation with analytes. Negatively charged pendants, phosphate and acetate, yielded milder relaxivities and halved responses to analytes. Their unanticipated behavior was rationalized by intramolecular self-assembly induced by Gd-$O_{18C6\text{-}pendate}$ interaction, which impedes assembly with guest molecules. A non-charged bulky group displayed the lowest initial relaxivity, with change comparable to that of the hosts with sterically small groups. Importantly, we revealed that irrespective of Gd-chelate type, the 18C6-pending arm has a pivotal role in recognition of zwitterionic AAs.

Careful analysis of structure-activity relationships on a family of bismacrocyclic hosts (Chapter 2) allowed us to advance host framework design with more favorable complementarity towards AAs. Precisely, **Chapter 3** introduces a novel bismacrocyclic host (**GdL^7**) with an 18C6 motif engineered to boost interactions with NH_4^+. Relaxometric evaluation displayed enhanced affinity towards Glu and GABA over hydrogencarbonate. In addition, detailed analysis on the conformational mobility of the 18C6 binding site, performed on the diamagnetic binary analog (**YL^5**) and ternary adducts with HCO_3^- and Glu, revealed that greater affinity towards Glu is additionally contributed by multiple bifurcated hydrogen bonds of the ammonium cation. Yet, the co-occurrence of non-synchronized changes of T_1 and T_2 values in

response to zwitterionic AAs allowed implementation of the ratiometric r_2/r_1 approach. *In vitro* MRI phantoms measured by the bSSFP pulse sequence verified signal enhancement for Glu and GABA compared to that of hydrogencarbonate, with the r_2/r_1 ratio almost equal to that of non-bound **GdL^7**. In a broader sense, this approach offers a general strategy for designing small-molecule paramagnetic sensors for multidentate guests.

The macromolecular probe described in **Chapter 4** entails conjugation of a small-molecule Gd-chelate (Chapter 3), anchored by an isothiocyanate group to the amino surface of a G4 PAMAM dendrimer. Although a considerable increase in initial r_1 relaxivity relative to the non-conjugated receptor was expected, presumably due to interaction between coordinatively unsaturated Gd^{3+} and non-conjugated end-amines, the obtained values were lower. Capping off the remaining peripheral amines with hydrophilic PEG units improved the solubility of the dendrimeric conjugate, however, with no significant impact on relaxivity. Further analysis revealed an unanticipated relaxometric response to analytes, which is brought in connection with the interaction between oxygen from the PEG chains and the Gd-center. Yet, the host-guest study provided useful insights on orthogonality requirements for dendrimeric surface morphology with conjugated turn-off MRI-responsive sensors.

Direct visualization of synaptic Glu transients by functional MRI is challenged by the development of a highly selective molecular sensor. On the other hand, the ^{13}C MRS methodology uses Glu as an endogenous contrast agent by detecting signals coming only from Glu; however, it does not spatially resolve between different Glu pools. Thus, by combining the Gd(do2a)-based synthetic receptor **LnL^5** (Chapter 2), having among the highest affinity to Glu, with chemical shift-capturing modality, in **Chapter 5** we set the ground towards a hybrid MRS/I approach designed to distinguish extra- from intracellular Glu content. The conducted *in vitro* NMR titrations were designed to mimic the interaction of Ln(III)-chelate with ^{13}C labelled Glu in the synaptic cleft. The measurements revealed notable shift changes of carboxylic carbons of Glu, which confirmed the feasibility of this approach.

In summary, the work presented here expanded the scope of small molecules and introduced dendrimeric-conjugated MRI molecular transducers sensitive to amino acid neurotransmitters. Although the selectivity issue of zwitterionic AAs *versus* hydrogencarbonate was successfully resolved *via* the cyclen-C186 ditopic Gd-probe coined for ratiometric T_2/T_1 MRI (Chapter 3), the sensitivity requirement to achieve detection in the μM range remained unmet. Therefore, applications on animal subjects will need further structural improvements of synthetic receptors wherein target molecules will be bound *via* a large number of interactions; a promising host could be metalloenzymes or deep cavity cavitands with binding pockets engineered for the desired transmitter. Irrespective of mMRI, the introduced paradigm for the NMR-based shift imaging represents the first attempt to selectively modulate the chemical shift of ^{13}C-enriched stimuli using a responsive paramagnetic host. In addition, this approach paves the way to a wide array of endogenous markers that could be labeled through administration of ^{13}C-labeled substrates.

Appendices

6.1 Appendix A

6.2 Experimental Section

Major experiments detailed in this thesis were conducted in the Research Group MR Neuroimaging Agents at Max Planck Institute for Biological Cybernetics, Tübingen, Germany, between 2015 and 2019. Additionally, ESI HRMS measurements were conducted by Dr. Dorothee Wistuba at Eberhard Karls University in Tübingen. Computational calculations were performed by Prof. Dr. Carlos Platas-Iglesias at the University of A Coruña, Spain.

6.2.1 Materials and Methods

General procedures: Commercially available reagents and solvents were purchased from Acros, Sigma-Aldrich, Fluka, Fischer, TCI, Merck, VWR, Carl Roth, and CheMaTech and used without further purification unless stated otherwise. Solvents for the reaction were of quality puriss. p.a. Dry solvents for anhydrous reactions were dried over 3 Å molecular sieves activated *via* microwave heating or flame-dried using a heating gun and then cooled in a vacuum desiccator. For aqueous solutions, deionized water passed through a Milli-Q® filter was used. All glassware used for anhydrous reactions was heated overnight at 80°C and cooled prior to use or flame-dried under the nitrogen. Organic extracts were dried using anhydrous calcium sulphate ($CaSO_4$) unless otherwise stated. All the reactions requiring anhydrous conditions were conducted under the N_2 atmosphere. Reactions were magnetically stirred, and the progress of reactions was monitored by TLC (thin-layer chromatography) performed on alumina TLC plates pre-coated with silica gel 60 containing an UV254 fluorescent indicator visualized at 254 nm. Flash chromatography purification was performed using silica gel 60 (0.03-0.2 mm) purchased from Carl Roth, Germany. Small-scale purifications were performed on preparative thin-layer chromatographic plates (PTLC), using glass plates precoated with Analtech 500 µm thick silica gel (20 × 20 cm, Uniplate) containing a fluorescent indicator using HPLC-grade solvents. The compounds were visualized with a 254 nm UV lamp. Reverse Phase High Pressure Liquid Chromatography (RP-HPLC) was performed on a Varian PrepStar system equipped with the UV–Vis detector model 335 and a binary pump model SD-1 manual injector, controlled by Star Chromatography Workstation version 6.3 software.

General Analytical Information: Nuclear Resonance Spectra and relaxation times were measured at Bruker AVANCE III spectrometers operating at 300 or 800 MHz. All spectra were recorded at room temperature (22 – 25°C) using either $CDCl_3$ or D_2O, referenced to TMS/TSP, respectively. Processing was performed using TopSpin 2.1 and the analysis using ACD/SpecManager 9.0 (Advanced Chemistry Development, Inc.) or TopSpin 2.1 and 4.0.6. The concentrations of the analyzed solutions containing paramagnetic Ln(III) ions were determined using the bulk magnetic susceptibility shift (BMS) method.[356] The luminescence emission and lifetime measurements were performed on a QuantaMaster™ 3 PH fluorescence spectrometer from Photon Technology International, Inc. (USA). Low-resolution mass spectra (ESI-MS) were recorded on an ion trap SL 1100 Agilent system with an electrospray ionization source. High-resolution mass spectra (ESI-HRMS) were performed on a Bruker BioApex II ESI-FT-ICR, equipped with an

Agilent ESI source. Low-resolution mass spectra were recorded on an Agilent ion trap SL 1100 system with an electrospray ionization source. Relaxometric titrations

6.2.2 Relaxometric titrations

The bulk water proton, T_1 and T_2, relaxation times were measured using standard inversion-recovery (IR) and *Carr-Purcell-Meiboom-Gill* (CPMG) pulse sequences, respectively. The relaxometric titrations were performed by stepwise addition of buffered analyte to the solution of analyzed complex, and the bulk water ^{1}H relaxation times, $T_{i,obs}$, were measured after each addition. The molar r_1 and r_2 relaxivities (mM^{-1} s^{-1}) of the bulk water protons were normalized to the concentration of Gd(III) (mM) and calculated according to Eq. S2.1, where R_{obs} (s^{-1}) is the measured relaxation rate (R_{obs} = $1/T_{obs}$) and R_d is the relaxation rate of media (diamagnetic contribution).

$$r_i = \frac{(R_{obs} - R_d)}{[\mathrm{CA}]}; i = 1, 2 \qquad \text{(S2.1)}$$

6.2.3 Binding affinity calculations

The calculated r_1-values were plotted as a function of the added amount of analyte and fitted to the Michaelis-Menten model, shown by Eq. S2.2, where the slope of the fitted curve represents disassociation constant K_d, [CA] is the initial concentration of the gadolinium complex, and r_f and r_b are relaxivities of free and bound ternary adducts, respectively. To compare host-guest binding strength, the association constants (K_a) were used (K_a = $1/K_d$, in units M^{-1}).

$$y = r_f - \left(\frac{r_f - r_b}{[\mathrm{CA}]}\right) \times \left(\frac{([\mathrm{CA}] + x \times [\mathrm{CA}] + K_d) - \sqrt{([\mathrm{CA}] + x \times [\mathrm{CA}] + K_d)^2 - 4x \times [\mathrm{CA}]^2}}{2}\right) \qquad \text{(S2.2)}$$

6.2.4 Luminescence Study

The luminescence measurements were performed in H_2O and D_2O (298K, pH 7.4, 50 mM HEPES). The emission spectra were obtained by direct excitation of Eu(III) at 395 nm, while both the excitation and emission slit widths were set to 2 a nm bandpass. The decays were measured at the emission wavelength of 617 nm with a 10 µs resolution. Excitation and emission slits were set to 5 and 15 nm bandpass, respectively. Data sets are an average of 25 scans (decay data), and each reported value is the mean of three independent measurements. The obtained curves were fitted to a first-order exponential decay. The hydration number (q) was calculated using modified Horrock's model, given by Eq. S2.3;[97, 98] where n takes into account the number of exchangeable amide N–H oscillators of coordinated amide groups, k_{H_2O} and k_{D_2O} are the rate constants for depopulation of the excited state and are inversely proportional to measured excited-state lifetime (τ).

$$q = 1.2 \times \left[\left(k_{\mathrm{H_2O}} - k_{\mathrm{D_2O}}\right) - 0.25 - 0.075n\right];\ n = 1 \qquad \text{(S2.3)}$$

6.2.5 Diffusion measurements

^{1}H Diffusion-Ordered Spectroscopy (DOSY) NMR experiments were performed on a Bruker AVANCE III spectrometer using a BBO probe with z gradients. The samples were dissolved in D_2O at pD 7.8, and the data were acquired at 298 K. The viscosity calibration for the media was performed using the stebpg1s pulse sequence, and the obtained data were processed in the T_1/T_2 relaxation module (TopSpin 2.1). The diffusion measurements were conducted using the standard Bruker pulse sequence stebpg1s19, employing stimulated echo, bipolar gradients, and Watergate solvent suppression. The gradient pulse time was set to 2.5 ms with a diffusion time of 200 ms. The gradient strength was increased linearly over 16 steps from 2% to 95%. Processing was performed using Bruker Topspin software 2.1. The individual slices of pseudo-2D ^{1}H diffusion spectra were phased and base corrected, and the diffusion constants were read from the obtained spectra. The hydrodynamic radii of diffusing particles (R_h) were calculated using the Stokes-Einstein (SE) relation, which models molecules as hydrodynamic spheres, shown by Eq. S2.4, where k is the Boltzmann constant, T is the absolute temperature, η is solvent viscosity, and D is the measured diffusion coefficient.

$$R_h = \frac{kT}{6\pi\eta D} \qquad (S2.4)$$

6.2.6 Density Functional Theory (DFT) Calculations

All calculations were performed using the Gaussian 09 package (Revision E.01) within the hybrid meta-generalized gradient approximation (hybrid meta-GGA) with the TPSSh exchange-correlation functional.[357] All calculations used the large-core quasi-relativistic effective core potential (LCRECP) approximation developed by Dolg and the corresponding [5s4p3d]-GTO valence basis set for Gd,[358] whereas the ligand atoms were described by using the standard 6–31G (d,p) basis set. The stationary points found on the potential-energy surfaces as a result of geometry optimizations were confirmed to correspond to energy minima rather than saddle points by using frequency analysis. Solvent effects were included by using the integral-equation formalism variant of the polarizable continuum model (IEFPCM).[359] Relative energies include zero-point energy (ZPE) corrections obtained with frequency calculations.

6.2.7 Synthetic procedures

Tri-*tert*-butyl 2,2',2''-(10-(3-aminopropyl)-1,4,7,10-tetraazacyclododecane-1,4,7-triyl)triacetate (**2-1**)

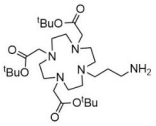

K_2CO_3 (1.69 g, 12.12 mmol) was added to a stirred solution of DO3A *tert*-butyl ester (2.4 g, 4.66 mmol) in MeCN (20 mL) at room temperature, followed by portionwise addition of *N*-(-3-bromopropyl)phthalimide (1.66 g, 6.06 mmol) over 1 h. Upon completed addition, the mixture was vigorously stirred at 60°C for 16 hours. The mixture was then filtered, and the filtrate was evaporated under reduced pressure to dryness. Thereafter, the remaining residue was redissolved in *i*-PrOH, followed by the addition of EDA (2.52 mL, 37.3 mmol). The temperature of the reaction mixture was raised to 60°C and the mixture was stirred for 4 h. The mixture was then concentrated in vacuo, and the obtained dark yellow residue was purified by column chromatography (silica gel, MeOH/CH_2Cl_2, 4:96) to afford **2-1** (1.7 g, 65%) as an off-white solid: R_f = 0.68 (MeOH/CH_2Cl_2, 15:85); **^{1}H NMR** (300 MHz, $CDCl_3$): δ (ppm) 3.43 – 3.08 (br, 8H, CH_2), 2.89 – 2.30 (br, 16H, CH_2), 1.63 (quint, 2H, CH2CH_2CH2), 1.55 – 1.39 (overlapped s, 27H, C(CH_3)$_3$); **^{13}C NMR** (75 MHz, $CDCl_3$); (ppm) 172.3, 170.7, 82.0, 81.9, 58.0, 57.2, 56.7, 50.7, 50.6, 50.5, 50.2, 50.0, 39.6, 28.0, 23.8; **LRMS (ESI-TOF)** *m/z* $[M + H]^+$ calcd. for $C_{29}H_{58}N_5O_6^+$ 572.4, found 572.4.

Tri-*tert*-butyl 2,2',2''-(10-(3-(2-bromoacetamido)propyl)-1,4,7,10-tetraazacyclododecane -1,4,7-triyl)triacetate (**2-2**)

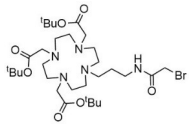

The bromide **2-2** was synthesized according to the previously published procedure.[149] The analytical data matched those previously reported.

Di-*tert*-butyl 2,2'-(4-(3-(1,3-dioxoisoindolin-2-yl)propyl)-1,4,7,10-tetraazacyclododecane-1,7-diyl)diacetate (**2-3**)

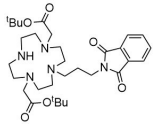

$NaHCO_3$ (0.483 g, 5.59 mmol) was added to a stirred solution of DO2A *tert*-butyl ester (2.4 g, 5.99 mmol) in MeCN (60 mL) at room temperature, followed by portionwise addition of *N*-(-3-bromopropyl)phthalimide (1.45 g, 5.39 mmol) over 4 hours. Upon completed addition, the mixture was vigorously stirred for 3 days. The mixture was then filtered, and the filtrate was evaporated under reduced pressure to dryness. The solid residue was then dissolved in CH_2Cl_2 (60 mL) and washed with water (2 x 25 mL). The organic layer was dried over anhydrous Na_2SO_4 and evaporated under vacuum. The resulting dark yellow resin was washed with a low amount of cooled Et_2O to give **2-3** (2.1 g. 62%) as an off-white solid. **^{1}H NMR** (300 MHz, $CDCl_3$)**:** δ (ppm) 7.92–7.66 (m, 4H, PhthC*H*), 3.70 (t, *J* = 7.1 Hz, 2H, CH_2NPhth), 3.33 (br s, 4H, NCH_2CO_2tBu), 3.09 (br m, 4H,

NC*H*$_2$CH$_2$N), 2.92 (br s, 4H, NHCH$_2$C*H*$_2$N), 2.81 (br s, 4H, NHC*H*$_2$CH$_2$N), 2.76–2.55 (br, 6H, CH$_2$C*H*$_2$CH$_2$ and NCH$_2$C*H*$_2$N), 1.78 (quint, 2H, CH$_2$C*H*$_2$CH$_2$), 1.45 (br s, 18H, C(C*H*$_3$)$_3$); **^{13}C NMR** (75 MHz, CDCl$_3$): δ (ppm) 170.4, 168.3, 134.2, 131.8, 123.3, 81.5, 58.1, 51.1, 50.9, 49.0, 47.7, 43.6, 36.2, 28.1, 21.1; **HRMS (ESI-TOF)** *m/z* [M + H]$^+$ calcd. for $C_{31}H_{50}N_5O_6^+$ 588.3756, found 588.3761.

Di-*tert*-butyl 2,2'-(4-(3-aminopropyl)-10-(2-((4-nitrophenethyl)amino)-2-oxoethyl)-1,4,7, 10-tetraazacyclododecane-1,7-diyl)diacetate (**2-5**)

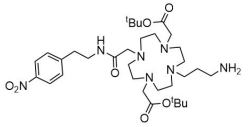

K_2CO_3 (1.2 g, 8.58 mmol) was added to a solution of **2-3** (2.1 g, 2.65 mmol) in dry MeCN and the mixture was stirred for 30 min. at room temperature. The compound **2-4** (1.24 g, 4.29 mmol) was then added portion-wise, the temperature was elevated to 45°C and it was left to stir for 16 hours. Thereafter, the reaction mixture was cooled down to r.t., solvent was removed under the vacuum, and the residue was redissolved in *i*-PrOH, followed by the addition of EDA (1.43 mL, 21.6 mmol). The temperature of the reaction mixture was raised to 60°C and the mixture was stirred for 4 h. Then the mixture was concentrated in vacuo, and the obtained dark yellow residue was purified by column chromatography (silica gel, MeOH/CH_2Cl_2, 5:95) to give **2-5** (1.2 g, 65%) as an off-white solid: R_f = 0.31 (MeOH/CH_2Cl_2, 10:90); **^{1}H NMR** (300 MHz, $CDCl_3$); (ppm) 8.11 (d, *J* = 7.55 Hz, 2H, ArH), 7.58 (d, *J* = 7.93 Hz, 2H, ArH), 3.71–1.94 (br, 30H, C*H*$_2$), 1.84–1.35 (overlapped s, 20H, CH$_2$C*H*$_2$CH$_2$ and C(C*H*$_3$)$_3$); **^{13}C NMR** (75 MHz, $CDCl_3$); (ppm) 172.0, 170.2, 147.9, 146.4, 130.2, 123.4, 82.0, 58.7, 56.6, 56.4, 56.3, 50.6, 50.2, 49.5, 40.0, 38.8, 34.8, 28.0, 23.8; **HRMS (ESI-TOF)** *m/z* [M + H]$^+$ calcd. for $C_{33}H_{58}N_7O_7^+$ 664.4392, found 664.4398.

Di-*tert*-butyl 2,2'-(4-(3-(2-bromoacetamido)propyl)-10-(2-((4-nitrophenethyl)amino)-2-oxoethyl)-1,4,7,10-tetraazacyclododecane-1,7-diyl)diacetate (**2-6**)

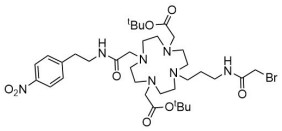

Bromoacetic acid (0.404 g, 2.82 mmol) and DCC (0.587 g, 2.82 mmol) were subsequently added as solids to a stirred solution of the amine **2-3** (1.1 g, 1.66 mmol) in CH_2Cl_2 (30 mL), and the reaction mixture was stirred at room temperature for 8 h. Then, the precipitate was filtered off, and the filtrate was concentrated under reduced pressure. The crude residue was purified by column chromatography (silica gel, MeOH/CH_2Cl_2 gradient from 5:95 to 30:70) to yield **2-6** (840 mg, 52%) as an off-white solid: R_f = 0.5 (MeOH/CH_2Cl_2, 15:85); **^{1}H NMR** (300 MHz, $CDCl_3$); (ppm) 8.62 (m, 1H, *H*NCO), 8.10 (d, *J* = 8.69 Hz, 2H,

ArH), 7.67 (m, 1H, *H*NCO), 7.48 (d, *J* = 8.69 Hz, 2 H), 3.95 (br s, 2H, C*H*$_2$Br), 3.65–2.07 (br, 30H, C*H*$_2$), 1.74 (quint, 2H, CH$_2$C*H*$_2$CH$_2$), 1.48 (br s, 18 H, C(C*H*$_3$)$_3$); **^{13}C NMR** (75 MHz, CDCl$_3$); (ppm) 172.8, 171.1, 166.3, 147.9, 146.4, 130.0, 123.4, 82.7, 56.7, 56.3, 53.5, 51.6, 51.1, 50.9, 50.1, 39.7, 38.3, 35.3, 29.5, 28.0, 25.2; **HRMS (ESI-TOF)** *m/z* [M + H]$^+$ calcd. for $C_{35}H_{59}BrN_7O_8^+$ 784.3603, found 784.3596.

tert-butyl 2-(1,4,10,13-tetraoxa-7,16-diazacyclooctadecan-7-yl)acetate (**2-7**)

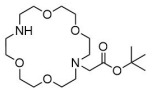

The solution of *tert*-butyl bromoacetate (0.32 mL, 2.13 mmol) in CDCl$_3$ (25 mL) was added dropwise to a stirred mixture of 4,13-diaza-18-crown 6-ether (0.59 g, 2.24 mmol) and Et$_3$N (0.32 mL, 2.24 mmol) in CDCl$_3$ (25 mL) over 8 h, and the resulting mixture was stirred at room temperature for 2 days. Then the reaction mixture was evaporated under the vacuum, and the residue was purified by column chromatography (silica gel, 3.5% MeOH/CH$_2$Cl$_2$) to give **2-7** (0.52 g, 62%) as a pale yellow solid: R$_f$ = 0.23 (MeOH/CH$_2$Cl$_2$, 15:85); **^{1}H NMR** (300 MHz, CDCl$_3$): δ (ppm) 4.03–3.81 (m, 4H, HNCH$_2$C*H*$_2$O), 3.71–3.47 (overlapped m, 12H, OC*H*$_2$CH$_2$N and OC*H*$_2$C*H*$_2$O), 3.42–3.33 (overlapped s, 2H, NC*H*$_2$C(O)O), 3.21–3.06 (br m, 4 H, NC*H*$_2$CH$_2$O), 3.03–2.90 (m, 4 H, OCH$_2$C*H*$_2$N), 1.49–1.41 (overlapped s, 9 H, C(C*H*$_3$)$_3$); **^{13}C NMR** (75 MHz, CDCl$_3$): δ (ppm) 170.4, 81.4, 70.2, 69.9, 67.8, 66.5, 53.9, 50.8, 48.7, 28.3; **HRMS (ESI-TOF)** *m/z* [M + H]$^+$ calcd. for $C_{18}H_{37}N_2O_6^+$ 377.2646, found 377.2651.

7-Benzyl-1,4,10,13-tetraoxa-7,16-diazacyclooctadecane (**2-8**)

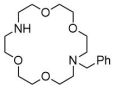

Et$_3$N (0.32 mL, 4.48 mmol) was added to a stirred solution of 4,13-diaza-18-crown 6-ether (1.0 g, 3.74 mmol) in CDCl$_3$ (25 mL) and the mixture was stirred for 30 min. Benzyl chloride (0.43 mL, 3.74 mmol) in CDCl$_3$ (25 mL) was then added dropwise over 8 h and the resulting mixture was stirred at room temperature for 2 days. Then the solvent was removed under reduced pressure, and the solid residue was purified by column chromatography (silica gel, 5% MeOH/CH$_2$Cl$_2$) to give compound **2-8** (0.79 g, 60%) as an off-white solid: R$_f$ = 0.16 (MeOH/CH$_2$Cl$_2$, 15:85); **^{1}H NMR** (300 MHz, CDCl$_3$): δ (ppm) 7.40–7.19 (overlapped m, 5H, Ar*H*), 3.88 (t, 4H, NHCH$_2$C*H*$_2$O), 3.68 (br s, 2 H, C*H*$_2$Ph), 3.66–3.43 (overlapped m, 12H, OC*H*$_2$), 3.17 (t, 4H, NHC*H*$_2$CH$_2$), 2.77 (t, *J* = 4.91 Hz, 4H, NC*H*$_2$CH$_2$); **^{13}C NMR** (75 MHz, CDCl$_3$): δ (ppm) 138.5, 128.9, 128.2, 126.9, 70.0, 69.9, 68.6, 66.5, 57.8, 55.1, 48.4; **HRMS (ESI-TOF)** *m/z* [M + H]$^+$ calcd. for $C_{19}H_{33}N_2O_4^+$ 353.2435, found 353.2438.

Diethyl ((16-benzyl-1,4,10,13-tetraoxa-7,16-diazacyclooctadecan-7-yl)methyl)phosphonate (**2-9**)

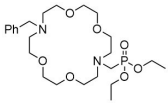

Formaldehyde (48 mg, 1.59 mmol) and anhydrous Na_2SO_4 (250 mg) were added to a solution of diethyl phosphonate (218 µL, 1.59 mmol) in dry CH_3Cl (15 mL), and the resulting mixture was stirred for 30 min. at room temperature. Then the compound **2-8** (350 mg, 0.99 mmol) was added, followed by the addition of $BF_3{\cdot}Et_2O$ (10 µL), and the reaction mixture was refluxed for 6 h. The reaction mixture was then cooled down to r.t., filtered off, and the filtrate was concentrated in vacuo, and the obtained solid residue was purified by column chromatography (silica gel, $MeOH/CH_2Cl_2$ gradient from 4:96 to 8:92) to afford product **2-9** (298 mg, 60%) as a dark yellow solid: R_f = 0.42 ($MeOH/CH_2Cl_2$, 20:80); **^{1}H NMR** (300 MHz, $CDCl_3$): δ (ppm) 7.52–7.14 (overlapped m, 5H, ArH), 4.13 (quint, 4H, C*H*$_2$CH$_3$), 3.80 (br s, 2H, NC*H*$_2$Ph), 3.74–3.49 (overlapped m, 16H, OC*H*$_2$CH$_2$), 3.17–2.50 (overlapped m, 10H, CH$_2$C*H*$_2$N and NC*H*$_2$P(O), 1.34 (t, *J* = 7.08 Hz, 6H, CH$_3$); **^{13}C NMR** (75 MHz, $CDCl_3$): δ (ppm) 139.2, 129.3, 128.3, 127.3, 70.6, 69.9, 69.3, 69.3, 61.9, 61.8, 59.6, 55.3, 55.2, 53.5, 51.9, 49.8, 16.6, 16.5; **^{31}P NMR** (121.5 MHz, $CDCl_3$): δ (ppm) 25.46; **HRMS (ESI-TOF)** *m/z* [M + Na]$^+$ calcd. for $C_{24}H_{43}N_2NaO_7P^+$ 525.2700, found 525.2707.

Diethyl ((1,4,10,13-tetraoxa-7,16-diazacyclooctadecan-7-yl)methyl)phosphonate (**2-10**)

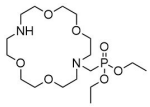

The catalyst $Pd(OH)_2/C$ (20% w/w) was suspended in the solution of **2-9** (298 mg, 0.59 mmol) in EtOH (25 mL), and a catalytic amount of NH_4OH (50 µL, 7N solution in MeOH) was then added. The suspension was shaken in Parr's hydrogenator for 7 h, filtered off through a diatomaceous earth pad, and the filtrate was evaporated to yield **2-10** (230 mg, 94%) as a dark yellow-brown semi-solid. R_f = 0.19 ($MeOH/CH_2Cl_2$, 20:80); **^{1}H NMR** (300 MHz, $CDCl_3$): δ (ppm) 4.25–4.04 (m, 4H, OC*H*$_2$CH$_3$), 3.82–3.50 (overlapped m, 16H, OC*H*$_2$C*H2*O and OC*H*$_2$CH$_2$N), 3.17–3.04 (overlapped s, 2H, NC*H*$_2$P), 3.04–2.71 (overlapped m, 8H OCH$_2$C*H*$_2$N), 1.33 (t, *J* = 6.99 Hz, 6H, CH$_3$); **^{13}C NMR** (75 MHz, $CDCl_3$): δ (ppm) 70.4, 70.1, 69.3, 69.0, 61.9, 61.8, 55.0, 54.9, 50.2, 48.9, 48.2, 16.6, 16.5; **^{31}P NMR** (121 MHz, $CDCl_3$): δ (ppm) 25.82; **HRMS (ESI-TOF)** *m/z* [M + Na]$^+$ calcd. for $C_{17}H_{37}N_2NaO_7P^+$ 435.2231, found 435.2235.

4-((1,4,10,13-tetraoxa-7,16-diazacyclooctadecan-7-yl)methyl)-7-methoxy-2H-chromen-2-one (**2-11**)

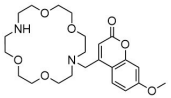

4-Bromomethyl-7-methoxycoumarin (382 mg, 1.42 mmol) was added to a stirred mixture of 4,13-diaza-18-crown 6-ether (392 g, 1.49 mmol) and $NaHCO_3$ (126 mg, 1.49 mmol) in MeCN (25 mL), and the resulting mixture was stirred at r.t. for 2 days. Then the reaction mixture was evaporated under the vacuum, and the residue was purified by column chromatography (silica gel, 3.5% MeOH/CH_2Cl_2) to yield **11** (0.269 g, 40%) as a yellowish sold: R_f = 0.39 (MeOH/CH_2Cl_2, 15:85); **^{1}H NMR** (300 MHz, $CDCl_3$): δ (ppm); 7.51 (d, *J* = 8.69 Hz, 1H, CC*H*C=HCC), 6.97–6.61 (overlapped m, 3H, ArC*H*), 3.86–3.77 (overlapped m, 7H, $NHCH_2CH_2O$ and OCH_3), 3.67 (br s, 2H, NCH_2C), 3.59 – 3.51 (overlapped m, 4H, OCH_2CH_2O), 3.47–3.35 (overlapped m, 8H, OCH_2CH_2O and OCH_2CH_2N), 3.33–3.19 (br s, 4H, $NHCH_2CH_2O$), 2.83 (t, *J* = 8.50 Hz, OCH_2CH_2N); **^{13}C NMR** (75 MHz, $CDCl_3$): δ (ppm) 161.5, 160.8, 154.3, 153.0, 123.5, 111.3, 110.5, 100.1, 69.2, 68.8, 67.8, 65.4, 56.8, 54.8, 53.4, 47.1; **HRMS (ESI-TOF)** *m/z* $[M + H]^+$ calcd. for $C_{23}H_{35}N_2O_7^+$ 451.2439, found 451.2443.

General procedure for the preparation (**2-12 to 2-17**)

To a stirred solution of the corresponding 1,10-diaza 18-crown-6 ether derivative (**2-7**, **2-8**, **2-10**, **2-11)** or 1-aza-18-crown-6 ether in dry DMF, the base $NaHCO_3$ (3.2 equiv.) was added, and the mixture was stirred for 45 min. To a stirred mixture, the corresponding bromide (**2-2** or **2-6**) was added at once, and the reaction was stirred under the nitrogen atmosphere for three days (in the case of compound **2-15**, for five days). The reaction mixture was then filtered off, and solvent was evaporated on a Kugelrohr apparatus to give residue, which was purified on PTLC plates to yield the corresponding *bis*-macrocycle (**2-12** to **2-17**).

Tri-*tert*-butyl 2,2',2''-(10-(3-(2-(16-benzyl-1,4,10,13-tetraoxa-7,16-diazacyclooctadecan-7-yl)acetamido)propyl)-1,4,7,10-tetraazacyclododecane-1,4,7-triyl)triacetate (**2-12**)

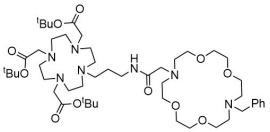

Yield: dark yellow solid (199 mg, 0.149 mmol, 72%): R_f = 0.59 (CH_2Cl_2/MeOH, 85:15); **^{1}H NMR** (300 MHz, $CDCl_3$): δ (ppm) 7.47–7.11 (overlapped m, 5H, Ar*H*), 4.13–1.98 (br, 54H, CH_2), 1.79 (br s, 2H, $CH_2CH_2CH_2$), 1.70–1.33 (overlapped s, 27H, $C(CH_3)_3$); **^{13}C NMR** (75 MHz, $CDCl_3$): δ (ppm): 173.5, 172.6, 172.3, 136.4, 130.4, 128.4, 127.7, 82.6, 82.4, 69.0, 68.3, 67.4, 66.9, 60.2, 57.9, 56.5, 55.8, 55.6, 53.5, 53.4, 52.2, 51.9, 50.9, 50.0, 37.7, 27.9,

27.8, 24.7; **HRMS** (ESI-TOF) *m/z* $[M + Na]^+$ calcd. for $C_{50}H_{89}N_7NaO_{11}^+$ 986.6512, found 986.6507.

Di-*tert*-butyl 2,2'-(4-(3-(2-(16-benzyl-1,4,10,13-tetraoxa-7,16-diazacyclooctadecan-7-yl)-acetamido)propyl)-10-(2-((4-nitrophenethyl)amino)-2-oxoethyl)-1,4,7,10-tetraazacyclod-odecane-1,7-diyl)diacetate (**2-13**)

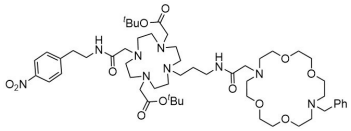

Yield: dark yellow solid (94.7 mg, 79%); R_f = 0.56 (CH_2Cl_2/MeOH, 85:15); **^{1}H NMR** (300 MHz, $CDCl_3$): δ (ppm) 8.00 (d, *J* = 8.31, 2H, Ar*H*), 7.42 (d, *J* = 8.12, 2H, Ar*H*), 7.35–6.89 (br s, 5H, Ar*H*), 3.89–1.84 (br, 58H, CH_2), 1.70 (br s, 2H, $CH_2CH_2CH_2$), 1.50–1.23 (overlapped s, 18H, C(CH_3)$_3$); **^{13}C NMR** (75 MHz, $CDCl_3$): δ (ppm) 172.8, 172.6, 171.1, 148.1, 146.3, 136.3 130.3, 130.0, 128.4, 127.8, 123.3, 82.3, 69.8, 68.8, 68.2, 67.4, 66.8, 60.3, 57.9, 57.8, 56.6, 56.2, 53.4, 52.3, 51.7, 50.2, 50.0, 48.3, 39.6, 37. 9, 35.3, 27.9, 24.3; **HRMS (ESI-TOF)** *m/z* $[M + Na]^+$ calcd. for $C_{54}H_{89}N_9NaO_{12}^+$ 1078.6523, found 1078.6520.

Di-*tert*-butyl 2,2'-(4-(3-(2-(16-(2-(tert-butoxy)-2-oxoethyl)-1,4,10,13-tetraoxa-7,16-diazac ycloоctadecan-7-yl)acetamido)propyl)-10-(2-((4-nitrophenethyl)amino)-2-oxoethyl)-1,4, 7,10-tetraazacyclododecane-1,7-diyl)diacetate (**2-14**)

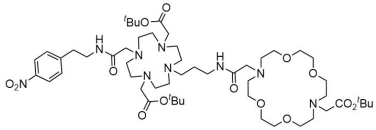

Yield: dark yellow solid (140 mg, 61%); **^{1}H NMR** (300 MHz, $CDCl_3$): δ (ppm) 8.02 (d, *J* = 8.31 Hz, 2H, Ar*H*), 7.43 (d, *J* = 7.74 Hz, 2H, Ar*H*), 4.34–1.52 (br, 58H, CH_2), 1.51–1.26 (overlapped s, 27H, C(CH_3)$_3$); **^{13}C NMR** (75 MHz, $CDCl_3$): δ (ppm) 171.9, 171.3, 170.6, 170.2, 147.1, 145.4, 129.1, 122.4, 81.7, 81.4, 67.9, 67.6, 66.2, 66.0, 60.9, 58.6, 57.5, 55.8, 55.3, 53.9, 53.3, 50.9, 50.8, 49.9, 49.2, 38.7, 36.6, 34.3, 27.2, 27.2, 27.1, 24.8; **HRMS (ESI-TOF):** *m/z* $[M + Na]^+$ calcd. for $C_{53}H_{93}N_9NaO_{14}^+$ 1102.6734, found 1102.6729.

Di-*tert*-butyl 2,2'-(4-(3-(2-(16-((diethoxyphosphoryl)methyl)-1,4,10,13-tetraoxa-7,16-dia-zacyclooctadecan-7-yl)acetamido)propyl)-10-(2-((4-nitrophenethyl)amino)-2-oxoeth-yl)-1,4,7,10-tetraazacyclododecane-1,7-diyl)diacetate (**2-15**)

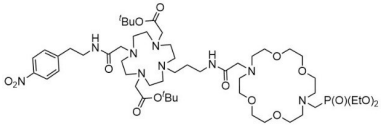

Yield: dark yellow solid (70 mg, 25%); **^{1}H NMR** (300 MHz, $CDCl_3$): δ (ppm) 8.03 (d, *J* = 8.02 Hz, 2H, Ar*H*), 7.43 (d, *J* = 7.44 Hz, 2H, Ar*H*), 4.00 (quint, 4H, C*H*$_2$CH$_3$), 3.85–1.91 (br, 58H, C*H*$_2$), 1.78 (br s, 2H, CH$_2$*CH*$_2$CH$_2$), 1.50–1.32 (overlapped s, 18H, C(*CH*$_3$)$_3$), 1.25 (t, 6H, CH$_2$*CH*$_3$); **^{13}C NMR** (75 MHz, $CDCl_3$): δ (ppm); 173.5, 172.6, 172.3, 136.4, 130.4, 128.4, 127.7, 82.6, 82.4, 69.0, 68.3, 67.4, 66.9, 60.2, 57.9, 56.5, 55.8, 55.6, 53.5, 53.4, 52.2, 51.9, 50.9, 50.0, 37.7, 32.0, 31.9, 29.6, 27.9, 27.8, 24.7; **^{31}P NMR** (121.5 MHz, $CDCl_3$): δ (ppm) 26.50, 26.81, 27.31; **HRMS (ESI-TOF):** *m/z* $[M + Na]^+$ calcd. for $C_{52}H_{94}N_9NaO_{15}P^+$ 1138.6499, found 1138.6491.

Di-*tert*-butyl 2,2'-(4-(3-(2-(1,4,7,10,13-pentaoxa-16-azacyclooctadecan-16-yl)acetamido) propyl)-10-(2-((4-nitrophenethyl)amino)-2-oxoethyl)-1,4,7,10-tetraazacyclododecane-1,7-diyl)diacetate (**2-16**)

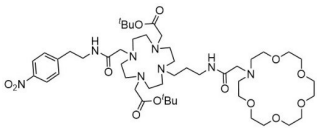

Yield: white solid (72%). **^{1}H NMR** (300 MHz, $CDCl_3$): δ (ppm) 8.10–7.98 (m, 2H, Ar*H*), 7.59–7.32 (m, 2H, Ar*H*), 3.92–1.91 (br, 58H, C*H*$_2$), 1.77 (broad s, 2H, CH$_2$*CH*$_2$CH$_2$), 1.52–1.28 (overlapped s, 18H, C(*CH*$_3$)$_3$); **^{13}C NMR** (75 MHz, $CDCl_3$): δ (ppm) 172.9, 172.5, 171.2, 148.2, 146.4, 130.1, 123.3, 82.3, 81.7, 68.9, 66.6, 68.5, 68.1, 67.1, 58.2, 56.3, 54.4, 54.1, 53.5, 51.8, 50.3, 50.0, 48.9, 39.6, 37.9, 35.3, 28.0, 24.1; **HRMS (ESI-TOF):** *m/z* $[M + Na]^+$ calcd. for $C_{47}H_{82}N_8NaO_{13}^+$ 989.5894, found 989.5887.

Di-*tert*-butyl 2,2'-(4-(3-(2-(16-((7-methoxy-2-oxo-2H-chromen-4-yl)methyl)-1,4,10,13-tetraoxa-7,16-diazacyclooctadecan-7-yl)acetamido)propyl)-10-(2-((4-nitrophenethyl) amino)-2-oxoethyl)-1,4,7,10-tetraazacyclododecane-1,7-diyl)diacetate (**2-17**)

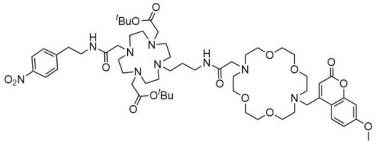

Yield: white solid (80 mg, 26%). **^{1}H NMR** (300 MHz, $CDCl_3$): δ (ppm) 8.19–7.87 (m, 2H, Ar*H*), 7.62 (dd, *J* = 59.0, 8.78 Hz, 1H, Ar*H*), 7.48–7.33 (m, 2H, Ar*H*), 7.03–6.59 (overlapped m, 2H, Ar*H*), 6.44 (d, *J* = 25.12 Hz, 1H, C=C*H*CO$_2$C), 4.07–2.00 (br, 61H, CH$_2$ and CH$_3$), 1.83–1.60 (br, CH$_2$C*H*$_2$CH$_2$), 1.51–1.26 (overlapped s, 18H, C(*CH*$_3$)$_3$); **^{13}C NMR** (75 MHz, $CDCl_3$): δ (ppm); 171.4, 170.2, 168.9, 161.7, 161.5, 160.2, 154.3, 151.9, 147.2, 146.6, 145.5, 129.0, 123.8, 122.5, 111.9, 111.5, 110.2, 100.1, 80.8, 67.9, 67.9, 67.1, 66.1, 57.8, 57.1, 55.3, 55.0, 53.6, 53.4, 53.0, 52.4, 50.7, 50.2, 49.4, 48.4, 46.0, 38.6, 36.9, 34.3, 28.7, 27.2, 27.0, 22.4; **HRMS (ESI-TOF):** *m/z* $[M + Na]^+$ calcd. for $C_{58}H_{91}N_9NaO_{15}^+$ 1176.6527, found 1176.6523.

General procedure for hydrolysis **2-12** to **2-17**

The compound **2-12, 2-13, 2-14**, **2-16**, or **2-17** was dissolved in formic acid (8 mL) and stirred at 60°C for 24 hours. After the cleavage of *tert*-butyl esters was completed (confirmed by the low-resolution MS analysis), the reaction mixture was cooled down to r.t., and the solvent was evaporated under reduced pressure, followed by lyophilization for two days to yield the corresponding final ligand **L$^{1-3,5,6}$**. The products were analyzed by CHN analysis, and the amount of ligand was calculated with respect to the content of nitrogen for the subsequent complexation with Ln(III).

2,2',2''-(10-(3-(2-(16-benzyl-1,4,10,13-tetraoxa-7,16-diazacyclooctadecan-7-yl)acetamideo)propyl)-1,4,7,10-tetraazacyclododecane-1,4,7-triyl)triacetic acid (**L^1**)

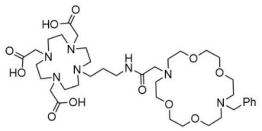

Yield: off-white solid (75%). **^{1}H NMR** (300 MHz, D_2O): δ (ppm) 7.50 (br s, 5H, Ar*H*), 4.48 (br s, 2H, C*H*$_2$Ph), 4.16 (br s, 2H, C*H*$_2$C(O)NH), 4.00–2.52 (br, 50H, C*H*$_2$), 1.76 (br s, 2H, CH$_2$C*H*$_2$CH$_2$); **^{13}C NMR** (75 MHz, D_2O): δ (ppm): 171.7, 171.1, 164.0, 130.5, 129.5, 128.5, 127.6, 69.0, 68.8, 63.0, 62.5, 57.7, 54.3, 53.7, 53.5, 52.1, 51.9, 50.0, 49.0, 48.6, 48.2, 36.3, 23.3; **HRMS (ESI-TOF)** *m/z* $[M + 2H]^{2+}$ calcd. for $C_{38}H_{67}N_7O_{11}^{2+}$ 398.7444, found 398.7448.

2,2'-(4-(3-(2-(16-benzyl-1,4,10,13-tetraoxa-7,16-diazacyclooctadecan-7-yl)acetamido)pr-opyl)-10-(2-((4-nitrophenethyl)amino)-2-oxoethyl)-1,4,7,10-tetraazacyclododecane-1,7-diyl)diacetic acid (**L^2**)

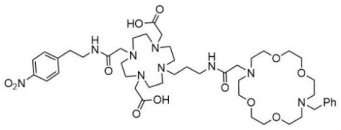

Yield: off-white solid (72%). **^{1}H NMR** (300 MHz, D_2O): δ (ppm) 8.02 (d, *J* = 8.50 Hz, 2H, Ar*H*), 7.46–7.23 (overlapped m, 5H, Ar*H*), 4.35 (br s, 2H, C*H*$_2$CONH(CH$_2$)$_2$), 4.03 (br s, 2H, C*H*$_2$CONH(CH$_2$)$_3$), 3.82–2.71 (overlapped m, 52H, C*H*$_2$), 2.62 (br s, 2H, C*H*$_2$(CH$_2$)$_2$NHCO), 1.63 (quint, 2H, CH$_2$C*H*$_2$CH$_2$); **^{13}C NMR** (75 MHz, D_2O): δ (ppm) 171.2, 169.0, 164.8, 147.9, 147.3, 146.3, 131.4, 130.4, 130.1, 129.4, 123.6, 69.9, 69.7, 63.9, 63.4, 58.6, 56.7, 56.4, 55.8, 54.6, 54.4, 53.0, 50.6, 50.1, 49.1, 48.5, 39.7, 37.4, 34.7, 24.5; **HRMS (ESI-TOF)** *m/z* $[M + 2H]^{2+}$ calcd. for $C_{46}H_{75}N_9O_{12}^{2+}$ 472.7762, found 472.7771.

2,2'-(4-(3-(2-(16-(carboxymethyl)-1,4,10,13-tetraoxa-7,16-diazacyclooctadecan-7-yl)acet amido)propyl)-10-(2-((4-nitrophenethyl)amino)-2-oxoethyl)-1,4,7,10-tetraazacyclododec ane-1,7-diyl)diacetic acid (**L^3**)

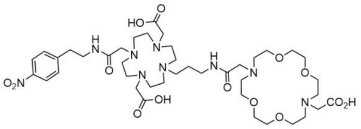

Yield: off-white solid (82%). **^{1}H NMR** (300 MHz, D_2O): δ (ppm) 8.02 (d, *J* = 8.12 Hz, 2H, Ar*H*), 7.34 (d, *J* = 7.93 Hz, 2H, Ar*H*), 4.01–1.99 (overlapped m, 58H, CH_2), 1.57 (br s, 2H, $CH_2CH_2CH_2$); **^{13}C NMR** (75 MHz, D_2O): δ (ppm) 169.9, 168.7, 168.4, 168.3, 146.6, 145.0, 128.8, 122.3, 68.6, 68.3, 65.8, 62.5, 55.6, 53.8, 53.5, 53.0, 50.1, 49.8, 48.7, 48.6. 46.6, 46.5, 46.3; 38.2, 36.0, 33.4, 23.2; **HRMS (ESI-TOF):** *m/z* $[M + 2H]^{2+}$ calcd. for $C_{41}H_{71}N_9O_{14}^{2+}$ 456.77621, found 456.7755.

2,2'-(4-(2-((4-nitrophenethyl)amino)-2-oxoethyl)-10-(3-(2-(16-(phosphonomethyl)-1,4,10,13-tetraoxa-7,16-diazacyclooctadecan-7-yl)acetamido)propyl)-1,4,7,10-tetraazacyclodo-decane-1,7-diyl)diacetic acid (**L^4**)

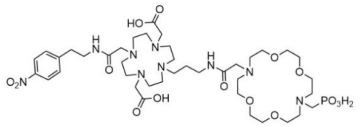

The compound **15** (70 mg, 63 mmol) was dissolved in dry CH_2Cl_2 (5 mL) in a flame-dried flask, and the solution was cooled down to 0°C under the nitrogen atmosphere. Then the $BrSiMe_3$ (196 mg, 1.254 mmol) was added slowly, and the reaction was stirred for 2 h at r.t. to result in the formation of a white precipitate. The solvent was then evaporated under the reduced pressure; without previous isolation H_2O (3 mL) was added into the solid residue, and the mixture was stirred for 1.5 h. The reaction mixture was then evaporated and lyophilized to give a glassy amorphous solid (32 mg, 54%). **^{1}H NMR** (300 MHz, D_2O): δ (ppm) 8.04 (d, *J* = 8.50, 2H, Ar*H*), 7.36 (d, *J* = 8.31, 2H, Ar*H*), 4.07 (br s, 2H, CH_2CONH$(CH_2)_2$), 3.97 (br s, 2H, CH_2CONH$(CH_2)_3$), 3.84–2.78 (br, 54H, CH_2), 1.91 (quint. 2H, $CH_2CH_2CH_2$); **^{13}C NMR** (75 MHz, D_2O): δ (ppm) 174.0, 165.2, 164.5, 147.8, 146.3, 130.2, 123.7, 69.9, 63.8, 59.8, 57.5, 55.3, 55.2, 54.7, 54.7, 54.6, 53.0, 52.2, 51.9, 51.8, 50.1, 50.1, 48.2, 48.2, 40.2, 36.9, 34.9, 22.9; **^{31}P NMR** (121.5 MHz, D_2O): δ (ppm) 6.63, 9.00; **HRMS (ESI-TOF)** *m/z* $[M + Ca]^{2+}$ calcd. for $C_{40}H_{70}CaN_9O_{15}P^{2+}$ 493.7172, found 493.7167.

2,2'-(4-(3-(2-(1,4,7,10,13-pentaoxa-16-azacyclooctadecan-16-yl)acetamido)propyl)-10-(2-((4-nitrophenethyl)amino)-2-oxoethyl)-1,4,7,10-tetraazacyclododecane-1,7-diyl)diacetic acid (**L^5**)

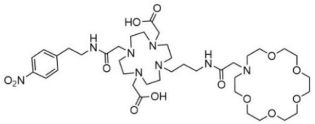

Yield: off-white solid (72%); **^{1}H NMR** (300 MHz, D_2O): δ (ppm) 8.14 (d, *J* = 8.12 Hz, 2H, Ar*H*), 7.45 (d, *J* = 7.74 Hz, 2H, Ar*H*), 4.05 (br s, 2H, CH_2CONH), 3.93–2.75 (overlapped m, 52H, CH_2), 2.67 (br s, 2H, CH_2(CH$_2$)$_2$NHCO), 1.73 (quint, 2H, CH$_2$CH_2CH$_2$); **^{13}C NMR** (75 MHz, D_2O): δ (ppm) 170.6, 165.1, 164.9, 147.9, 146.3, 130.1, 123.7, 69.9, 69.7, 69.5, 65.9, 63.8, 56.3, 55.1, 54.6, 51.4, 51.0, 50.6, 50.3, 48.7, 48.3, 47.9, 39.7, 37.3, 34.7, 24.5; **HRMS (ESI-TOF):** *m/z* [M + 2H]$^{2+}$ calcd. for $C_{39}H_{68}N_8O_{13}^{2+}$ 428.2447, found 428.2450.

2,2'-(4-(3-(2-(16-((7-methoxy-2-oxo-2H-chromen-4-yl)methyl)-1,4,10,13-tetraoxa-7,16-diazacyclooctadecan-7-yl)acetamido)propyl)-10-(2-((4-nitrophenethyl)amino)-2-oxoethyl)-1,4,7,10-tetraazacyclododecane-1,7-diyl)diacetic acid (**L^6**)

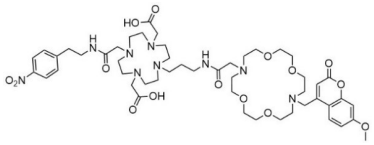

Yield: off-white solid (69%); **^{1}H NMR** (300 MHz, D_2O): δ (ppm) 7.99 (d, *J* = 8.31 Hz, 2H, Ar*H*), 7.62 (d, *J* = 9.06 Hz, 1H, Ar*H*), 7.36 (d, *J* = 8.50 Hz, 2H, Ar*H*), 6.95 (dd, *J* = 8.88, 2.27 Hz, 1H, Ar*H*), 6.89–6.77 (m, 1H, C=C*H*COMe), 6.61 (br s, 1H, C=C*H*CO$_2$C), 4.09 (br s, 2H, NCH_2C=CH), 3.95–2.73 (br, 57H, CH_2 and OCH_3), 2.51 (br s, 2H, NCH_2CH$_2$CH$_2$), 1.63 (br s, 2H, CH$_2$CH_2CH$_2$); **^{13}C NMR** (75 MHz, D_2O): δ (ppm) 170.2, 169.5, 164.7, 163.3, 162.5, 154.9, 147.9, 146.1, 145.8, 130.0, 125.5, 123.5, 114.0, 113.4, 111.0, 101.5, 69.9, 69.8, 64.1, 63.3, 56.4, 56.2, 56.1, 55.5, 54.6, 54.4, 53.6, 51.2, 50.7, 50.0, 48.4, 48.1, 39.7, 37.5, 34.7, 24.8; **HRMS (ESI-TOF):** *m/z* [M + 2H]$^{2+}$ calcd. for $C_{50}H_{77}N_9O_{15}^{2+}$ 521.7764, found 521.7766.

General synthetic procedure for **GdL$^{1\text{-}6}$**

The final ligand **L$^{1\text{-}6}$** was dissolved in MilliQ H_2O (3 mL), and the pH of the reaction media was adjusted to 7.2 with $NaOH_{(aq.)}$ (0.1 M). Then the corresponding amount of $LnCl_3$ dissolved in MilliQ H_2O (1 mL) was added portionwise over 0.5 h, during which the pH of the reaction was maintained at 7.2. After the addition was completed, the temperature of the reaction mixture was elevated to 60°C and stirred for 16 h. Then the solvent was evaporated under reduced pressure, and the acquired complex was freeze-dried on a lyophilizer for 24 h.

GdL[1]: White solid. LRMS *m/z* $[M+H]^+$ calcd. for $C_{38}H_{63}GdN_7O_{11}^+$ 951.4, found 951.4; **GdL[2]:** White solid. LRMS *m/z* $[M]^+$ calcd. for $C_{46}H_{71}GdN_9O_{12}^+$ 1099.4, found 1099.5; **GdL[3]:** White solid. LRMS *m/z* $[M + Na]^+$ calcd. for $C_{41}H_{66}GdN_9NaO_{14}^+$ 1089.4, found 1089.4; **EuL[3]:** White solid. LRMS *m/z* $[M + Na]^+$ calcd. for $C_{41}H_{66}EuN_9NaO_{14}^+$ 1084.4, found 1084.4; **GdL[4]:** White solid. LRMS *m/z* $[M + Na]^+$ calcd. for $C_{40}H_{67}GdN_9NaO_{15}P^+$ 1125.4, found 1125.4; **GdL[5]:** Off-white solid. LRMS *m/z* $[M + H]^{2+}$ calcd. for $C_{39}H_{65}GdN_8O_{13}^{2+}$ 505.7, found 505.7; **EuL[5]:** Off-white solid. LRMS *m/z* $[M + H]^{2+}$ calcd. for $C_{39}H_{65}EuN_8O_{13}^{2+}$ 503.2, found 503.3; **GdL[6]:** Dark yellow solid. LRMS *m/z* $[M + H]^{2+}$ calcd. for $C_{50}H_{74}GdN_9O_{15}^{2+}$ 599.2, found 599.3.

6.2.8 Chromatographic purification

The method used is displayed below with the flow rate of 10 mL/min. Solvents used for reverse-phase HPLC purification were grade and previously acidified with 0.1% either formic acid or TFA.

Time (min.)	**0:0**	**1:00**	**3:00**	**5:00**	**7:00**	**15:00**	**25:00**	**30:00**
MeCN (%)	0	5	10	15	20	25	50	90
H_2O (%)	100	95	90	85	80	75	50	10

6.2.9 Supplemental Figures

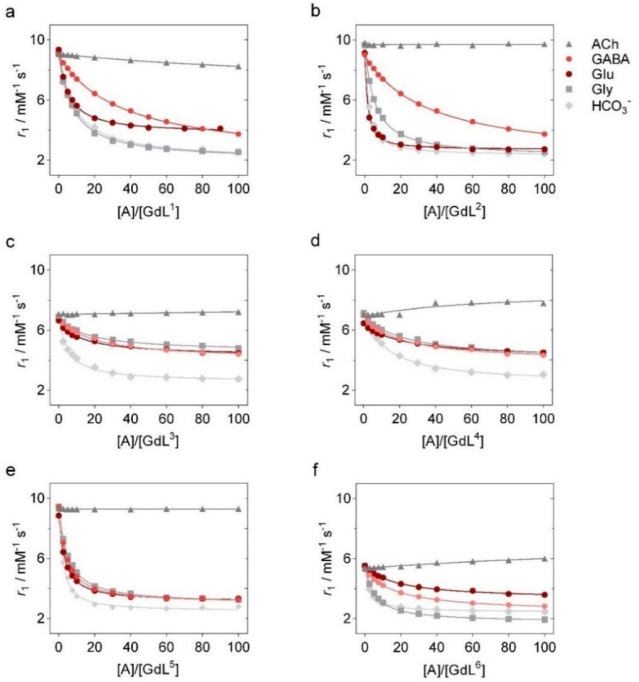

Figure S2.1. Relaxometric response of **GdL$^{1-6}$** to various analytes. Decrease in r_1 relaxivity for (**a**)–**(e)** 3.0 mM **GdL$^{1-5}$** and (**f**) 1.0 mM **GdL^6** in 50 mM HEPES induced by titration with various analytes (0-100 equiv.) at 25°C (pH 7.4, 300 MHz). The symbols are experimental data, and the lines represent fits. Plotting the molar r_1 values, calculated to Eq. S2.1, *versus* the amount of added analyte and fitting the obtained curves to the *Michaelis-Menten* model (Eq. S2.2) provided the K_a values for the corresponding ternary complexes.

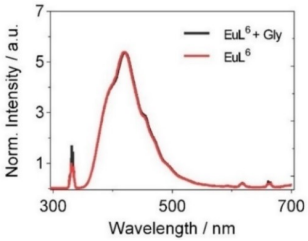

Figure S2.2. Luminescence emission spectra od **EuL^6** before and after the addition of 50 equiv. of Gly (λ_{ex} = 330 nm, [**EuL^6**] = 50 μM, 50 mM HEPES, 298 K).

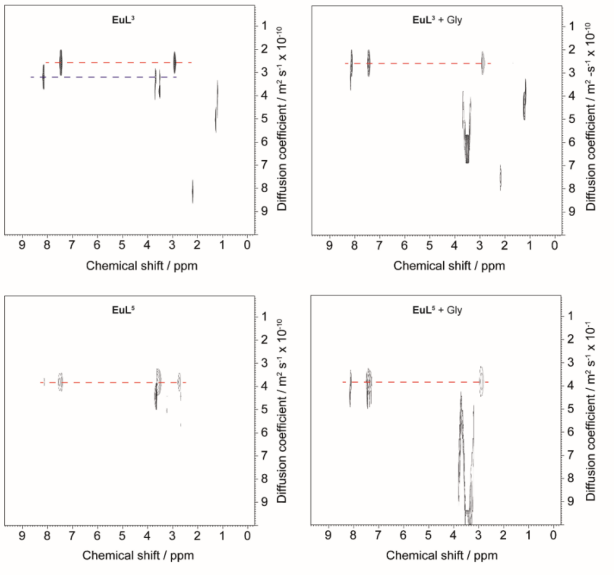

Figure S2.3. ^{1}H DOSY plots of **EuL^{3}** (top) and **EuL^{5}** (bottom) in D_2O before (left) and after (right) addition of 50 equiv. of Gly ([**EuL^{3,5}**] = 10 Mm, 298 K, 300 MHz).

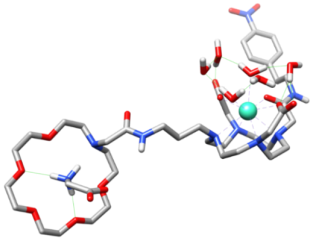

Figure S2.4. Structure of the **GdL^{5}**(Gly)$(H_2O)_2 \cdot 4H_2O$ system obtained with DFT calculations showing the binding of Gly to the crown moiety.

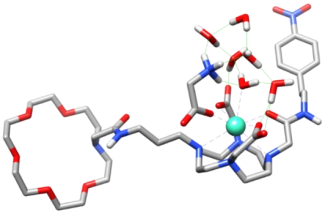

Figure S2.5. Structure of the **GdL^5**(Gly)(H_2O)·5H_2O system obtained with DFT calculations showing the binding of Gly to the metal ion.

Table S2.1. Binding affinity constants (M^{-1}) of **GdL$^{1–6}$** upon addition of 60 equiv. of analytes. [a] [b]

Complex	Gly	GABA	Glu	HCO_3^-	ACh
K_{GdL1}	47	10	73	40	2
K_{GdL2}	68	78	311	216	N/A
K_{GdL3}	23	19	26	72	N/A
K_{GdL4}	16	17	15	26	5
K_{GdL5}	76	92	114	188	N/A
K_{GdL6}	69	20	19	150	1

[a] K_a values were obtained by fitting r_1 titration curves according to Eq. S2.2.
[b] Conditions: [**GdL$^{1-5}$**] = 3.0 mM, [**GdL^6**] = 1.0 mM, 50 mM HEPES, pH 7.4, 25°C, 300 MHz.

Table S2.2. Ratio of $^5D_0 \rightarrow {}^7F_2$ to $^5D_0 \rightarrow {}^7F_1$ for **EuL^3** and **EuL^5** before and after the addition of 50 equiv. of Gly. [a] [b]

Complex	EuL^3	EuL^3-Gly	EuL^5	EuL^5-Gly
Ratio	3.17	3.20	1.80	3.37

[a] Conditions: [**EuL^{3,5}**] = 5.0 mM, 50 mM HEPES, pH 7.4, 25°C. [b] λ_{ex} = 395 nm, λ_{em} = 616 nm.

6.2.10 NMR Spectra

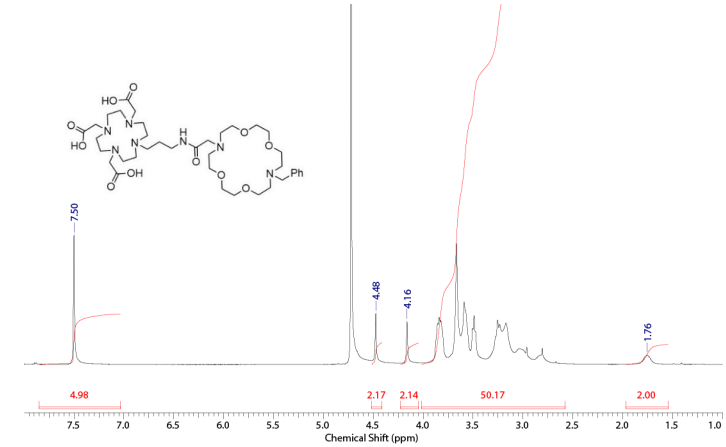

Figure S2.6. ^{1}H NMR spectrum of **L^{1}** in D_2O (300 MHz, 298K).

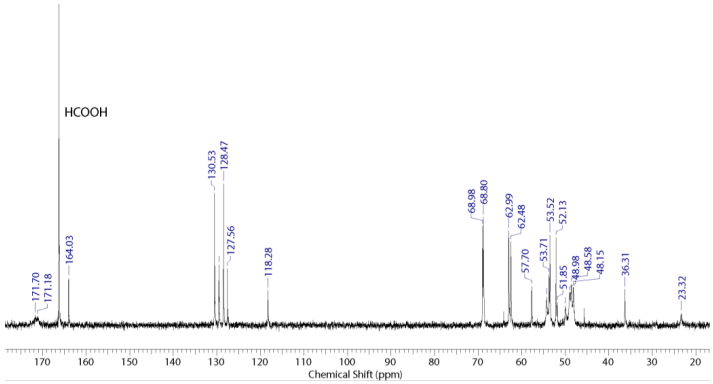

Figure S2.7. ^{13}C NMR spectrum of **L^{1}** in D_2O (75 MHz, 298K).

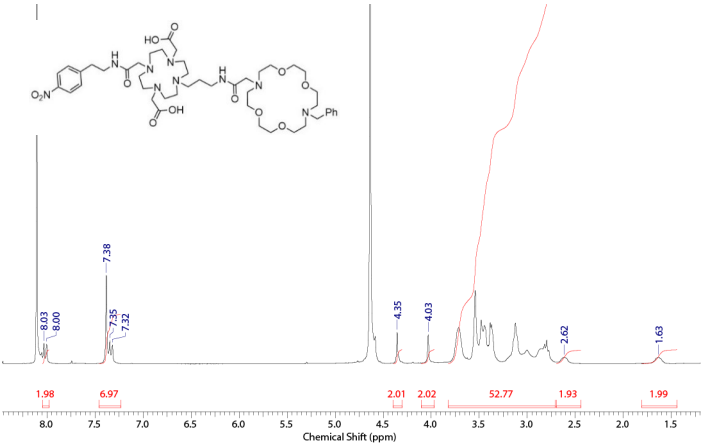

Figure S2.8. ^{1}H NMR spectrum of **L²** in D_2O (300 MHz, 298K).

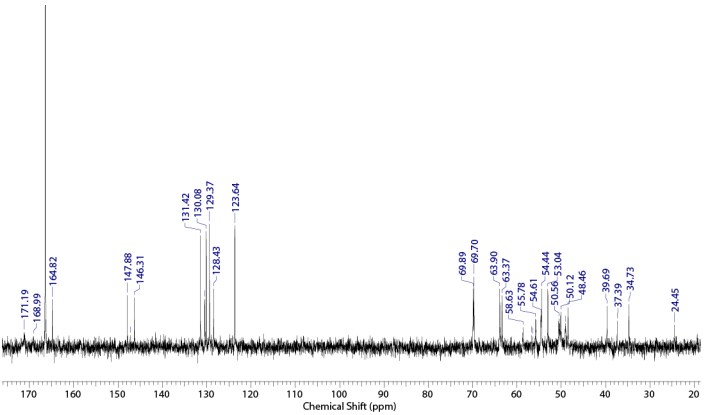

Figure S2.9. ^{13}C NMR spectrum of **L²** in D_2O (75 MHz, 298K).

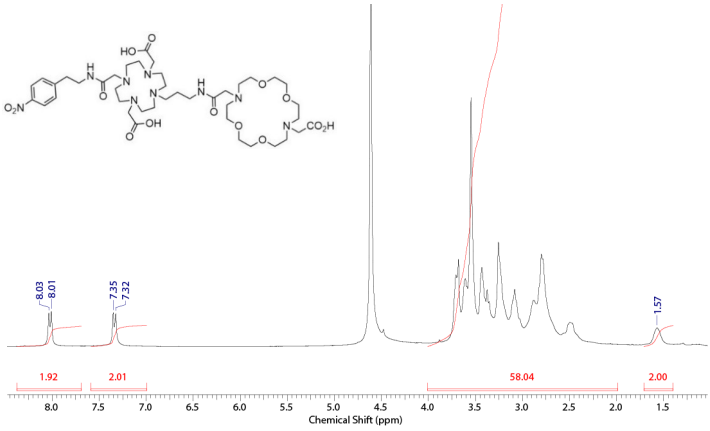

Figure S2.10. ^{1}H NMR spectrum of **L^{3}** in D_2O (300 MHz, 298K).

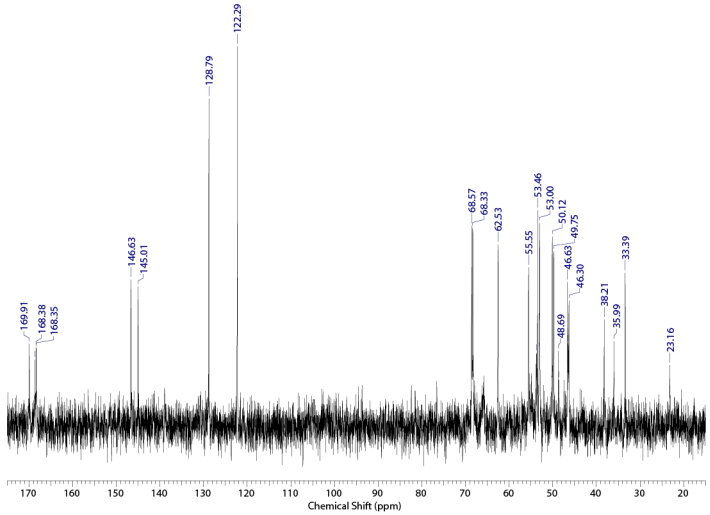

Figure S2.11. ^{13}C NMR spectrum of **L^{3}** in D_2O (75 MHz, 298K).

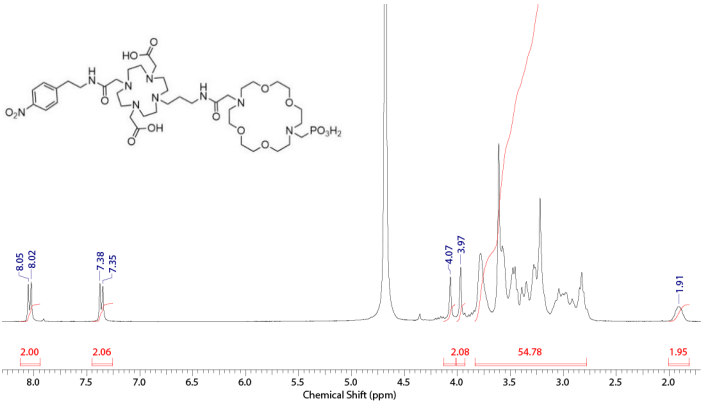

Figure S2.12. ^{1}H NMR spectrum of **L^{4}** in D_2O (300 MHz, 298K).

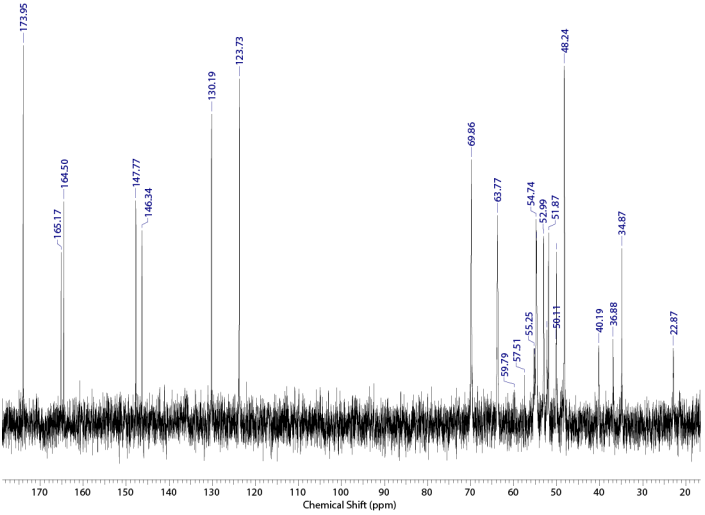

Figure 2.13. ^{13}C NMR spectrum of **L^{4}** in D_2O (75 MHz, 298K).

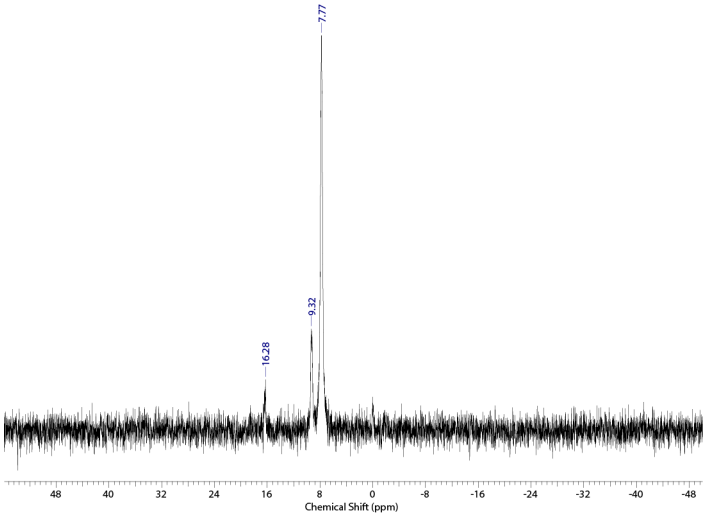

Figure S2.14. ^{31}P NMR spectrum of **L⁴** in D_2O (121 MHz, 298 K).

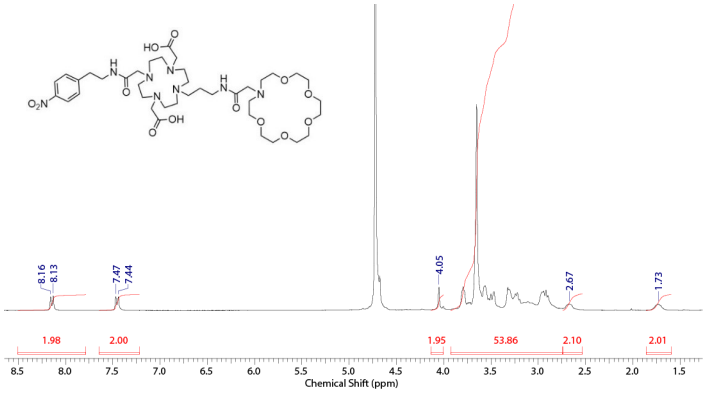

Figure S2.15. ^{1}H NMR spectrum of **L⁵** in D_2O (300 MHz, 298K).

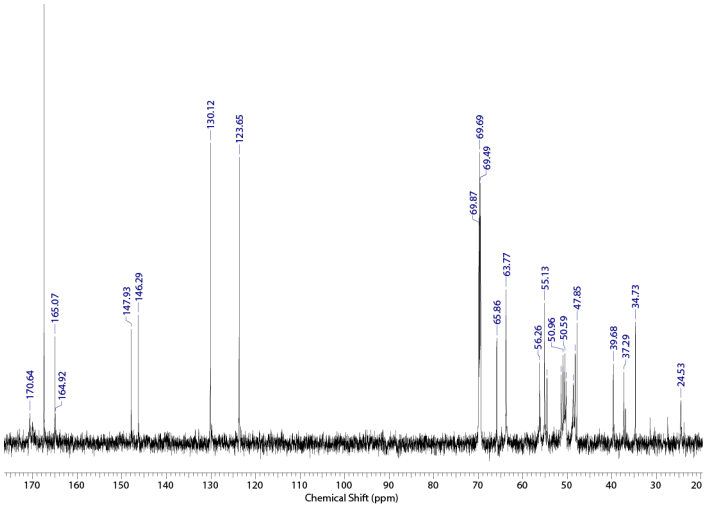

Figure S2.16. ^{13}C NMR spectrum of **L^5** in D_2O (75 MHz, 298K).

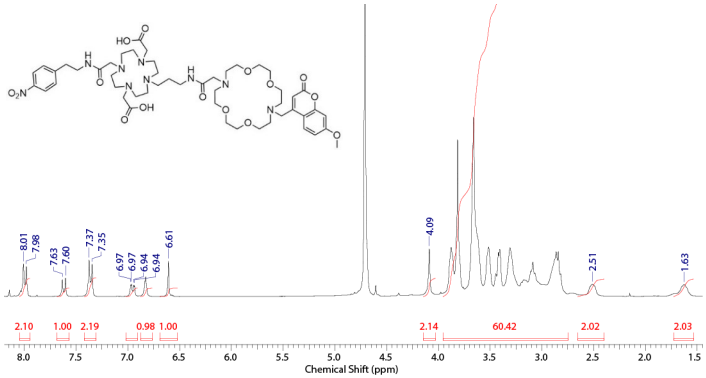

Figure S2.17. ^1H NMR spectrum of **L^6** in D_2O (pH 7.4, 300 MHz).

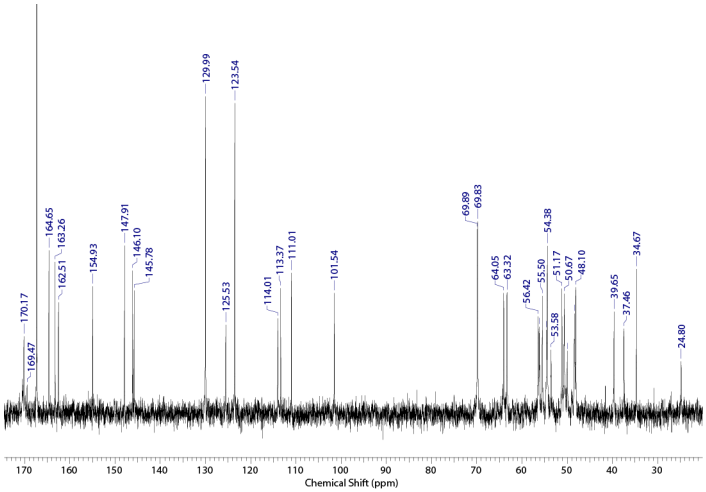

Figure S2.18. ^{13}C NMR spectrum of **L⁶** in D_2O (75 MHz, 298K).

6.3 Appendix B

6.4 Experimental Section

6.4.1 Materials and methods

For general methods, see Chapter 2.

6.4.2 Estimation of rotational correlation time by ^{1}H NMR

The hydrodynamic radii, R_h, were calculated as described in Chapter 2. The rotational correlation time (τ_R) was calculated using the SED model shown in Eq. S3.1, which establishes the relation between translational and rotational motions of a solute.[360, 361]

$$\tau_R = \frac{4\pi\eta {R_h}^3}{3kT} \qquad (S3.1)$$

where η for D_2O at 25°C is 8.87×10^{-4} Pa s.

6.4.3 Conformational dynamics

T_1 values of 15 mM **YL^7** and its ternary adducts with HCO_3^- and Glu in D_2O as a solvent were measured at 25°C (pD 7.8, 800 MHz), using the default inversion recovery pulse sequence (180° – τ - 90°). 24 different values for τ, in the range from 0.02 to 10.0 s, were used between 180° and 90° high-power pulses and pulse delays 5 times longer than the longest T_1 being measured with 8 scans. The obtained data were fitted in the T_1 /T_2 relaxation module using two parameters exponential fit.

6.4.4 MRI Phantoms

MRI measurements were performed on a Bruker BioSpec 70/30 USR magnet (software version Paravision 5.1) using a Bruker volume coil (RF RES 300 1H 075/040 QSN TR). Images were obtained using T_1, T_2, and T_2/T_1-weighted imaging protocols, acquired with Fast Low Angle Shot (FLASH), Multi-slice Multi-echo (MSME), and Steady State Free Precession (bSSFP) pulse sequences. Phantom consisted of 7 capillaries filled with 150 µL, where 5 capillaries contained 1.5 mM of **GdL^7** and an addition of 60 equivalents of the guest molecules: (GABA, Glu, Gly, ACh and HCO_3^-). As references, 1.5 mM **GdL^7** and 50 mM HEPES (pH 7.4) were used. Common imaging parameters were: Field of view (FOV) 30 x 30, matrix size (MTX) 150 x 150, slice thickness 1 mm, number of excitations (NEX) 10; the rest of the parameters specific for each sequence are given below. FLASH: repetition time (TR) = 30 ms, echo time (TE) = 2.75 ms, flip angle (FA) = 90^0, acquisition time (TA) = 45 s; MSME: TR = 900, TE = 30 (60) ms, TA = 22 m 30 s; bSSFP: TR = 2.1 (2.7) ms, TE = 1.05 (1.35) ms, FA = 70^0, TA = 17 s 115 ms (17 s 57 ms).

6.4.5 Synthetic Procedures

N-(4-nitrophenethyl)-2-(1,4,10,13-tetraoxa-7,16-diazacyclooctadecan-7-yl)acetamide (**3-1**)

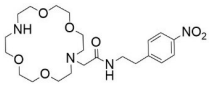

To a stirred solution of 4,13-diaza-18-crown 6-ether (700 mg, 2.61 mmol) in MeCN (30 mL) was added $NaHCO_3$ (264 mg, 3.14 mmol) and the mixture was stirred for 45 min. followed by dropwise addition of compound **3** (826 mg, 2.88 mmol) dissolved in MeCN (20 mL). After the addition was completed, the temperature was elevated to 50°C and the mixture was stirred vigorously for 2 days. Then the solvent was reduced under the vacuum, and the solid residue was purified on a silica column to yield **3-1** (637 mg, 53%) as a pale yellow solid. R*f* = 0.53 ($MeOH/CH_2Cl_2$, 20:80); **^{1}H NMR** (300 MHz, $CDCl_3$): δ (ppm) 8.15 (d. *J* = 8.12 Hz, 2H, Ar*H*), 7.49 (d, *J* = 8.5 Hz, 2H, Ar*H*), 4.10 – 2.44 (br, 30H, CH_2); **^{13}C NMR** (75 MHz, $CDCl_3$) δ (ppm) 171.4, 147.5, 146.4, 129.9, 123.5, 70.2, 69.9, 68.3, 66.1, 56.8, 53.6, 48.3, 39.8, 35.3; **HRMS (ESI-TOF)** *m/z* $[M + H]^+$ calc. for $[C_{22}H_{36}N_4O_7]$ 469.26568, found 469.26660.

tri-tert-butyl 2,2',2''-(10-(3-(2-(16-(2-((4-nitrophenethyl)amino)-2-oxoethyl)-1,4,10,13-tetraoxa-7,16-diazacyclooctadecan-7-yl)acetamido)propyl)-1,4,7,10 tetraazacyclododecane -1,4,7-triyl)triacetate (**3-2**)

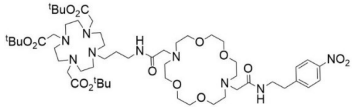

To a stirred solution of **3-1** (1.0 g, 3.74 mmol) in DMF (8 mL) was added $NaHCO_3$ (200 mg, 2.36 mmol), and the mixture was stirred for 1 h, followed by dropwise addition of **2** (754 mg, 1.09 mmol), and the resulting mixture was stirred at room temperature for 2 days. Then the solvent was removed under the reduced pressure, and the solid residue was purified on a silica gel column (5% $MeOH/CH_2Cl_2$) to give compound **3-2** (0.79 g, 60%) as an off-white fluffy solid: R_f = 0.41 ($MeOH/CH_2Cl_2$, 15:85); **^{1}H NMR** (300 MHz, $CDCl_3$): δ (ppm) 9.03 – 8.77 (overlapped m, 1H, CON*H*), 8.76 – 8.47 (overlapped m, 1H, CON*H*), 8.10 (d, *J* = 8.5 Hz, 2H, Ar*H*), 7.60 (d, *J* = 8.5 Hz, 2H, Ar*H*), 3.84 – 1.98 (br, 60H, CH_2); 1.79 (br. s, 2H, $CH_2CH_2CH_2$); 1.65 – 1.29 (overlapped s, 27H, CH_3); **^{13}C NMR** (75 MHz, $CDCl_3$) δ (ppm) 173.5, 172.0, 171.7, 171.5, 148.3, 146.3, 130.5, 123.3, 82.7, 82.5, 68.9, 68.4, 67.0, 67.0, 60.0, 58.6, 56.6, 55.5, 54.9, 55.5, 54.9, 53.9, 53.5, 51.6, 50.2, 47.6, 39.9, 37.3, 35.3, 24.3; **HRMS (ESI-TOF)** *m/z* $[M + H]^+$ calc. for $[C_{53}H_{94}N_9O_{14}]^+$ 1080.69148, found 1080.68958.

tri-*tert*-butyl 2,2',2''-(10-(3-(2-(16-(2-((4-aminophenethyl)amino)-2-oxoethyl)-1,4,10,13-tetraoxa-7,16-diazacyclooctadecan-7-yl)acetamido)propyl)-1,4,7,10-tetraazacyclododec-ane-1,4,7-triyl)triacetate (**3-3**)

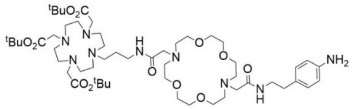

To a solution of **3-2** (445 mg, 0.41 mmol) in EtOH (25 mL), the catalyst $Pd(OH)_2/C$ (20% w/w) was suspended, followed by the addition of a catalytic amount of NH_4OH (50 µL, 7N solution in MeOH). Then the suspension was shaken in Parr's hydrogenator for 8 h, filtered off through a diatomaceous earth pad, and the filtrate was evaporated to yield **3-3** (364 mg, 84%) as a dark green-brownish fluffy solid. **^{1}H NMR** (300 MHz, $CDCl_3$): δ (ppm) 7.47 – 7.27 (m, 1H, CON*H*), 7.16 – 6.81 (d, 2H, Ar*H*), 6.80 – 6.35 (d, 2H, Ar*H*), 3.98 – 2.05 (br, 58H, CH_2); 1.70 (br. s, 2H, $CH_2CH_2CH_2$); 1.61 – 1.30 (overlapped s, 27H, CH_3); **^{13}C NMR** (75 MHz, $CDCl_3$) δ (ppm) 173.5, 172.5, 171.7, 171.5, 145.0, 129.4, 128.6, 115.2, 82.7, 82.4, 70.5, 69.3, 59.3, 59.2, 56.6, 56.5, 55.7, 55.4, 55.3, 52.4, 51.8, 50.7, 50.0, 40.6, 37.2, 34.7, 28.0, 27.8, 25.5; **HRMS (ESI-TOF)** *m/z* $[M + Na]^+$ calc. for $[C_{53}H_{95}N_9NaO_{12}]^+$ 1072.69924, found 1072.69741.

2,2',2''-(10-(3-(2-(16-(2-((4-formamidophenethyl)amino)-2-oxoethyl)-1,4,10,13-tetraoxa-7,16-diazacyclooctadecan-7-yl)acetamido)propyl)-1,4,7,10-tetraazacyclododecane-1,4,7-triyl)triacetic acid (**L^7**)

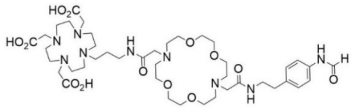

Compound **3-3** (350 mg, 0.333 mmol) was dissolved in formic acid (8 mL), and the resulting solution was vigorously stirred at 60°C overnight. The solvent was then evaporated, and the residue was purified by RP-HPLC using a gradient of acetonitrile in water to yield **L^7** (195 mg, 64%) as a white solid. ^{1}H NMR analysis evidenced the presence of isomers in the ratio 76:24. **^{1}H NMR** (300 MHz, D_2O): δ (ppm) enolate form: 8.56 (s, 1H, NHC*H*O), 7.10 (d, *J* = 7.39 Hz, 2H, Ar*H*), keto form: 8.19 (s, 1H, NHC*H*O), 7.41 (d, *J* = 7.52 Hz, 2H, Ar*H*), (keto + enol form) 7.29 – 7.13 (overlapping, 4H, Ar*H*), 3.95 – 2.35 (br, 58H, CH_2), 1.81 (br. s, 2H, $CH_2CH_2CH_2$); **^{13}C NMR** (75 MHz, D_2O) δ (ppm); 173.4, 169.2, 167.3, 163.8, 160.9, 135.0, 133.8, 133.5, 129.0, 128.5, 119.7, 117.6, 68.4, 65.2, 64.2, 55.4, 54.8, 54.4, 53.7, 53.6, 49.6, 49.0, 48.4, 39.1, 35.6, 32.6, 22.2; **HRMS (ESI-TOF)** *m/z* $[M + 2H]^{2+}$ calc. for $[C42H73N9O13]^{2+}$ 455.76584, found 455.76502.

General procedure for complexation ligand **L^7**

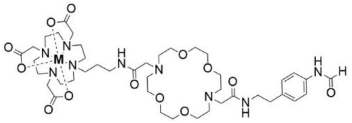

The final ligand **L^7** was dissolved in MilliQ H_2O (2 mL), and the pH of the reaction media was adjusted to 7.2 with $NaOH_{(aq.)}$ (0.2 M). Then the amount of $GdCl_3$ corresponding to 0.8 equiv. of **L^7** was dissolved in MilliQ H_2O (1 mL) and was added in a dropwise manner over 0.5 h, during which the pH of the reaction was maintained at 7.2. After the addition was completed, the temperature of the reaction mixture was elevated to 60°C and stirred for 4 h. Then the solvent was evaporated under the reduced pressure, and the product was purified by RP-HPLC followed by lyophilization for 24 h.

2,2',2''-(10-(3-(2-(16-(2-((4-formamidophenethyl)amino)-2-oxoethyl)-1,4,10,13-tetraoxa-7,16-diazacyclooctadecan-7-yl)acetamido)propyl)-1,4,7,10-tetraazacyclododecane-1,4,7-triyl)triacetic acid (**GdL^7**)

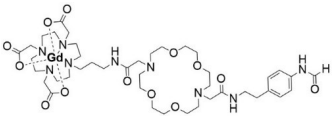

GdL^7 was obtained as a white solid, 30 mg (74%). **HRMS (ESI-TOF)** *m/z* $[M - H]^-$ calc. for $[C_{42}H_{67}N_9O_{13}Gd]^-$ 1063.41049, found 1063.41154.

2,2',2''-(10-(3-(2-(16-(2-((4-formamidophenethyl)amino)-2-oxoethyl)-1,4,10,13-tetraoxa-7,16-diazacyclooctadecan-7-yl)acetamido)propyl)-1,4,7,10-tetraazacyclododecane-1,4,7-triyl)triacetic acid (**YL^7**)

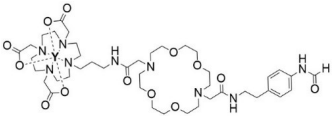

YL^7 was obtained as a white solid, 50.9 mg (76%). ^{1}H NMR analysis evidenced the presence of isomers in the ratio 72:28. **^{1}H NMR** (300 MHz, D_2O): δ (ppm) enolate form: 8.61 (s, 1H, NHC*H*O), 7.15 (d, *J* = 7.43 Hz, 2H, Ar*H*), keto form: 8.21 (s, 1H, NHC*H*O), 7.44 (d, *J* = 7.63 Hz, 2H, Ar*H*), (keto + enol form) 7.35 – 7.20 (overlapping, 4H, Ar*H*), 3.78 – 2.28 (br, 58H, CH_2), 1.69 (br. s, 2H, $CH_2CH_2CH_2$); **HRMS (ESI-TOF)** *m/z* $[M - H]^-$ calc. for $[C_{42}H_{67}N_9O_{13}Y]^-$ 994.39223, found 994.39347.

6.4.6 Supplemental Figures

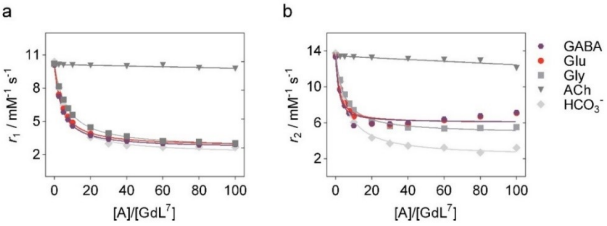

Figure S3.1. Relaxometric profiles of **GdL^7** in response to various analytes. The schematic depiction of experimentally measured (symbols) and fitted (curves) data for (**a**) longitudinal r_1 and (**b**) transverse r_2 relaxometric titration curves for 2.5 mM [Gd^{3+}] with various analytes (0 – 100 equiv.) in 50 mM HEPES (pH 7.4, 7.05 T) at 25°C. Plotting the molar r_1 values, calculated to Eq. S2.1, versus the amount of added analyte and fitting the obtained curves to the *Michaelis-Menten* model (Eq. S2.2) provided the K_a values for the corresponding ternary complexes.

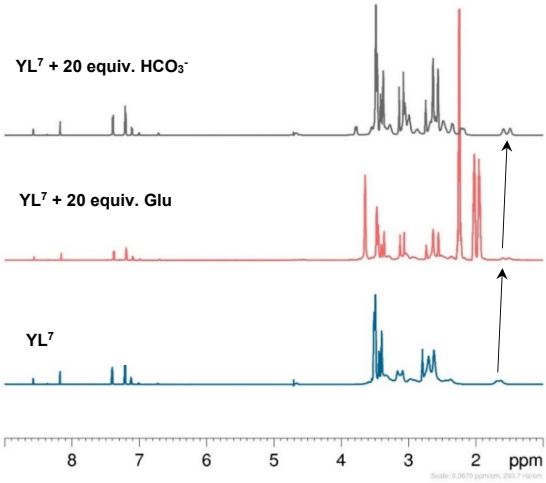

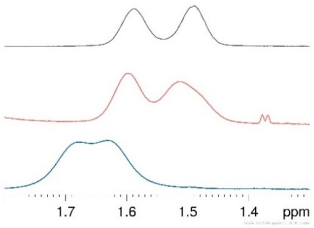

Figure S3.2. ^{1}H NMR spectra of 15 mM **YL^7** in the absence and upon addition of 20 equiv. of Glu and HCO_3^- in D_2O (pD 7.8, 800 MHz). Significant signal shifts and multiplicity changes can be observed in the aliphatic protons induced by interaction with Glu or HCO_3^-.

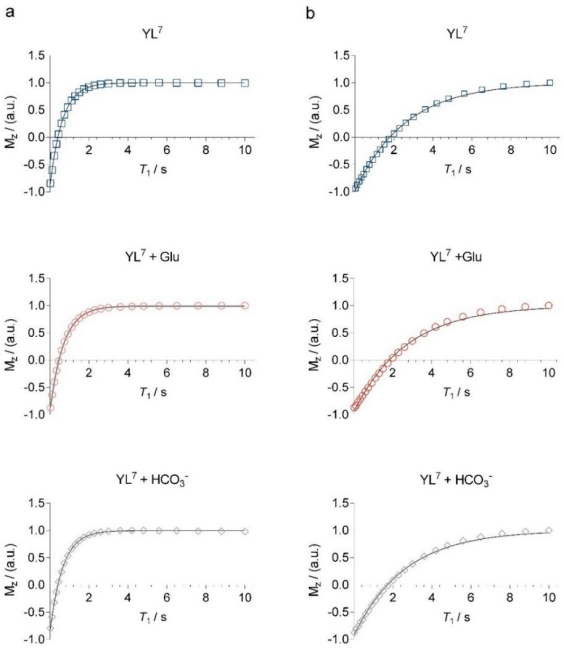

Figure S3.3. Characterization of conformational mobility of **YL^7** in the presence of various analytes. T_1-values for (**a**) $NCH_2\underline{CH_2}O$ group within the 18C6 ring frame and (**b**) the *meta*-H within the aromatic ring in the 18C6 pending arm for 10 mM of the binary complex **YL^7 alone** and in the presence of 20 equiv. of Glu and hydrogencarbonate. Symbols are experimentally measured values, and curves represent fits.

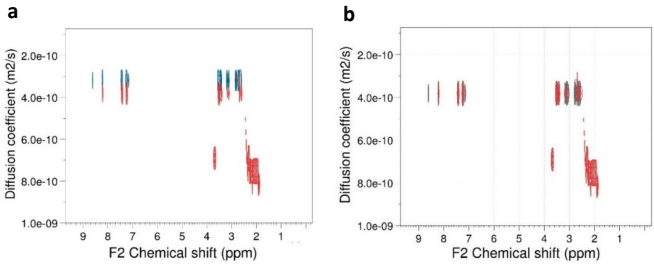

Figure S3.4. Overlay of ^{1}H 2D DOSY plots of (**a**) **YL^{7}** and **YL^{7}**(Glu) and (**b**) **YL^{7}** and **YL^{7}**(HCO_3^-) displaying changes in diffusion coefficient of binary complex upon addition of analytes (298 K, 300 MHz).

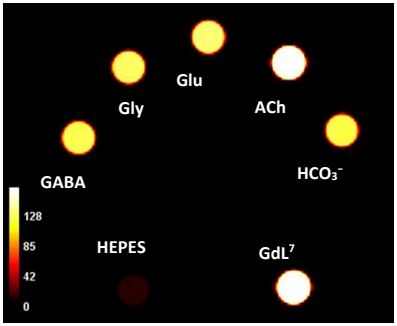

Figure S3.5. T_2w phantom image of **GdL^{7}** (1.5 mM) with ZNTs and competitive metabolites in a ratio of 1:60 buffered in 50 Mm HEPES (298 K, pH 7.4, 7 T).

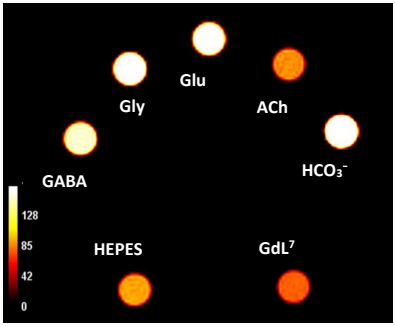

Figure S3.6. T_2w phantom image of **GdL^{7}** (1.5 mM) with ZNTs and competitive metabolites in a ratio of 1:60 buffered in 50 Mm HEPES (298 K, pH 7.4, 7 T).

Table S3.1. SNR values obtained in T_1**w**, T_2**w** and T_1/T_2**w** MRI phantom experiments for **GdL^7** with analytes in the ratio 1:60. [a] [b]					
SNR	**GdL^7**	**YL^7(HCO$_3^-$)**	**GdL^7(Glu)**	**GdL^7(Gly)**	**GdL^7(GABA)**
T_1**w**	434	229	246	241	235
T_2**w**	56	164	119	133	108
T_1/T_2**w**	196	196	177	189	175

[a] [**YL^7**] = 1.2 mM, 50 mM HEPES, pH 7.4, 298 K, 7 T. [b] Host to guest ratio 1:60.

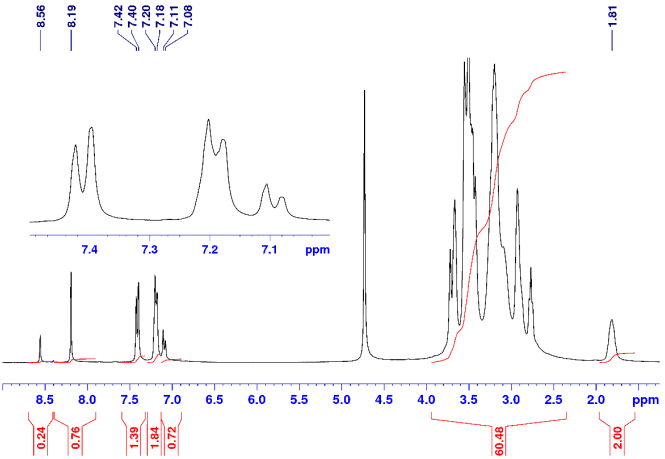

Figure S3.7. ^{1}H NMR spectrum of **L^7** in D_2O (pD 7.8, 300 MHz).

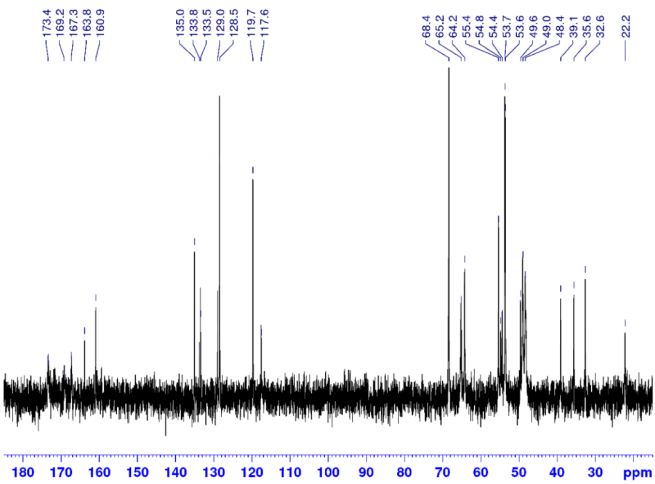

Figure S3.8. ^{13}C NMR spectrum of **L⁷** in D_2O (pD 7.8, 75 MHz).

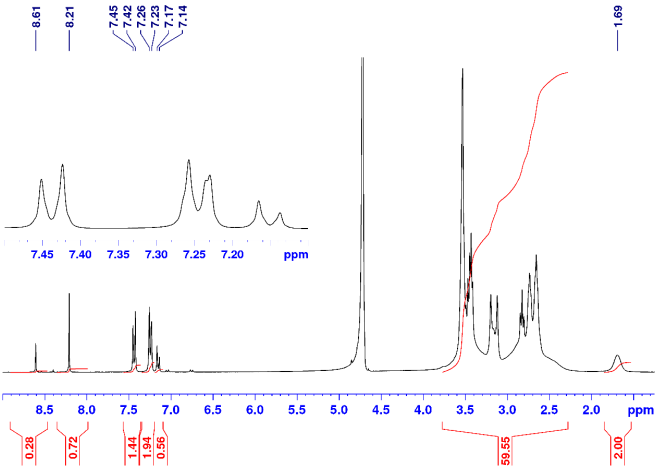

Figure S3.9. ^{1}H NMR spectrum of **YL⁷** in D_2O (pD 7.8, 300 MHz).

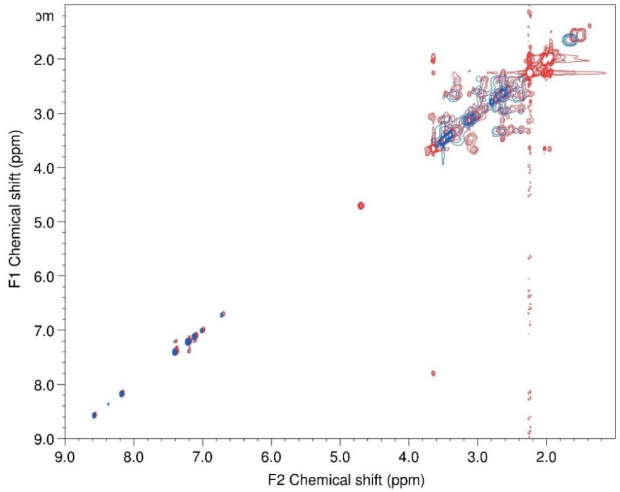

Figure S3.10. Overlapped 2D EXSY NMR spectra of **YL^7** (blue) and **YL^7**-Glu (red) in a ratio of 1.0 : 20 measured in D_2O at 25ºC (pD 7.8, 800 MHz).

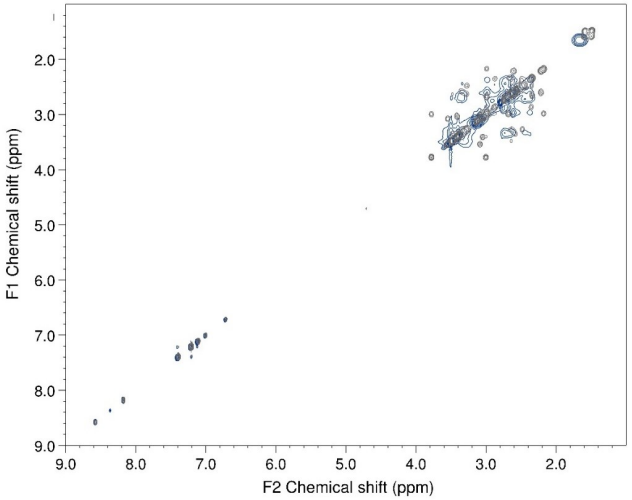

Figure S3.11. Overlapped 2D EXSY NMR spectra of **YL^7** (blue) and HCO_3^- (red) in a ratio of 1.0 : 20 measured in D_2O at 25ºC (pD 7.8, 800 MHz).

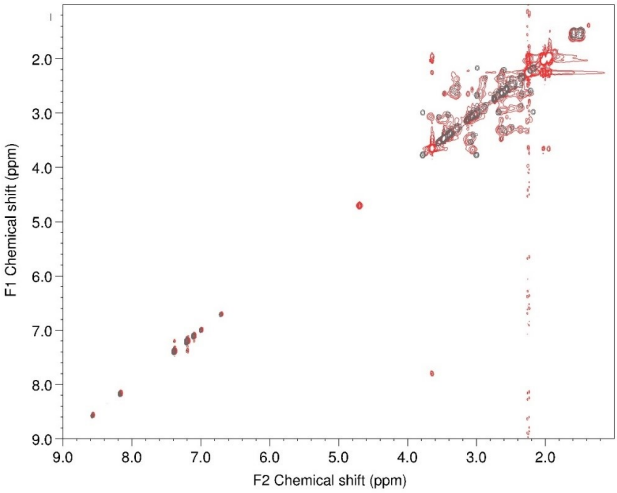

Figure S.3.12. Overlapped 2D EXSY NMR spectra of **YL^7** (blue) and Glu (red) in a ratio of 1.0 : 20 measured in D_2O at 25ºC (pD 7.8, 800 MHz).

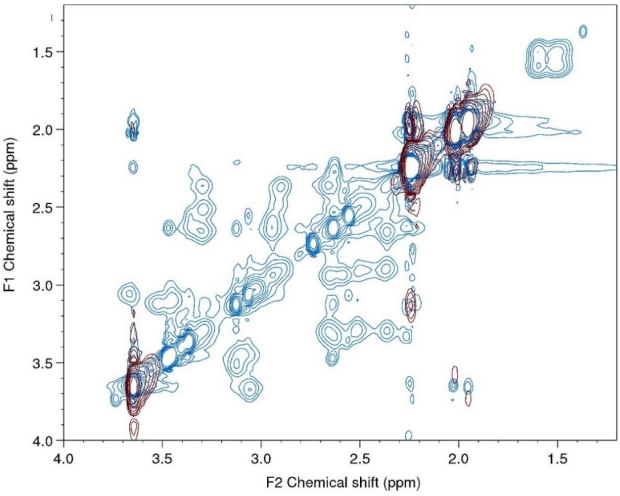

Figure S3.13. Overlapped 2D EXSY NMR spectra of **YL^7** (blue) and Glu (red) in a ratio of 1.0 : 20 measured in D_2O at 25ºC (pD 7.8, 800 MHz).

6.5 Appendix C

6.6 Experimental Section

6.6.1 Materials and Methods

Key reagents: Commercially available reagents and solvents were used without further purification. The G4 poly(amidoamine) PAMAM Starburst dendrimer (cystamine core) as a solution in methanol (10% wt/wt) was purchased from Andrews ChemService (Berrien Springs, MI, USA). Low molecular weight molecules were purified using silica gel 60 (0.03 – 0.2 mm) purchased from Carl Roth, Germany.

Purification: The lipophilic dendrimeric conjugate **4-2** was purified using lipophilic Sephadex® LH-20 (bead size: 25 – 100 µm) purchased from Sigma-Aldrich (Germany). The hydrophilic dendrimeric conjugate **GdD^1** was purified using hydrophilic Sephadex® G-15 (bead size: 40 – 120 µm) purchased from GE Healthcare. Centrifuge purification of **GdD^1** and **GdD^1-mPEG** was conducted using molecular weight cut-off filters (MWCO 30 kDa).

For the additional information, including omitted methods, see Chapter 2.

6.6.2 Estimation of PAMAM loading with sensor 4-1

The number of loaded units of the bismacrocyclic chelate precursor **4-1**, in compounds **4-2** and **D^1**, per dendrimer core was estimated by ^{1}H NMR spectra analysis according to the previously established procedure.[325]

6.6.3 Synthetic Procedures

tri-*tert*-butyl 2,2',2''-(10-(3-(2-(16-(2-((4-isothiocyanatophenethyl)amino)-2-oxoethyl)-1,-4,10,13-tetraoxa-7,16-diazacyclooctadecan-7-yl)acetamido)propyl)-1,4,7,10-tetraazacycl-ododecane-1,4,7-triyl)triacetate **(4-1)**

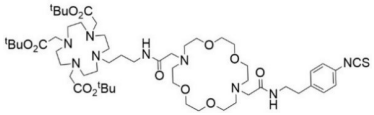

The amine **3-3** (0.538 g, 0.512 mmol) was dissolved in dry CH_2Cl_2 (25 mL), and Et_3N (0.288 mL, 2.05 mmol) was added. The thiophosgene (0.044 mL, 0.563 mmol) was added to the reaction mixture and stirred for 3 h at room temperature. The reaction mixture was filtrated off, and the solvent was evaporated under reduced pressure. The resulting crude solid was then purified by silica gel column (CH_2Cl_2/MeOH, 92:8) to yield isothiocyanate **4-1** as a brown solid (0.261 g, 47%). R_f = 0.52 (MeOH/CH_2Cl_2, 15:85); **^{1}H NMR** (300 MHz, $CDCl_3$): δ (ppm) 7.53 – 7.25 (m, 2H, Ar*H*), 7.25 – 6.59 (m, 2H, Ar*H*), 3.84 – 1.94 (br, 58H, C*H*$_2$), 1.87 – 1.68 (br. s, 2H, $CH_2CH_2CH_2$), 1.62 – 1.39 (overlapped s, 28H, (C*H*$_3$)$_3$); **^{13}C NMR** (75 MHz, $CDCl_3$): δ (ppm) 172.0, 171.8, 171.6, 170.0, 140.0, 134.3, 130.5, 128.6, 125.4, 82.6, 82.4, 81.6, 68.9, 68.4, 67.1, 59.9, 58.4, 65.5, 55.5, 54.9, 53.8, 53.1,

51.6, 50.6, 50.2, 40.5, 37.2, 35.1, 28.1, 27.6; **HRMS (ESI-TOF)** *m/z* $[M + Na + MeOH]^+$ calc. for $C_{55}H_{97}N_9NaO_{13}^+$ 1146.68188, found 1146.68151.

Compound **4-2:**

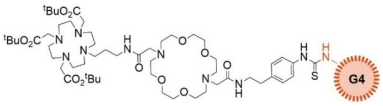

The G4 PAMAM dendrimer as a 10% w/w solution in methanol (0.344 mL, 1.91 µmol) was dried under reduced pressure and then redissolved in dry DMF (3 mL). Then the Et_3N (0.043 mL, 0.305 mmol) was added, and the resulting mixture was stirred for 45 min. The isothiocyanate **2** (200 mg, 0.183 mmol) was added in portions over 24 h and left to stir at 45°C for 2 days. Then the solvent was removed in Kugelrohr, and the resin-like dark yellow residue was purified on lipophilic Sephadex LH-20 using methanol as eluent. The G4 PAMAM-conjugate **4-2** (135 mg, 63%) was obtained as the amorphous yellow solid. As determined by the ^{1}H NMR, the **4-2** was functionalized with 42 bis-macrocyclic units. **^{1}H NMR** (300 MHz, $CDCl_3$): δ (ppm) 7.52 (br. s, 2H, ArH), 7.10 (br. s, 2H, ArH), 5.06 – 1.69 (br, 60H, C*H*$_2$), 1.45 (br. s, 27H, C(C*H*$_3$)$_3$).

Compound **D^1**:

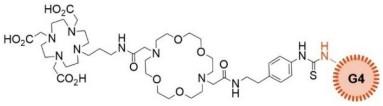

The *tert*-butyl protected dendrimer conjugate **4-2** (105 mg, 0.093 mmol) was dissolved in formic acid (6 mL) and stirred at 60°C for 24 h. Then the solvent was evaporated under reduced pressure, followed by lyophilization to acquire brown residue. The yield of the obtained product **D^1** was quantitative and in the following stage of synthesis, was used without further purification. **^{1}H NMR** (300 MHz, D_2O): δ (ppm) 7.51 – 6.96 (overlapped s, 4H, Ar*H*), 4.49 – 2.25 (br, 60H, C*H*$_2$), 1.77 (br. s, 2H, $CH_2CH_2CH_2$).

Compound **GdD^1**:

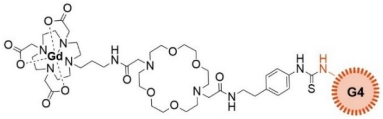

Compound **D^1** (89 mg, 0.093 mmol) was dissolved in MilliQ water, and the pH was set to 7.2 using NaOH $_{(aq.)}$ (0.1 M). Then the aqueous solution of $GdCl_3$ (28 mg, 0.075 mmol) was added portionwise over 6 hours while the pH value of the reaction mixture was maintained at 7.2. After the addition was completed, the mixture was stirred at 60°C overnight. Then the reaction mixture was cooled, and EDTA monosodium salt (17.5 mg,

0.047 mmol) was added while the pH was maintained at 7.2. The reaction mixture was stirred for 4 h, and the solvent was evaporated under reduced pressure. The obtained dark yellow residue was purified on hydrophilic Sephadex G-15 using water as eluent, and collected fractions were centrifuged using a 30 kDa MWCO for 45 min at 2000 *g*. This process was repeated until the filtrate showed an absence of GdEDTA and EDTA (checked by low-resolution ESI-MS and the xylenol orange test). The product was then lyophilized to obtain the final **GdD^1** (65 mg, 65%) as a yellow solid.

Compound **GdD^1-mPEG**:

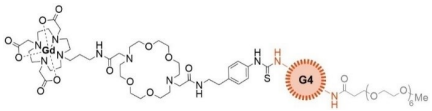

Compound **GdD^1** (47 mg, 0.042 mmol) was dissolved in HEPES (2 mL, 0.15 M, pH 7.8), and the m-PEG6-NHS ester (21.4 mg, 0.051 mmol) dissolved in HEPES (0.5 mL, 0.15 M, pH 7.8) was added. The resulting reaction mixture was left to stir for 24 h at room temperature. The reaction mixture was then transferred into a Millipore tube containing an MWCO 30 kDa filter and centrifuged multiple times until the filtrate showed the absence of PEG-specific peaks on low-resolution MS. The concentrated product was lyophilized to yield **GdD^1-mPEG** (41 mg, 75%) as an off-white fluffy solid.

6.6.4 Supporting Figures

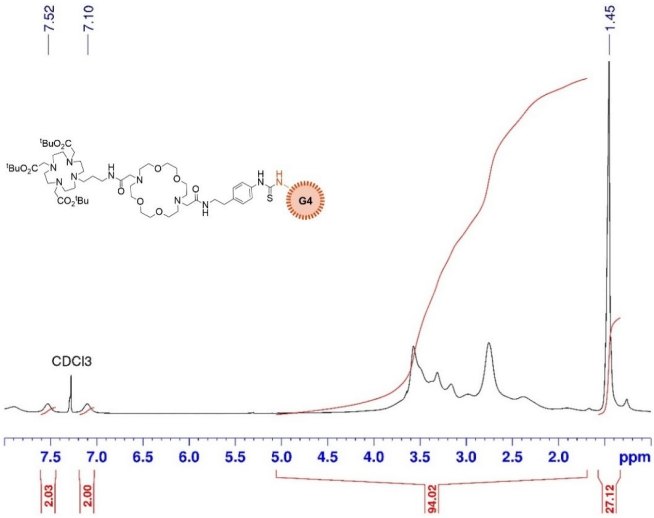

Figure S4.1. Estimation of the loading capacity of compound **4-2**. ^{1}H NMR spectra recorded in $CDCl_3$ (300 MHz, 298 K) revealed functionalization of 36 surface amines out of 64 (56%).

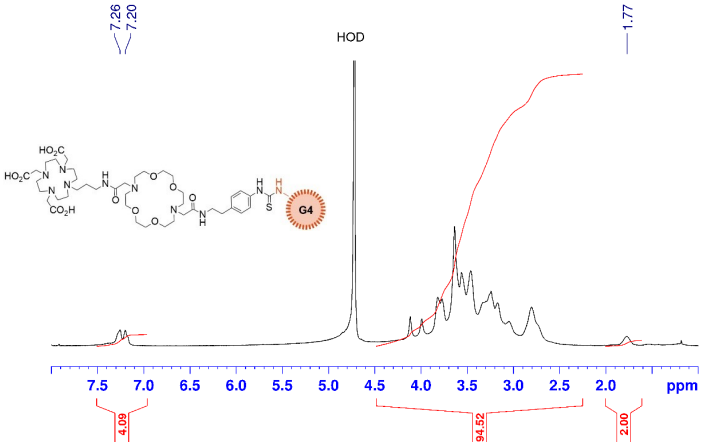

Figure S4.2. Estimation of the loading capacity of compound **D**[1]. ^{1}H NMR spectra recorded in D_2O (300 MHz, 298 K) revealed functionalization of 36 surface amines out of 64 (56%).

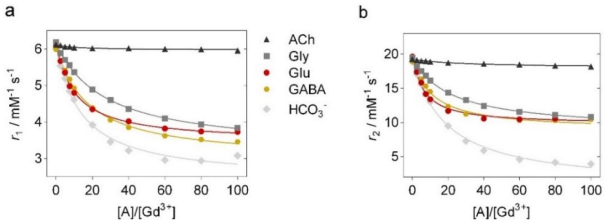

Figure S4.3. Relaxometric response of **GdD**[1]**-mPEG**$_6$ to various analytes. The schematic depiction of experimentally measured (symbols) and fitted data (curves) for (**a**) longitudinal r_1 and (**b**) transverse r_2 relaxometric titration curves for 2.5 mM [Gd^{3+}] with various analytes (0 - 100 equiv.) in 50 mM HEPES (pH 7.4, 300 MHz) at 25°C. Plotting the molar r_1 values, calculated to Eq. S2.1, versus the amount of added analyte and fitting the obtained curves to the *Michaelis-Menten* model (Eq. S2.2) provided the binding affinity constants for the corresponding ternary complexes.

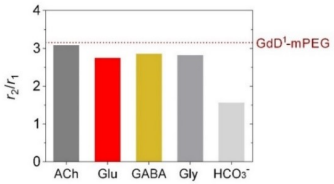

Figure S4.4. Ratiometric r_2/r_1 responsiveness of **GdD**[1]**-mPEG**$_6$ to various analytes. MR relaxivities used to calculate the ratios are measured for 2.5 mM [Gd^{3+}] before and after addition of 60 equiv. of various analytes

in 50 mM HEPES-buffered media (pH 7.4, 300 MHz) at 25°C. The depicted horizontal line represents r_2/r_1 value of **GdD^1-mPEG** in the absence of analytes. An insignificant change of the r_2/r_1 upon saturation with analytes revealed that **GdD^1-mPEG** cannot be used as the ratiometric probe.

6.6.5 MALDI-TOF Characterization

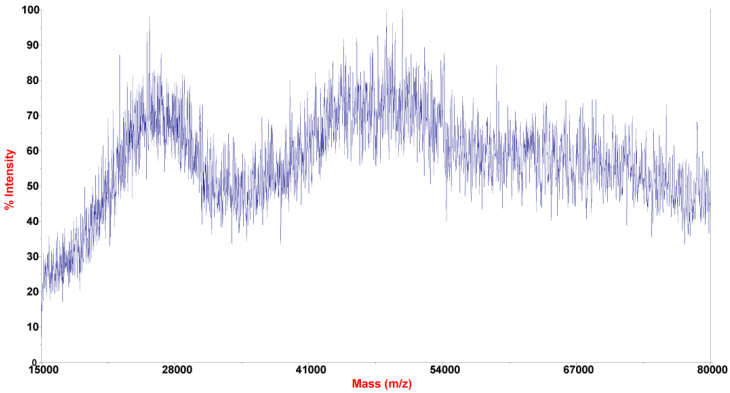

Figure S4.5. MALDI-TOF MS spectrum of **4-2** (Sinapinic acid matrix).

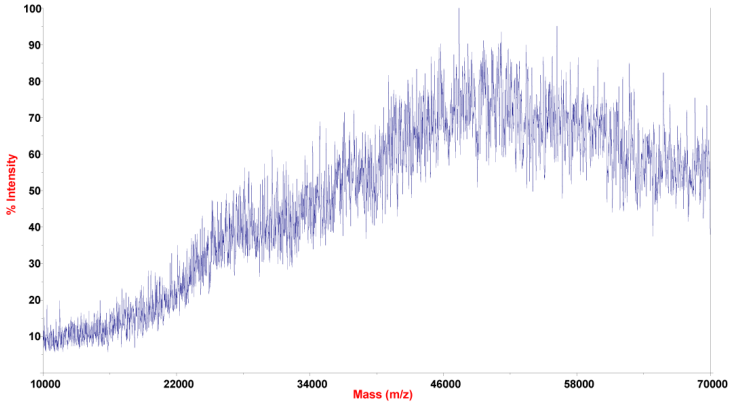

Figure S4.6. MALDI-TOF MS spectrum of **D^1** (THAP matrix).

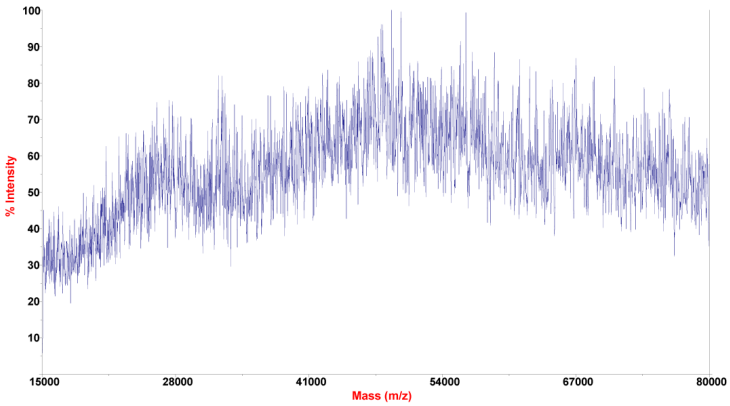

Figure S4.7. MALDI-TOF MS spectrum of **GdD[1]** (THAP matrix).

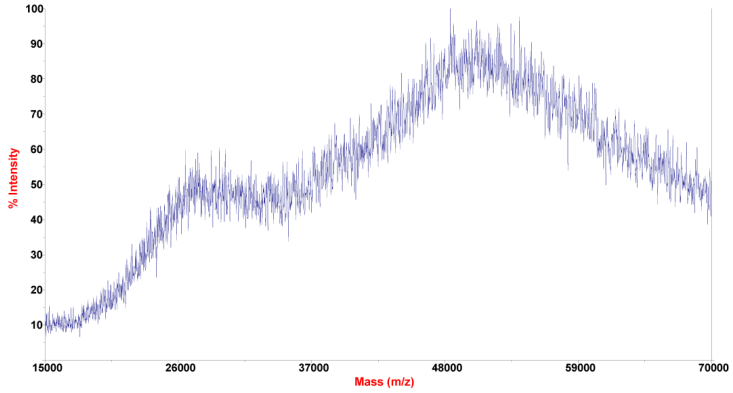

Figure S4.8. MALDI-TOF MS spectrum of **GdD[1]-mPEG** (THAP matrix).

6.7 Appendix D

6.8 Experimental Section

6.8.1 Materials and Methods

For materials and methods, see Chapter 2.

6.8.2 NMR titrations

NMR experiments were performed at 25°C at 300 MHz (^{13}C at 75 MHz). Samples were placed in the outer NMR tube equipped with the coaxial insert filled with D_2O with DSS as the reference. Titration of **LnL^5/YL^5** solutions (concentrations are indicated in the respective experiment) was performed by the addition of a buffered solution of ^{13}C-labeled Glu or Gly, and the ^{13}C NMR spectra were recorded upon each addition. The pH value was maintained at 7.4 by the addition of diluted aqueous solutions of HCl and KOH and measured with a standard pH glass electrode.

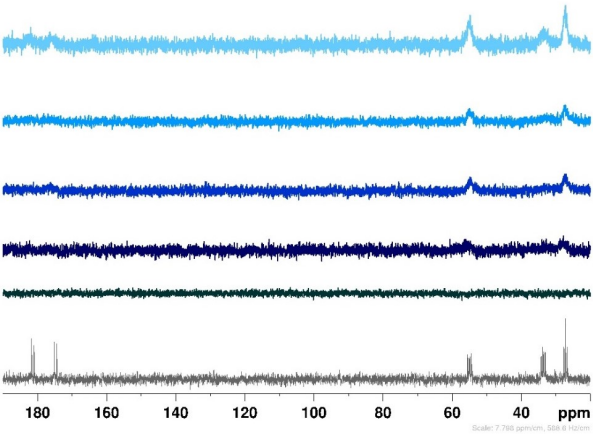

Figure S5.1. ^{13}C NMR of Glu induced in the presence of **EuL^5**. 10 mM **EuL^5** in the presence of 10, 20, 30, 40, and 50 equiv. of Glu at 300 MHz (H_2O, pH 7.4, 25°C, D_2O).

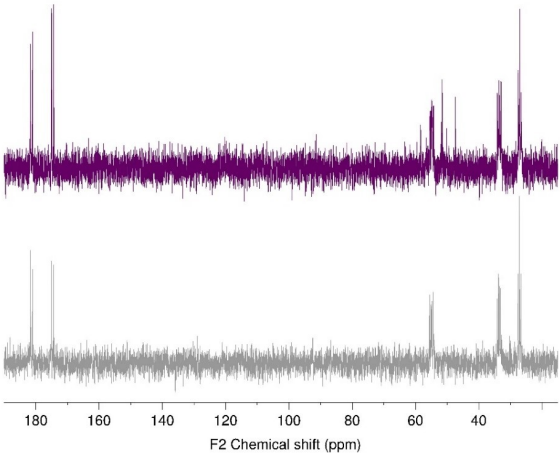

Figure S5.2. ^{13}C NMR spectra of Glu in the absence (gray) and presence (purple) of **YL^5**.

Bibliography

1. Glaser, S., *Magn. Reson. Chem.* **2000,** *38* (11), 985-985.
2. Doan, B.-T.; Meme, S.; Beloeil, J.-C.
3. Brown, M.; Semelka, R.; Nishino, T. K., *Medical Physics* **2004,** *31* (1), 170-170.
4. Caravan, P.; Farrar, C. T.; Frullano, L.; Uppal, R., *Contrast Media & Molecular Imaging* **2009,** *4* (2), 89-100.
5. Yang, C.; Tian, R.; Liu, T.; Liu, G., *Molecules* **2016,** *21* (5), 580.
6. Korngold, E. C.; Jaffer, F. A.; Weissleder, R.; Sosnovik, D. E., *Heart Failure Reviews* **2008,** *13* (2), 163-173.
7. Zhang, F.; Xie, J.; Liu, G.; He, Y.; Lu, G.; Chen, X., *Molecular Imaging and Biology* **2011,** *13* (4), 695-701.
8. Barandov, A.; Bartelle, B. B.; Williamson, C. G.; Loucks, E. S.; Lippard, S. J.; Jasanoff, A., *Nature Communications* **2019,** *10* (1), 897.
9. Bloch, F.; Hansen, W. W.; Packard, M., *Physical Review* **1946,** *69* (3-4), 127-127.
10. Purcell, E. M.; Torrey, H. C.; Pound, R. V., *Physical Review* **1946,** *69* (1-2), 37-38.
11. *American Journal of Neuroradiology* **2008,** *29* (6), e50.
12. Nelson, K. L.; Runge, V. M., *Topics in magnetic resonance imaging : TMRI* **1995,** *7* (3), 124-36.
13. Wood, M. L.; Hardy, P. A., *Journal of magnetic resonance imaging : JMRI* **1993,** *3* (1), 149-56.
14. Hancu, I.; Dixon, W. T.; Woods, M.; Vinogradov, E.; Sherry, A. D.; Lenkinski, R. E., *Acta Radiol* **2010,** *51* (8), 910-923.
15. Hendrick, R. E.; Mark Haacke, E., *Journal of Magnetic Resonance Imaging* **1993,** *3* (1), 137-148.
16. Geraldes, C. F. G. C.; Laurent, S., *Contrast Media & Molecular Imaging* **2009,** *4* (1), 1-23.
17. Bony, B. A.; Baeck, J. S.; Chang, Y.; Bae, J. E.; Chae, K. S.; Lee, G. H., *Bull. Korean Chem. Soc.* **2015,** *36* (4), 1203-1208.
18. Kalavagunta, C.; Michaeli, S.; Metzger, G. J., *Contrast Media & Molecular Imaging* **2014,** *9* (2), 169-176.
19. Wong, W.; Chan, K. W.
20. Caravan, P.; Ellison, J. J.; McMurry, T. J.; Lauffer, R. B., *Chem. Rev.* **1999,** *99* (9), 2293-352.
21. Port, M.; Idée, J.-M.; Medina, C.; Robic, C.; Sabatou, M.; Corot, C., *BioMetals* **2008,** *21* (4), 469-490.
22. Bourne, G. W.; Trifaró, J. M., *Neuroscience* **1982,** *7* (7), 1615-1622.
23. Spencer, A.; Wilson, S.; Harpur, E., *Human & experimental toxicology* **1998,** *17* (11), 633-7.
24. Corot, C.; Idee, J. M.; Hentsch, A. M.; Santus, R.; Mallet, C.; Goulas, V.; Bonnemain, B.; Meyer, D., *Journal of magnetic resonance imaging : JMRI* **1998,** *8* (3), 695-702.
25. Morcos, S. K., *European journal of radiology* **2008,** *66* (2), 175-9.
26. Schmitt-Willich, H., *The British Journal of Radiology* **2007,** *80* (955), 581-582.
27. Chen, Y.-M.; Wang, C.-Z.; Wu, Q.-Y.; Lan, J.-H.; Chai, Z.-F.; Nie, C.-M.; Shi, W.-Q., *J. Mol. Liq.* **2020,** *299*, 112174.
28. Gustav, J. S.; Willem, J. M. M.; Geralda, A. F. v. T.; Klaas, N., *Anti-Cancer Agents in Medicinal Chemistry* **2007,** *7* (3), 291-305.
29. Taeko, I.; Tabassum, M.; Robia, G. P., *Reviews in the Neurosciences* **2011,** *22* (6), 675-694.
30. Eschenko, O.; Evrard, H. C.; Neves, R. M.; Beyerlein, M.; Murayama, Y.; Logothetis, N. K., *NeuroImage* **2012,** *59* (4), 3252-3265.
31. Small, W. C.; Macchi, D. D.; Parker, J. R.; Bernardino, M. E., *Academic radiology* **1998,** *5 Suppl 1*, S147-50; discussion S156.
32. Rivera-Mancía, S.; Ríos, C.; Montes, S., *BioMetals* **2011,** *24* (5), 811-825.
33. Gallez, B.; Demeure, R.; Baudelet, C.; Abdelouahab, N.; Beghein, N.; Jordan, B.; Geurts, M.; Roels, H. A., *NeuroToxicology* **2001,** *22* (3), 387-392.
34. Pan, D.; Schmieder, A. H.; Wickline, S. A.; Lanza, G. M., *Tetrahedron* **2011,** *67* (44), 8431-8444.
35. Karlsson, J. O. G.; Ignarro, L. J.; Lundström, I.; Jynge, P.; Almén, T., *Drug Discovery Today* **2015,** *20* (4), 411-421.
36. Toft, K. G.; Hustvedt, S. O.; Grant, D.; Martinsen, I.; Gordon, P. B.; Friisk, G. A.; Korsmo, A. J.; Skotland, T., *Acta radiologica (Stockholm, Sweden : 1987)* **1997,** *38* (4 Pt 2), 677-89.
37. Gale, E. M.; Atanasova, I. P.; Blasi, F.; Ay, I.; Caravan, P., *J. Am. Chem. Soc.* **2015,** *137* (49), 15548-15557.
38. Baker, J. F.; Kratz, L. C.; Stevens, G. R.; Wible, J. H., Jr., *Investigative radiology* **2004,** *39* (6), 334-9.

39. Oliveira, I. S.; Hedgire, S. S.; Li, W.; Ganguli, S.; Prabhakar, A. M., *Cardiovasc Diagn Ther* **2016,** *6* (6), 508-518.
40. Mahfouz, A. E., *Curr Opin Investig Drugs* **2000,** *1* (4), 476-480.
41. Grobner, T., *Nephrology, dialysis, transplantation : official publication of the European Dialysis and Transplant Association - European Renal Association* **2006,** *21* (4), 1104-8.
42. Marckmann, P.; Skov, L.; Rossen, K.; Dupont, A.; Damholt, M. B.; Heaf, J. G.; Thomsen, H. S., *Journal of the American Society of Nephrology : JASN* **2006,** *17* (9), 2359-62.
43. Runge, V. M., *Journal of magnetic resonance imaging : JMRI* **2000,** *12* (2), 205-13.
44. Guo, B. J.; Yang, Z. L.; Zhang, L. J., *Front Mol Neurosci* **2018,** *11*, 335-335.
45. Montagne, A.; Toga, A. W.; Zlokovic, B. V., *JAMA Neurol* **2016,** *73* (1), 13-14.
46. Nehra, A. K.; McDonald, R. J.; Bluhm, A. M.; Gunderson, T. M.; Murray, D. L.; Jannetto, P. J.; Kallmes, D. F.; Eckel, L. J.; McDonald, J. S., *Radiology* **2018,** *288* (2), 416-423.
47. Kanda, T.; Nakai, Y.; Oba, H.; Toyoda, K.; Kitajima, K.; Furui, S., *Magn Reson Imaging* **2016,** *34* (10), 1346-1350.
48. Taoka, T.; Naganawa, S., *Magn Reson Med Sci* **2018,** *17* (2), 111-119.
49. Vergauwen, E.; Vanbinst, A.-M.; Brussaard, C.; Janssens, P.; De Clerck, D.; Van Lint, M.; Houtman, A. C.; Michel, O.; Keymolen, K.; Lefevere, B.; Bohler, S.; Michielsen, D.; Jansen, A. C.; Van Velthoven, V.; Gläsker, S., *Hered Cancer Clin Pract* **2018,** *16*, 2-2.
50. Park, J. Y.; Choi, E. S.; Baek, M. J.; Lee, G. H.; Woo, S.; Chang, Y., *Eur. J. Inorg. Chem.* **2009,** *2009* (17), 2477-2481.
51. Qin, J.; Laurent, S.; Jo, Y. S.; Roch, A.; Mikhaylova, M.; Bhujwalla, Z. M.; Muller, R. N.; Muhammed, M., *Adv. Mater.* **2007,** *19* (14), 1874-1878.
52. Karimzadeh, I.; Aghazadeh, M.; Doroudi, T.; Ganjali, M. R.; Kolivand, P. H., *Advances in Physical Chemistry* **2017,** *2017*, 9437487.
53. Maurizi, L.; Claveau, A.; Hofmann, H., *Journal of Nanomaterials* **2015,** *2015*, 732719.
54. Karimzadeh, I.; Dizaji, H. R.; Aghazadeh, M., *J. Magn. Magn. Mater.* **2016,** *416*, 81-88.
55. Bohara, R. A.; Thorat, N. D.; Pawar, S. H., *RSC Advances* **2016,** *6* (50), 43989-44012.
56. Storey, P.; Lim, R. P.; Chandarana, H.; Rosenkrantz, A. B.; Kim, D.; Stoffel, D. R.; Lee, V. S., *Investigative radiology* **2012,** *47* (12), 717-24.
57. Maurizi, L.; Papa, A.-L.; Dumont, L.; Bouyer, F.; Walker, P.; Vandroux, D.; Millot, N., *Journal of Biomedical Nanotechnology* **2015,** *11* (1), 126-136.
58. Mornet, S.; Vasseur, S.; Grasset, F.; Duguet, E., *J. Mater. Chem.* **2004,** *14* (14), 2161-2175.
59. Hamm, B., *European Radiology* **2002,** *12* (5), 957-958.
60. Maeda, H.; Wu, J.; Sawa, T.; Matsumura, Y.; Hori, K., *J. Controlled Release* **2000,** *65* (1), 271-284.
61. Golombek, S. K.; May, J. N.; Theek, B.; Appold, L.; Drude, N.; Kiessling, F.; Lammers, T., *Advanced drug delivery reviews* **2018,** *130*, 17-38.
62. Xie, J.; Chen, K.; Lee, H.-Y.; Xu, C.; Hsu, A. R.; Peng, S.; Chen, X.; Sun, S., *J. Am. Chem. Soc.* **2008,** *130* (24), 7542-7543.
63. Cohen, B.; Dafni, H.; Meir, G.; Harmelin, A.; Neeman, M., *Neoplasia* **2005,** *7* (2), 109-117.
64. Leuze, C.; Aswendt, M.; Ferenczi, E.; Liu, C. W.; Hsueh, B.; Goubran, M.; Tian, Q.; Steinberg, G.; Zeineh, M. M.; Deisseroth, K.; McNab, J. A., *NeuroImage* **2017,** *156*, 412-422.
65. Brooks, R. A.; Vymazal, J.; Bulte, J. W.; Baumgarner, C. D.; Tran, V., *J Magn Reson Imaging* **1995,** *5* (4), 446-450.
66. Rooney, W. D.; Johnson, G.; Li, X.; Cohen, E. R.; Kim, S. G.; Ugurbil, K.; Springer, C. S., Jr., *Magnetic resonance in medicine* **2007,** *57* (2), 308-18.
67. Tóth, é.; Helm, L.; Merbach, A.
68. De León-Rodríguez, L. M.; Martins, A. F.; Pinho, M. C.; Rofsky, N. M.; Sherry, A. D., *Journal of Magnetic Resonance Imaging* **2015,** *42* (3), 545-565.
69. Luz, Z.; Meiboom, S., *The Journal of Chemical Physics* **1964,** *40* (9), 2686-2692.
70. Swift, T. J.; Connick, R. E., *The Journal of Chemical Physics* **1962,** *37* (2), 307-320.
71. Solomon, I., *Physical Review* **1955,** *99* (2), 559-565.
72. Bloembergen, N.; Purcell, E. M.; Pound, R. V., *Physical Review* **1948,** *73* (7), 679-712.
73. Yazyev, O. V.; Helm, L.; Malkin, V. G.; Malkina, O. L., *The Journal of Physical Chemistry A* **2005,** *109* (48), 10997-11005.
74. Tóth, É.; Helm, L.; Merbach, A. E., Relaxivity of MRI Contrast Agents. In *Contrast Agents I: Magnetic Resonance Imaging*, Krause, W., Ed. Springer Berlin Heidelberg: Berlin, Heidelberg, 2002; pp 61-101.
75. Benmelouka, M.; Borel, A.; Moriggi, L.; Helm, L.; Merbach, A. E., *The Journal of Physical Chemistry B* **2007,** *111* (4), 832-840.

76. Bloembergen, N.; Morgan, L. O., *The Journal of Chemical Physics* **1961,** *34* (3), 842-850.
77. Hwang, L. P.; Freed, J. H., *The Journal of Chemical Physics* **1975,** *63* (9), 4017-4025.
78. Freed, J. H., *The Journal of Chemical Physics* **1978,** *68* (9), 4034-4037.
79. Kotková, Z.; Pereira, G. A.; Djanashvili, K.; Kotek, J.; Rudovský, J.; Hermann, P.; Vander Elst, L.; Muller, R. N.; Geraldes, C. F. G. C.; Lukeš, I.; Peters, J. A., *Eur. J. Inorg. Chem.* **2009,** *2009* (1), 119-136.
80. Lauffer, R. B., *Chem. Rev.* **1987,** *87* (5), 901-927.
81. Botta, M., *Eur. J. Inorg. Chem.* **2000,** *2000* (3), 399-407.
82. Jacques, V.; Dumas, S.; Sun, W.-C.; Troughton, J. S.; Greenfield, M. T.; Caravan, P., *Invest Radiol* **2010,** *45* (10), 613-624.
83. Aime, S.; Botta, M.; Frullano, L.; Geninatti Crich, S.; Giovenzana, G.; Pagliarin, R.; Palmisano, G.; Sirtori, F. R.; Sisti, M., *J. Med. Chem.* **2000,** *43* (21), 4017-4024.
84. Baranyai, Z.; Gianolio, E.; Ramalingam, K.; Swenson, R.; Ranganathan, R.; Brücher, E.; Aime, S., *Contrast Media & Molecular Imaging* **2007,** *2* (2), 94-102.
85. Caravan, P.; Greenfield, M. T.; Li, X.; Sherry, A. D., *Inorg. Chem.* **2001,** *40* (26), 6580-6587.
86. Congreve, A.; Parker, D.; Gianolio, E.; Botta, M., *Dalton Transactions* **2004,** (9), 1441-1445.
87. Tweedle, M. F.; Hagan, J. J.; Kumar, K.; Mantha, S.; Chang, C. A., *Magnetic Resonance Imaging* **1991,** *9* (3), 409-415.
88. Gale, E. M.; Caravan, P.; Rao, A. G.; McDonald, R. J.; Winfeld, M.; Fleck, R. J.; Gee, M. S., *Pediatric Radiology* **2017,** *47* (5), 507-521.
89. Moreau, J.; Guillon, E.; Pierrard, J.-C.; Rimbault, J.; Port, M.; Aplincourt, M., *Chemistry – A European Journal* **2004,** *10* (20), 5218-5232.
90. Supkowski, R. M.; Horrocks, W. D., Jr., *Inorg. Chem.* **1999,** *38* (24), 5616-5619.
91. Aime, S.; Botta, M.; Crich, S. G.; Giovenzana, G.; Pagliarin, R.; Sisti, M.; Terreno, E., *Magn. Reson. Chem.* **1998,** *36* (S1), S200-S208.
92. Tircsó, G.; Kovács, Z.; Sherry, A. D., *Inorg. Chem.* **2006,** *45* (23), 9269-9280.
93. Aime, S.; Calabi, L.; Cavallotti, C.; Gianolio, E.; Giovenzana, G. B.; Losi, P.; Maiocchi, A.; Palmisano, G.; Sisti, M., *Inorg. Chem.* **2004,** *43* (24), 7588-7590.
94. Datta, A.; Raymond, K. N., *Acc. Chem. Res.* **2009,** *42* (7), 938-947.
95. Doble, D. M. J.; Melchior, M.; O'Sullivan, B.; Siering, C.; Xu, J.; Pierre, V. C.; Raymond, K. N., *Inorg. Chem.* **2003,** *42* (16), 4930-4937.
96. Werner, E. J.; Avedano, S.; Botta, M.; Hay, B. P.; Moore, E. G.; Aime, S.; Raymond, K. N., *J. Am. Chem. Soc.* **2007,** *129* (7), 1870-1871.
97. Dickins, R. S.; Parker, D.; de Sousa, A. S.; Williams, J. A. G., *Chem. Commun.* **1996,** (6), 697-698.
98. Beeby, A.; M. Clarkson, I.; S. Dickins, R.; Faulkner, S.; Parker, D.; Royle, L.; S. de Sousa, A.; A. Gareth Williams, J.; Woods, M., *Journal of the Chemical Society, Perkin Transactions 2* **1999,** (3), 493-504.
99. Djanashvili, K.; Peters, J. A., *Contrast Media & Molecular Imaging* **2007,** *2* (2), 67-71.
100. Zech, S. G.; Sun, W.-C.; Jacques, V.; Caravan, P.; Astashkin, A. V.; Raitsimring, A. M., *ChemPhysChem* **2005,** *6* (12), 2570-2577.
101. Raitsimring, A. M.; Astashkin, A. V.; Baute, D.; Goldfarb, D.; Poluektov, O. G.; Lowe, M. P.; Zech, S. G.; Caravan, P., *ChemPhysChem* **2006,** *7* (7), 1590-1597.
102. Pubanz, D.; Gonzalez, G.; Powell, D. H.; Merbach, A. E., *Inorg. Chem.* **1995,** *34* (17), 4447-4453.
103. Graeppi, N.; Hugh Powell, D.; Laurenczy, G.; Zékány, L.; Merbach, A., *Inorg. Chim. Acta* **1995,** *235* (1), 311-326.
104. Jászberényi, Z.; Sour, A.; Tóth, E.; Benmelouka, M.; Merbach, A. E., *Dalton transactions (Cambridge, England : 2003)* **2005,** (16), 2713-9.
105. Aime, S.; Botta, M.; Ermondi, G., *Inorg. Chem.* **1992,** *31* (21), 4291-4299.
106. Hoeft, S.; Roth, K., *Chem. Ber.* **1993,** *126* (4), 869-873.
107. Aime, S.; Botta, M.; Garda, Z.; Kucera, B. E.; Tircso, G.; Young, V. G.; Woods, M., *Inorg. Chem.* **2011,** *50* (17), 7955-7965.
108. Hancu, I.; Dixon, W. T.; Woods, M.; Vinogradov, E.; Sherry, A. D.; Lenkinski, R. E., *Acta Radiologica* **2010,** *51* (8), 910-923.
109. Zhang, S.; Kovacs, Z.; Burgess, S.; Aime, S.; Terreno, E.; Sherry, A. D., *Chemistry (Weinheim an der Bergstrasse, Germany)* **2001,** *7* (1), 288-96.
110. Aime, S.; Barge, A.; Bruce, J. I.; Botta, M.; Howard, J. A. K.; Moloney, J. M.; Parker, D.; de Sousa, A. S.; Woods, M., *J. Am. Chem. Soc.* **1999,** *121* (24), 5762-5771.
111. Ratnakar, S. J.; Woods, M.; Lubag, A. J. M.; Kovács, Z.; Sherry, A. D., *J. Am. Chem. Soc.* **2008,** *130* (1), 6-7.

112. Micskei, K.; Helm, L.; Brucher, E.; Merbach, A. E., *Inorg. Chem.* **1993,** *32* (18), 3844-3850.
113. Gonzalez, G.; Powell, D. H.; Tissieres, V.; Merbach, A. E., *The Journal of Physical Chemistry* **1994,** *98* (1), 53-59.
114. Valencia, D. P.; González, F. J., *Electrochem. Commun.* **2011,** *13* (2), 129-132.
115. Bryant, L. H., Jr.; Brechbiel, M. W.; Wu, C.; Bulte, J. W.; Herynek, V.; Frank, J. A., *Journal of magnetic resonance imaging : JMRI* **1999,** *9* (2), 348-52.
116. Song, Y.; Xu, X.; MacRenaris, K. W.; Zhang, X.-Q.; Mirkin, C. A.; Meade, T. J., *Angew. Chem. Int. Ed.* **2009,** *48* (48), 9143-9147.
117. Venditto, V. J.; Regino, C. A. S.; Brechbiel, M. W., *Molecular Pharmaceutics* **2005,** *2* (4), 302-311.
118. Livramento, J. B.; Tóth, É.; Sour, A.; Borel, A.; Merbach, A. E.; Ruloff, R., *Angew. Chem. Int. Ed.* **2005,** *44* (10), 1480-1484.
119. Barkey, N. M.; Preihs, C.; Cornnell, H. H.; Martinez, G.; Carie, A.; Vagner, J.; Xu, L.; Lloyd, M. C.; Lynch, V. M.; Hruby, V. J.; Sessler, J. L.; Sill, K. N.; Gillies, R. J.; Morse, D. L., *J. Med. Chem.* **2013,** *56* (16), 6330-6338.
120. Smith, C. E.; Shkumatov, A.; Withers, S. G.; Yang, B.; Glockner, J. F.; Misra, S.; Roy, E. J.; Wong, C.-H.; Zimmerman, S. C.; Kong, H., *ACS Nano* **2013,** *7* (11), 9599-9610.
121. Mastarone, D. J.; Harrison, V. S. R.; Eckermann, A. L.; Parigi, G.; Luchinat, C.; Meade, T. J., *J. Am. Chem. Soc.* **2011,** *133* (14), 5329-5337.
122. Fulton, D. A.; Elemento, E. M.; Aime, S.; Chaabane, L.; Botta, M.; Parker, D., *Chem. Commun.* **2006,** (10), 1064-1066.
123. Wiener, E. C.; Auteri, F. P.; Chen, J. W.; Brechbiel, M. W.; Gansow, O. A.; Schneider, D. S.; Belford, R. L.; Clarkson, R. B.; Lauterbur, P. C., *J. Am. Chem. Soc.* **1996,** *118* (33), 7774-7782.
124. Zhang, Z.; Greenfield, M. T.; Spiller, M.; McMurry, T. J.; Lauffer, R. B.; Caravan, P., *Angew. Chem. Int. Ed.* **2005,** *44* (41), 6766-6769.
125. Boros, E.; Srinivas, R.; Kim, H.-K.; Raitsimring, A. M.; Astashkin, A. V.; Poluektov, O. G.; Niklas, J.; Horning, A. D.; Tidor, B.; Caravan, P., *Angew. Chem. Int. Ed.* **2017,** *56* (20), 5603-5606.
126. Caravan, P.; Cloutier, N. J.; Greenfield, M. T.; McDermid, S. A.; Dunham, S. U.; Bulte, J. W. M.; Amedio, J. C.; Looby, R. J.; Supkowski, R. M.; Horrocks, W. D.; McMurry, T. J.; Lauffer, R. B., *J. Am. Chem. Soc.* **2002,** *124* (12), 3152-3162.
127. Wallace, R. A.; Haar Jr, J. P.; Miller, D. B.; Woulfe, S. R.; Polta, J. A.; Galen, K. P.; Hynes, M. R.; Adzamli, K., *Magnetic Resonance in Medicine* **1998,** *40* (5), 733-739.
128. Strauch, R. C.; Mastarone, D. J.; Sukerkar, P. A.; Song, Y.; Ipsaro, J. J.; Meade, T. J., *J. Am. Chem. Soc.* **2011,** *133* (41), 16346-16349.
129. Pierre, V. C.; Harris, S. M.; Pailloux, S. L., *Acc. Chem. Res.* **2018,** *51* (2), 342-351.
130. Zhang, L.; Li, J.; Liu, K., *Science China Technological Sciences* **2018,** *61* (9), 1329-1333.
131. Hingorani, D. V.; Bernstein, A. S.; Pagel, M. D., *Contrast Media & Molecular Imaging* **2015,** *10* (4), 245-265.
132. Moats, R. A.; Fraser, S. E.; Meade, T. J., *Angewandte Chemie International Edition in English* **1997,** *36* (7), 726-728.
133. André, J. P.; Tóth, É.; Fischer, H.; Seelig, A.; Mäcke, H. R.; Merbach, A. E., *Chemistry – A European Journal* **1999,** *5* (10), 2977-2983.
134. Aime, S.; Botta, M.; Frullano, L.; Crich, S. G.; Giovenzana, G. B.; Pagliarin, R.; Palmisano, G.; Sisti, M., *Chemistry – A European Journal* **1999,** *5* (4), 1253-1260.
135. Aime, S.; Botta, M.; Panero, M.; Grandi, M.; Uggeri, F., *Magn. Reson. Chem.* **1991,** *29* (9), 923-927.
136. Parac-Vogt, T. N.; Vander Elst, L.; Kimpe, K.; Laurent, S.; Burtéa, C.; Chen, F.; Van Deun, R.; Ni, Y.; Muller, R. N.; Binnemans, K., *Contrast Media & Molecular Imaging* **2006,** *1* (6), 267-278.
137. Ye, D.; Pandit, P.; Kempen, P.; Lin, J.; Xiong, L.; Sinclair, R.; Rutt, B.; Rao, J., *Bioconjugate Chem.* **2014,** *25* (8), 1526-1536.
138. Lebel, R.; Jastrzębska, B.; Therriault, H.; Cournoyer, M.-M.; McIntyre, J. O.; Escher, E.; Neugebauer, W.; Paquette, B.; Lepage, M., *Magnetic Resonance in Medicine* **2008,** *60* (5), 1056-1065.
139. Catanzaro, V.; Gringeri, C. V.; Menchise, V.; Padovan, S.; Boffa, C.; Dastrù, W.; Chaabane, L.; Digilio, G.; Aime, S., *Angew. Chem. Int. Ed.* **2013,** *52* (14), 3926-3930.
140. Ekanger, L. A.; Allen, M. J., *Metallomics* **2015,** *7* (3), 405-421.
141. Aime, S.; Fedeli, F.; Sanino, A.; Terreno, E., *J. Am. Chem. Soc.* **2006,** *128* (35), 11326-11327.
142. Aime, S.; Geninatti Crich, S.; Botta, M.; Giovenzana, G.; Palmisano, G.; Sisti, M., *Chem. Commun.* **1999,** (16), 1577-1578.
143. Tu, C.; Louie, A. Y., *NMR Biomed.* **2013,** *26* (7), 781-787.

144. Botár, R.; Molnár, E.; Trencsényi, G.; Kiss, J.; Kálmán, F. K.; Tircsó, G., *J. Am. Chem. Soc.* **2020,** *142* (4), 1662-1666.
145. Li, W.-h.; Fraser, S. E.; Meade, T. J., *J. Am. Chem. Soc.* **1999,** *121* (6), 1413-1414.
146. MacRenaris, K. W.; Ma, Z.; Krueger, R. L.; Carney, C. E.; Meade, T. J., *Bioconjugate Chem.* **2016,** *27* (2), 465-473.
147. Li, W.-h.; Parigi, G.; Fragai, M.; Luchinat, C.; Meade, T. J., *Inorg. Chem.* **2002,** *41* (15), 4018-4024.
148. Mishra, A.; Fousková, P.; Angelovski, G.; Balogh, E.; Mishra, A. K.; Logothetis, N. K.; Tóth, É., *Inorg. Chem.* **2008,** *47* (4), 1370-1381.
149. Angelovski, G.; Fouskova, P.; Mamedov, I.; Canals, S.; Toth, E.; Logothetis, N. K., *ChemBioChem* **2008,** *9* (11), 1729-1734.
150. Que, E. L.; Gianolio, E.; Baker, S. L.; Wong, A. P.; Aime, S.; Chang, C. J., *J. Am. Chem. Soc.* **2009,** *131* (24), 8527-8536.
151. Hanaoka, K.; Kikuchi, K.; Urano, Y.; Narazaki, M.; Yokawa, T.; Sakamoto, S.; Yamaguchi, K.; Nagano, T., *Chemistry & Biology* **2002,** *9* (9), 1027-1032.
152. Oukhatar, F.; Même S Fau - Même, W.; Même W Fau - Szeremeta, F.; Szeremeta F Fau - Logothetis, N. K.; Logothetis Nk Fau - Angelovski, G.; Angelovski G Fau - Tóth, É.; Tóth, É., (1948-7193 (Electronic)).
153. Oukhatar, F.; Meudal, H.; Landon, C.; Logothetis, N. K.; Platas-Iglesias, C.; Angelovski, G.; Tóth, É., (1521-3765 (Electronic)).
154. Lee, T.; Cai, L. X.; Lelyveld, V. S.; Hai, A.; Jasanoff, A., *Science* **2014,** *344* (6183), 533.
155. Shapiro, M. G.; Westmeyer, G. G.; Romero, P. A.; Szablowski, J. O.; Küster, B.; Shah, A.; Otey, C. R.; Langer, R.; Arnold, F. H.; Jasanoff, A., *Nat. Biotechnol.* **2010,** *28* (3), 264-270.
156. Matsumoto, Y.; Jasanoff, A., *FEBS Lett.* **2013,** *587* (8), 1021-1029.
157. Luo, Y.; Kim, E. H.; Flask, C. A.; Clark, H. A., *ACS Nano* **2018,** *12* (6), 5761-5773.
158. Giraudeau, C.; Flament, J.; Marty, B.; Boumezbeur, F.; Mériaux, S.; Robic, C.; Port, M.; Tsapis, N.; Fattal, E.; Giacomini, E.; Lethimonnier, F.; Le Bihan, D.; Valette, J., *Magnetic Resonance in Medicine* **2010,** *63* (4), 1119-1124.
159. Peterson, K. L.; Srivastava, K.; Pierre, V. C., *Frontiers in Chemistry* **2018,** *6*, 160.
160. Yu, J.-X.; Kodibagkar, V. D.; Hallac, R. R.; Liu, L.; Mason, R. P., *Bioconjugate Chem.* **2012,** *23* (3), 596-603.
161. Sakamoto, T.; Shimizu, Y.-k.; Sasaki, J.; Hayakawa, H.; Fujimoto, K., *Bioorg. Med. Chem. Lett.* **2011,** *21* (1), 303-306.
162. Lindon, J. C., Nuclear Magnetic Resonance Spectroscopy | Fluorine-19☆. In *Encyclopedia of Analytical Science (Third Edition)*, Worsfold, P.; Poole, C.; Townshend, A.; Miró, M., Eds. Academic Press: Oxford, 2016; pp 141-151.
163. Kenwright, A. M.; Kuprov, I.; De Luca, E.; Parker, D.; Pandya, S. U.; Senanayake, P. K.; Smith, D. G., *Chem. Commun.* **2008,** (22), 2514-2516.
164. Harvey, P.; Chalmers, K. H.; De Luca, E.; Mishra, A.; Parker, D., *Chemistry – A European Journal* **2012,** *18* (28), 8748-8757.
165. Blackburn, O. A.; Chilton, N. F.; Keller, K.; Tait, C. E.; Myers, W. K.; McInnes, E. J. L.; Kenwright, A. M.; Beer, P. D.; Timmel, C. R.; Faulkner, S., *Angew Chem Weinheim Bergstr Ger* **2015,** *127* (37), 10933-10936.
166. Tsitovich, P. B.; Spernyak, J. A.; Morrow, J. R., *Angew. Chem. Int. Ed.* **2013,** *52* (52), 13997-14000.
167. Ratnakar, S. J.; Viswanathan, S.; Kovacs, Z.; Jindal, A. K.; Green, K. N.; Sherry, A. D., *J. Am. Chem. Soc.* **2012,** *134* (13), 5798-5800.
168. Delli Castelli, D.; Gianolio, E.; Geninatti Crich, S.; Terreno, E.; Aime, S., *Coord. Chem. Rev.* **2008,** *252* (21), 2424-2443.
169. Terreno, E.; Boffa, C.; Menchise, V.; Fedeli, F.; Carrera, C.; Castelli, D. D.; Digilio, G.; Aime, S., *Chem. Commun.* **2011,** *47* (16), 4667-4669.
170. Schröder, L.; Lowery, T. J.; Hilty, C.; Wemmer, D. E.; Pines, A., *Science* **2006,** *314* (5798), 446.
171. Khan, N. S.; Riggle, B. A.; Seward, G. K.; Bai, Y.; Dmochowski, I. J., *Bioconjugate Chem.* **2015,** *26* (1), 101-109.
172. Kim, B. S.; Ko, Y. H.; Kim, Y.; Lee, H. J.; Selvapalam, N.; Lee, H. C.; Kim, K., *Chem. Commun.* **2008,** (24), 2756-2758.
173. Shapiro, M. G.; Ramirez, R. M.; Sperling, L. J.; Sun, G.; Sun, J.; Pines, A.; Schaffer, D. V.; Bajaj, V. S., *Nature Chemistry* **2014,** *6* (7), 629-634.
174. Stevens, T. K.; Ramirez, R. M.; Pines, A., *J. Am. Chem. Soc.* **2013,** *135* (26), 9576-9579.
175. Roukala, J.; Zhu, J.; Giri, C.; Rissanen, K.; Lantto, P.; Telkki, V.-V., *J. Am. Chem. Soc.* **2015,** *137* (7), 2464-2467.

176. Jayapaul, J.; Schröder, L., *Contrast Media & Molecular Imaging* **2019,** *2019*, 9498173.
177. Rose, H. M.; Witte, C.; Rossella, F.; Klippel, S.; Freund, C.; Schröder, L., *Proceedings of the National Academy of Sciences* **2014,** *111* (32), 11697.
178. Kunth, M.; Witte, C.; Hennig, A.; Schröder, L., *Chemical Science* **2015,** *6* (11), 6069-6075.
179. Slack, C. C.; Finbloom, J. A.; Jeong, K.; Bruns, C. J.; Wemmer, D. E.; Pines, A.; Francis, M. B., *Chem. Commun.* **2017,** *53* (6), 1076-1079.
180. Mishra, A.; Pariani, G.; Oerther, T.; Schwaiger, M.; Westmeyer, G. G., *Anal. Chem.* **2016,** *88* (22), 10790-10794.
181. El Alaoui El Abdallaoui, H.; Champmartin, D.; Rubini, P., *J. Chem. Soc., Dalton Trans.* **2001,** (14), 2153-2156.
182. Nonaka, H.; Hata, R.; Doura, T.; Nishihara, T.; Kumagai, K.; Akakabe, M.; Tsuda, M.; Ichikawa, K.; Sando, S., *Nature Communications* **2013,** *4* (1), 2411.
183. Jindal, A. K.; Merritt, M. E.; Suh, E. H.; Malloy, C. R.; Sherry, A. D.; Kovács, Z., *J. Am. Chem. Soc.* **2010,** *132* (6), 1784-1785.
184. Abbasi, E.; Aval, S. F.; Akbarzadeh, A.; Milani, M.; Nasrabadi, H. T.; Joo, S. W.; Hanifehpour, Y.; Nejati-Koshki, K.; Pashaei-Asl, R., *Nanoscale Research Letters* **2014,** *9* (1), 247.
185. Tomalia, D. A.; Baker, H.; Dewald, J.; Hall, M.; Kallos, G.; Martin, S.; Roeck, J.; Ryder, J.; Smith, P., *Polym. J.* **1985,** *17* (1), 117-132.
186. Leclaire, J.; Dagiral, R.; Fery-Forgues, S.; Coppel, Y.; Donnadieu, B.; Caminade, A.-M.; Majoral, J.-P., *J. Am. Chem. Soc.* **2005,** *127* (45), 15762-15770.
187. McClenaghan, N. D.; Passalacqua, R.; Loiseau, F.; Campagna, S.; Verheyde, B.; Hameurlaine, A.; Dehaen, W., *J. Am. Chem. Soc.* **2003,** *125* (18), 5356-5365.
188. Saudan, C.; Balzani, V.; Gorka, M.; Lee, S.-K.; Maestri, M.; Vicinelli, V.; Vögtle, F., *J. Am. Chem. Soc.* **2003,** *125* (15), 4424-4425.
189. Gürbüz, M. U.; Öztürk, K.; Ertürk, A. S.; Yoyen-Ermis, D.; Esendagli, G.; Çalış, S.; Tülü, M., *Journal of Biomaterials Science, Polymer Edition* **2016,** *27* (16), 1645-1658.
190. Gopidas, K. R.; Whitesell, J. K.; Fox, M. A., *J. Am. Chem. Soc.* **2003,** *125* (46), 14168-14180.
191. Nikolskaya, E.; Yabbarov, N.; Zhunina, O.; Tereshenko, O.; Mollaev, M.; Faustova, M.; Zamulaeva, I.; Séverin, E., *Materials Today: Proceedings* **2017,** *4*, 6849-6855.
192. Rippe, C.; Asgeirsson, D.; Venturoli, D.; Rippe, A.; Rippe, B., *Kidney International* **2006,** *69* (8), 1326-1332.
193. Malik, N.; Wiwattanapatapee, R.; Klopsch, R.; Lorenz, K.; Frey, H.; Weener, J. W.; Meijer, E. W.; Paulus, W.; Duncan, R., *J. Controlled Release* **2000,** *65* (1), 133-148.
194. Luo, X.; Feng, M.; Pan, S.; Wen, Y.; Zhang, W.; Wu, C., *Journal of materials science. Materials in medicine* **2012,** *23* (7), 1685-95.
195. Chauhan, A. S.; Jain, N. K.; Diwan, P. V.; Khopade, A. J., *Journal of drug targeting* **2004,** *12* (9-10), 575-83.
196. Kaminskas, L. M.; Kelly, B. D.; McLeod, V. M.; Sberna, G.; Owen, D. J.; Boyd, B. J.; Porter, C. J., *Journal of controlled release : official journal of the Controlled Release Society* **2011,** *152* (2), 241-8.
197. Zhang, M.; Zhu, J.; Zheng, Y.; Guo, R.; Wang, S.; Mignani, S.; Caminade, A.-M.; Majoral, J.-P.; Shi, X., *Pharmaceutics* **2018,** *10* (3), 162.
198. Sherje, A. P.; Jadhav, M.; Dravyakar, B. R.; Kadam, D., *Int. J. Pharm.* **2018,** *548* (1), 707-720.
199. Mekuria, S. L.; Debele, T. A.; Tsai, H.-C., *RSC Advances* **2016,** *6* (68), 63761-63772.
200. D'Emanuele, A.; Attwood, D., *Advanced Drug Delivery Reviews* **2005,** *57* (15), 2147-2162.
201. Tekade, R. K.; Kumar, P. V.; Jain, N. K., *Chem. Rev.* **2009,** *109* (1), 49-87.
202. Devarakonda, B.; Hill, R. A.; de Villiers, M. M., *Int. J. Pharm.* **2004,** *284* (1), 133-140.
203. Hu, J.; Cheng, Y.; Ma, Y.; Wu, Q.; Xu, T., *The Journal of Physical Chemistry B* **2009,** *113* (1), 64-74.
204. Kolhe, P.; Misra, E.; Kannan, R. M.; Kannan, S.; Lieh-Lai, M., *Int. J. Pharm.* **2003,** *259* (1), 143-160.
205. Fréchet, J. M. J., *Proceedings of the National Academy of Sciences* **2002,** *99* (8), 4782.
206. Rengaraj, A.; Subbiah, B.; Haldorai, Y.; Yesudhas, D.; Yun, H. J.; Kwon, S.; Choi, S.; Han, Y.-K.; Kim, E.-S.; N, H. S.; Huh, Y. S., *RSC Advances* **2017,** *7* (9), 5046-5054.
207. Kesharwani, P.; Banerjee, S.; Gupta, U.; Mohd Amin, M. C. I.; Padhye, S.; Sarkar, F. H.; Iyer, A. K., *Mater. Today* **2015,** *18* (10), 565-572.
208. Sztandera, K.; Działak, P.; Marcinkowska, M.; Stańczyk, M.; Gorzkiewicz, M.; Janaszewska, A.; Klajnert-Maculewicz, B., *Pharm. Res.* **2019,** *36* (10), 140.
209. Zhu, S.; Hong, M.; Zhang, L.; Tang, G.; Jiang, Y.; Pei, Y., *Pharm. Res.* **2010,** *27* (1), 161-174.
210. Medina, S. H.; Tekumalla, V.; Chevliakov, M. V.; Shewach, D. S.; Ensminger, W. D.; El-Sayed, M. E. H., *Biomaterials* **2011,** *32* (17), 4118-4129.

211. Yiyun, C.; Tongwen, X.; Rongqiang, F., *European Journal of Medicinal Chemistry* **2005,** *40* (12), 1390-1393.
212. Avila-Salas, F.; Sandoval, C.; Caballero, J.; Guiñez-Molinos, S.; Santos, L. S.; Cachau, R. E.; González-Nilo, F. D., *The Journal of Physical Chemistry B* **2012,** *116* (7), 2031-2039.
213. Rajca, A.; Wang, Y.; Boska, M.; Paletta, J. T.; Olankitwanit, A.; Swanson, M. A.; Mitchell, D. G.; Eaton, S. S.; Eaton, G. R.; Rajca, S., *J. Am. Chem. Soc.* **2012,** *134* (38), 15724-15727.
214. Swanson, S. D.; Kukowska-Latallo, J. F.; Patri, A. K.; Chen, C.; Ge, S.; Cao, Z.; Kotlyar, A.; East, A. T.; Baker, J. R., *Int J Nanomedicine* **2008,** *3* (2), 201-210.
215. Gündüz, S.; Power, A.; Maier, M. E.; Logothetis, N. K.; Angelovski, G., *ChemPlusChem* **2015,** *80* (3), 612-622.
216. Gündüz, S.; Savić, T.; Pohmann, R.; Logothetis, N. K.; Scheffler, K.; Angelovski, G., *ACS Sensors* **2016,** *1* (5), 483-487.
217. Ali, M. M.; Woods, M.; Caravan, P.; Opina, A. C. L.; Spiller, M.; Fettinger, J. C.; Sherry, A. D., *Chemistry* **2008,** *14* (24), 7250-7258.
218. Kojima, C.; Turkbey, B.; Ogawa, M.; Bernardo, M.; Regino, C. A. S.; Bryant, L. H.; Choyke, P. L.; Kono, K.; Kobayashi, H., *Nanomedicine: Nanotechnology, Biology and Medicine* **2011,** *7* (6), 1001-1008.
219. Strable, E.; Bulte, J. W. M.; Moskowitz, B.; Vivekanandan, K.; Allen, M.; Douglas, T., *Chem. Mater.* **2001,** *13* (6), 2201-2209.
220. Featherstone, D. E., *ACS Chemical Neuroscience* **2010,** *1* (1), 4-12.
221. Andreae, L. C.; Burrone, J., *J. Neurosci. Res.* **2018,** *96* (3), 354-359.
222. Rizo, J., *Protein Sci.* **2018,** *27* (8), 1364-1391.
223. Savtchenko, L. P.; Rusakov, D. A., *Proceedings of the National Academy of Sciences* **2007,** *104* (6), 1823.
224. Reznikov, L. R.; Fadel, J. R.; Reagan, L. P., Glutamate-Mediated Neuroplasticity Deficits in Mood Disorders. In *Neuroplasticity: New Biochemical Mechanisms*, Costa e Silva, J. A.; Macher, J. P.; Olié, J. P., Eds. Springer Healthcare Ltd.: Tarporley, 2009; pp 13-26.
225. Siegel, J. M., *The Journal of clinical psychiatry* **2004,** *65 Suppl 16*, 4-7.
226. Zhou, Y.; Danbolt, N. C., *Journal of Neural Transmission* **2014,** *121* (8), 799-817.
227. Parsons, C. G.; Danysz, W.; Quack, G., *Drug news & perspectives* **1998,** *11* (9), 523-69.
228. Dávalos, A.; Shuaib, A.; Wahlgren, N. G., *Journal of stroke and cerebrovascular diseases : the official journal of National Stroke Association* **2000,** *9* (6 Pt 2), 2-8.
229. Clements, J. D.; Lester, R. A.; Tong, G.; Jahr, C. E.; Westbrook, G. L., *Science* **1992,** *258* (5087), 1498.
230. Dzubay, J. A.; Jahr, C. E., *The Journal of Neuroscience* **1999,** *19* (13), 5265.
231. Diamond, J. S.; Jahr, C. E., *The Journal of Neuroscience* **1997,** *17* (12), 4672.
232. Clements, J. D., *Trends in Neurosciences* **1996,** *19* (5), 163-171.
233. Cai, K.; Haris, M.; Singh, A.; Kogan, F.; Greenberg, J. H.; Hariharan, H.; Detre, J. A.; Reddy, R., *Nature Medicine* **2012,** *18* (2), 302-306.
234. Chu, W. J.; Hetherington, H. P.; Kuzniecky, R. I.; Vaughan, J. T.; Twieg, D. B.; Faught, R. E.; Gilliam, F. G.; Hugg, J. W.; Elgavish, G. A., *Neurology* **1996,** *47* (3), 756.
235. Ward, K. M.; Aletras, A. H.; Balaban, R. S., *Journal of Magnetic Resonance* **2000,** *143* (1), 79-87.
236. Henkelman, R. M.; Stanisz, G. J.; Graham, S. J., *NMR Biomed.* **2001,** *14* (2), 57-64.
237. Zhou, R.; Bagga, P.; Nath, K.; Hariharan, H.; Mankoff, D. A.; Reddy, R., *Cancer Research* **2018,** *78* (19), 5521.
238. Crescenzi, R.; DeBrosse, C.; Nanga, R. P. R.; Reddy, S.; Haris, M.; Hariharan, H.; Iba, M.; Lee, V. M. Y.; Detre, J. A.; Borthakur, A.; Reddy, R., *NeuroImage* **2014,** *101*, 185-192.
239. Davis, K. A.; Nanga, R. P. R.; Das, S.; Chen, S. H.; Hadar, P. N.; Pollard, J. R.; Lucas, T. H.; Shinohara, R. T.; Litt, B.; Hariharan, H.; Elliott, M. A.; Detre, J. A.; Reddy, R., *Science Translational Medicine* **2015,** *7* (309), 309ra161.
240. Mao, Y.; Zhuang, Z.; Chen, Y.; Zhang, X.; Shen, Y.; Lin, G.; Wu, R., *Quantitative imaging in medicine and surgery* **2019,** *9* (10), 1652-1663.
241. Haris, M.; Nath, K.; Cai, K.; Singh, A.; Crescenzi, R.; Kogan, F.; Verma, G.; Reddy, S.; Hariharan, H.; Melhem, E. R.; Reddy, R., *NMR Biomed.* **2013,** *26* (4), 386-391.
242. Roalf, D. R.; Nanga, R. P. R.; Rupert, P. E.; Hariharan, H.; Quarmley, M.; Calkins, M. E.; Dress, E.; Prabhakaran, K.; Elliott, M. A.; Moberg, P. J.; Gur, R. C.; Gur, R. E.; Reddy, R.; Turetsky, B. I., *Molecular Psychiatry* **2017,** *22* (9), 1298-1305.
243. Pépin, J.; Francelle, L.; Carrillo-de Sauvage, M.-A.; de Longprez, L.; Gipchtein, P.; Cambon, K.; Valette, J.; Brouillet, E.; Flament, J., *NeuroImage* **2016,** *139*, 53-64.

244. Yan, G.; Zhang, T.; Dai, Z.; Yi, M.; Jia, Y.; Nie, T.; Zhang, H.; Xiao, G.; Wu, R., *PLOS ONE* **2016,** *11* (10), e0163765.
245. Bagga, P.; Crescenzi, R.; Krishnamoorthy, G.; Verma, G.; Nanga, R. P. R.; Reddy, D.; Greenberg, J.; Detre, J. A.; Hariharan, H.; Reddy, R., *J. Neurochem.* **2016,** *139* (3), 432-439.
246. Bagga, P.; Pickup, S.; Crescenzi, R.; Martinez, D.; Borthakur, A.; D'Aquilla, K.; Singh, A.; Verma, G.; Detre, J. A.; Greenberg, J.; Hariharan, H.; Reddy, R., *Scientific Reports* **2018,** *8* (1), 2883.
247. Ren, J.; Sherry, A. D.; Malloy, C. R., *NMR Biomed.* **2015,** *28* (11), 1455-1462.
248. Lai, M.; Lanz, B.; Poitry-Yamate, C.; Romero, J. F.; Berset, C. M.; Cudalbu, C.; Gruetter, R., *J Cereb Blood Flow Metab* **2018,** *38* (10), 1701-1714.
249. Wijtenburg, S. A.; Yang, S.; Fischer, B. A.; Rowland, L. M., *Neurosci Biobehav Rev* **2015,** *51*, 276-295.
250. Fitzpatrick, S. M.; Hetherington Hp Fau - Behar, K. L.; Behar Kl Fau - Shulman, R. G.; Shulman, R. G., (0271-678X (Print)).
251. Ramadan, S.; Lin, A.; Stanwell, P., *NMR Biomed.* **2013,** *26* (12), 1630-1646.
252. Barboiu, M. D.; Hovnanian, N. D.; Luca, C.; Cot, L., *Tetrahedron* **1999,** *55* (30), 9221-9232.
253. Wu, X.; Busschaert, N.; Wells, N. J.; Jiang, Y.-B.; Gale, P. A., *J. Am. Chem. Soc.* **2015,** *137* (4), 1476-1484.
254. Ryu, D.; Park, E.; Kim, D.-S.; Yan, S.; Lee, J. Y.; Chang, B.-Y.; Ahn, K. H., *J. Am. Chem. Soc.* **2008,** *130* (8), 2394-2395.
255. Nonokawa, R.; Yashima, E., *J. Am. Chem. Soc.* **2003,** *125* (5), 1278-1283.
256. Bernier, N.; Esteves, C. V.; Delgado, R., *Tetrahedron* **2012,** *68* (24), 4860-4868.
257. Aït-Haddou, H.; Wiskur, S. L.; Lynch, V. M.; Anslyn, E. V., *J. Am. Chem. Soc.* **2001,** *123* (45), 11296-11297.
258. Severin, K.; Bergs, R.; Beck, W., *Angew. Chem. Int. Ed.* **1998,** *37* (12), 1634-1654.
259. Mishra, A.; Gottschalk, S.; Engelmann, J.; Parker, D., *Chemical Science* **2012,** *3* (1), 131-135.
260. Gottschalk, S.; Engelmann, J.; Rolla, G. A.; Botta, M.; Parker, D.; Mishra, A., *Organic & Biomolecular Chemistry* **2013,** *11* (36), 6131-6141.
261. Laruelle, M., *Journal of Cerebral Blood Flow & Metabolism* **2000,** *20* (3), 423-451.
262. Mishra, A.; Mishra, R.; Gottschalk, S.; Pal, R.; Sim, N.; Engelmann, J.; Goldberg, M.; Parker, D., *ACS Chemical Neuroscience* **2014,** *5* (2), 128-137.
263. Sim, N.; Pal, R.; Parker, D.; Engelmann, J.; Mishra, A.; Gottschalk, S., *Organic & Biomolecular Chemistry* **2014,** *12* (46), 9389-9404.
264. Oukhatar, F.; Eliseeva, S. A.-O.; Bonnet, C. A.-O.; Placidi, M.; Logothetis, N. K.; Petoud, S. A.-O.; Angelovski, G. A.-O.; Tóth É, A.-O., (1520-510X (Electronic)).
265. Lewerenz, J.; Maher, P., *Frontiers in Neuroscience* **2015,** *9*, 469.
266. Dingledine, R.; Varvel, N. H.; Dudek, F. E., *Adv Exp Med Biol* **2014,** *813*, 109-122.
267. Rothman, D. L.; De Feyter, H. M.; de Graaf, R. A.; Mason, G. F.; Behar, K. L., *NMR Biomed.* **2011,** *24* (8), 943-957.
268. Fischman, A. J.; Alpert, N. M.; Rubin, R. H., *Clin Pharmacokinet* **2002,** *41* (8), 581-602.
269. Hingorani, D. V.; Bernstein, A. S.; Pagel, M. D., *Contrast Media Mol Imaging* **2015,** *10* (4), 245-65.
270. Oukhatar , F.; Meudal, H.; Landon, C.; Logothetis , N. K.; Platas-Iglesias, C.; Angelovski, G.; Tóth, É., *Chemistry – A European Journal* **2015,** *21* (31), 11226-11237.
271. Oukhatar, F.; Même, S.; Même, W.; Szeremeta, F.; Logothetis, N. K.; Angelovski, G.; Tóth, É., *ACS Chemical Neuroscience* **2015,** *6* (2), 219-225.
272. Machitani, K.; Sakamoto, H.; Nakahara, Y.; Kimura, K., *Anal. Sci.* **2008,** *24* (4), 463-469.
273. Gündüz, S.; Nitta, N.; Vibhute, S.; Shibata, S.; Mayer, M. E.; Logothetis, N. K.; Aoki, I.; Angelovski, G., *Chem. Commun.* **2015,** *51* (14), 2782-2785.
274. Kovacs, Z.; Sherry, A. D., *Synthesis* **1997,** *1997* (07), 759-763.
275. Maggini, L.; Toma, F. M.; Feruglio, L.; Malicka, J. M.; Da Ros, T.; Armaroli, N.; Prato, M.; Bonifazi, D., *Chemistry – A European Journal* **2012,** *18* (19), 5889-5897.
276. Binnemans, K., *Coord. Chem. Rev.* **2015,** *295*, 1-45.
277. Morrow, J. R.; Dorazio, S. J., *Luminescence of Lanthanide Ions in Coordination Compounds and Nanomaterials* **2014**, 303-330.
278. Ligner, G.; Mohan, R.; Knittel, S.; Duportail, G., *Spectrochimica Acta Part A: Molecular Spectroscopy* **1990,** *46* (5), 797-802.
279. Morris, K. F.; Johnson, C. S., *J. Am. Chem. Soc.* **1992,** *114* (8), 3139-3141.
280. Morris, K. F.; Stilbs, P.; Johnson, C. S., *Anal. Chem.* **1994,** *66* (2), 211-215.
281. Natrajan, L. S.; Timmins, P. L.; Lunn, M.; Heath, S. L., *Inorg. Chem.* **2007,** *46* (25), 10877-10886.

282. Denis-Quanquin, S.; Riobé, F.; Delsuc, M.-A.; Maury, O.; Giraud, N., *Chemistry – A European Journal* **2016,** *22* (50), 18123-18131.
283. Esteban-Gómez, D.; de Blas, A.; Rodríguez-Blas, T.; Helm, L.; Platas-Iglesias, C., *ChemPhysChem* **2012,** *13* (16), 3640-3650.
284. Regueiro-Figueroa, M.; Platas-Iglesias, C., *The Journal of Physical Chemistry A* **2015,** *119* (24), 6436-6445.
285. Dominy, B. N., *Curr Pharm Biotechnol* **2008,** *9* (2), 87-95.
286. Albert, J. S.; Goodman, M. S.; Hamilton, A. D., *J. Am. Chem. Soc.* **1995,** *117* (3), 1143-1144.
287. Zhong, Z.; Li, X.; Zhao, Y., *J. Am. Chem. Soc.* **2011,** *133* (23), 8862-8865.
288. Okada, S.; Mizukami, S.; Sakata, T.; Matsumura, Y.; Yoshioka, Y.; Kikuchi, K., **2014,** *26* (19), 2989-2992.
289. Barge, A.; Botta, M.; Parker, D.; Puschmann, H., *Chem. Commun.* **2003,** (12), 1386-1387.
290. Barge, A.; Cravotto, G.; Gianolio, E.; Fedeli, F., *Contrast Media & Molecular Imaging* **2006,** *1* (5), 184-188.
291. Bang, E.; Jung, J.-W.; Lee, W.; Lee, D. W.; Lee, W., *Journal of the Chemical Society, Perkin Transactions 2* **2001,** (9), 1685-1692.
292. Ciardi, M.; Galán, A.; Ballester, P., *J. Am. Chem. Soc.* **2015,** *137* (5), 2047-2055.
293. Nierengarten, J.-F.; Hahn, U.; Duarte, T. M. F.; Cardinali, F.; Solladié, N.; Walther, M. E.; Van Dorsselaer, A.; Herschbach, H.; Leize, E.; Albrecht-Gary, A.-M.; Trabolsi, A.; Elhabiri, M., *Comptes Rendus Chimie* **2006,** *9* (7), 1022-1030.
294. Butler, S. J.; Parker, D., *Chem. Soc. Rev.* **2013,** *42* (4), 1652-1666.
295. M. P. Lima, L.; Tripier, R., *Current Inorganic Chemistry* **2011,** *1* (1), 36-60.
296. Mariappan, S. V. S.; Gomathi, L.; Subramanian, S., *Magn. Reson. Chem.* **1991,** *29* (7), 656-666.
297. Kleinpeter, E.; Starke, I.; Ströhl, D.; Holdt, H. J., *J. Mol. Struct.* **1997,** *404* (3), 273-290.
298. Rüdiger, V.; Schneider, H.-J.; Solov'ev, V. P.; Kazachenko, V. P.; Raevsky, O. A., *Eur. J. Org. Chem.* **1999,** *1999* (8), 1847-1856.
299. Späth, A.; König, B., *Beilstein Journal of Organic Chemistry* **2010,** *6*, 32.
300. Pagès, G.; Gilard, V.; Martino, R.; Malet-Martino, M., *Analyst* **2017,** *142* (20), 3771-3796.
301. Scheffler, K., *Magnetic Resonance in Medicine* **2003,** *49* (4), 781-783.
302. Xing, P.; Zhao, Y., *Adv. Mater.* **2016,** *28* (34), 7304-7339.
303. Hisataka, K.; Martin, W. B., *Current Pharmaceutical Biotechnology* **2004,** *5* (6), 539-549.
304. Cheon, J.; Lee, J.-H., *Acc. Chem. Res.* **2008,** *41* (12), 1630-1640.
305. Bumb, A.; Brechbiel, M. W.; Choyke, P., *Acta Radiol* **2010,** *51* (7), 751-767.
306. Sun, C.; Lin, H.; Gong, X.; Yang, Z.; Mo, Y.; Chen, X.; Gao, J., *J. Am. Chem. Soc.* **2020,** *142* (1), 198-206.
307. Maingi, V.; Kumar, M. V. S.; Maiti, P. K., *The Journal of Physical Chemistry B* **2012,** *116* (14), 4370-4376.
308. Michelle, L.; Peter, L. C.; Hisataka, K., *Curr. Top. Med. Chem.* **2008,** *8* (14), 1180-1186.
309. Bhuiyan, M. P. I.; Aryal, M. P.; Janic, B.; Karki, K.; Varma, N. R. S.; Ewing, J. R.; Arbab, A. S.; Ali, M. M., *Contrast Media & Molecular Imaging* **2015,** *10* (6), 481-486.
310. Aime, S.; Caravan, P., *Journal of Magnetic Resonance Imaging* **2009,** *30* (6), 1259-1267.
311. Lancelot, E., *Invest Radiol* **2016,** *51* (11).
312. Abraham, J. L.; Thakral, C., *European journal of radiology* **2008,** *66* (2), 200-207.
313. Wiener, E.; Brechbiel, M. W.; Brothers, H.; Magin, R. L.; Gansow, O. A.; Tomalia, D. A.; Lauterbur, P. C., *Magnetic Resonance in Medicine* **1994,** *31* (1), 1-8.
314. Adam, G.; Neuerburg, J.; Spüntrup, E.; Mühler, A.; Scherer, K.; Günther, R. W., *Magnetic Resonance in Medicine* **1994,** *32* (5), 622-628.
315. Sunil Kumar, D.; Shubham, S.; Mukta, A.; Maithili, K.; Gautam, S.; Sanjay, T.; Swarnlata, S.; Shailendra, S.; Amit, A., *Current Drug Targets* **2020,** *21* (6), 528-540.
316. Labieniec-Watala, M.; Watala, C., *J. Pharm. Sci.* **2015,** *104* (1), 2-14.
317. Singh, A. K.; Gothwal, A.; Rani, S.; Rana, M.; Sharma, A. K.; Yadav, A. K.; Gupta, U., *ACS Omega* **2019,** *4* (3), 4519-4529.
318. Ciolkowski, M.; Petersen, J. F.; Ficker, M.; Janaszewska, A.; Christensen, J. B.; Klajnert, B.; Bryszewska, M., *Nanomedicine: Nanotechnology, Biology and Medicine* **2012,** *8* (6), 815-817.
319. Lowe, M. P.; Parker, D.; Reany, O.; Aime, S.; Botta, M.; Castellano, G.; Gianolio, E.; Pagliarin, R., *J. Am. Chem. Soc.* **2001,** *123* (31), 7601-7609.
320. Fox, L. J.; Richardson, R. M.; Briscoe, W. H., *Adv. Colloid Interface Sci.* **2018,** *257*, 1-18.
321. Luong, D.; Kesharwani, P.; Deshmukh, R.; Mohd Amin, M. C. I.; Gupta, U.; Greish, K.; Iyer, A. K., *Acta Biomaterialia* **2016,** *43*, 14-29.

322. Amir, R. J.; Pessah, N.; Shamis, M.; Shabat, D., *Angew. Chem. Int. Ed.* **2003,** *42* (37), 4494-4499.
323. Jevprasesphant, R.; Penny, J.; Jalal, R.; Attwood, D.; McKeown, N. B.; D'Emanuele, A., *Int. J. Pharm.* **2003,** *252* (1), 263-266.
324. Caravan, P., *Chem. Soc. Rev.* **2006,** *35* (6), 512-523.
325. Gunduz, S.; Savic, T.; Toljic, D.; Angelovski, G., *J Vis Exp* **2016,** (118), e54776.
326. Khopade, A. J.; Caruso, F.; Tripathi, P.; Nagaich, S.; Jain, N. K., *International Journal of Pharmaceutics* **2002,** *232* (1), 157-162.
327. Zhang, Z.-Y.; Smith, B. D., *Bioconjugate Chemistry* **2000,** *11* (6), 805-814.
328. Zeng, F.; Zimmerman, S. C., *Chem. Rev.* **1997,** *97* (5), 1681-1712.
329. Nwe, K.; Bryant, L. H.; Brechbiel, M. W., *Bioconjugate Chem.* **2010,** *21* (6), 1014-1017.
330. Kurhanewicz, J.; Bok, R.; Nelson, S. J.; Vigneron, D. B., *Journal of nuclear medicine : official publication, Society of Nuclear Medicine* **2008,** *49* (3), 341-4.
331. Sonnay, S.; Gruetter, R.; Duarte, J. M. N., *Frontiers in Neuroscience* **2017,** *11*, 288.
332. Wijtenburg, S. A.; Yang, S.; Fischer, B. A.; Rowland, L. M., *Neuroscience & Biobehavioral Reviews* **2015,** *51*, 276-295.
333. Lerma, J.; Herranz, A. S.; Herreras, O.; Abraira, V.; del Rio, R. M., *Brain Research* **1986,** *384* (1), 145-155.
334. Baker, D. A.; Xi, Z.-X.; Shen, H.; Swanson, C. J.; Kalivas, P. W., *The Journal of Neuroscience* **2002,** *22* (20), 9134.
335. Schubert, F.; Gallinat, J.; Seifert, F.; Rinneberg, H., *NeuroImage* **2004,** *21* (4), 1762-1771.
336. Jang, D.-P.; Lee, J.-M.; Lee, E.; Park, S.; Kim, J.-J.; Namkoong, K.; Yoon, K.-J.; Kim, I.-Y.; Kim, S. I., *Magnetic Resonance in Medicine* **2005,** *53* (3), 708-712.
337. Mullins, P. G.; Chen, H.; Xu, J.; Caprihan, A.; Gasparovic, C., *Magnetic Resonance in Medicine* **2008,** *60* (4), 964-969.
338. Armitage, I.; Campbell, J. R.; Hall, L. D., *Can. J. Chem.* **1972,** *50* (13), 2139-2141.
339. Ross, B.; Lin, A.; Harris, K.; Bhattacharya, P.; Schweinsburg, B., *NMR Biomed.* **2003,** *16* (6-7), 358-369.
340. Müntener, T.; Kottelat, J.; Huber, A.; Häussinger, D., *Bioconjugate Chem.* **2018,** *29* (10), 3344-3351.
341. Ravera, E.; Parigi, G.; Luchinat, C., *Journal of Magnetic Resonance* **2017,** *282*, 154-169.
342. Lee, M. D.; Dennis, M. L.; Swarbrick, J. D.; Graham, B., *Chem. Commun.* **2016,** *52* (51), 7954-7957.
343. Pan, B.-B.; Yang, F.; Ye, Y.; Wu, Q.; Li, C.; Huber, T.; Su, X.-C., *Chem. Commun.* **2016,** *52* (67), 10237-10240.
344. Coman, D.; Trubel, H. K.; Hyder, F., *NMR Biomed.* **2010,** *23* (3), 277-285.
345. Senanayake, P. K.; Rogers, N. J.; Finney, K.-L. N. A.; Harvey, P.; Funk, A. M.; Wilson, J. I.; O'Hogain, D.; Maxwell, R.; Parker, D.; Blamire, A. M., *Magnetic Resonance in Medicine* **2017,** *77* (3), 1307-1317.
346. Chalmers, K. H.; Kenwright, A. M.; Parker, D.; Blamire, A. M., *Magnetic Resonance in Medicine* **2011,** *66* (4), 931-936.
347. Zuo, C. S.; Metz, K. R.; Sun, Y.; Sherry, A. D., *J Magn Reson* **1998,** *133* (1), 53-60.
348. Kainosho, M.; Ajisaka, K.; Tori, K., *Chem. Lett.* **1972,** *1* (11), 1061-1064.
349. Gansow, O. A.; Loeffler, P. A.; Davis, R. E.; Willcott, M. R.; Lenkinsk, R. E., *J. Am. Chem. Soc.* **1973,** *95* (10), 3390-3392.
350. Pearson, R. G., *J. Am. Chem. Soc.* **1963,** *85* (22), 3533-3539.
351. Carubelli, C. R.; Massabni, A. M. G.; Leite, S. R. d. A., *Journal of the Brazilian Chemical Society* **1997,** *8*, 597-602.
352. Morishima, I.; Yonezawa, T.; Goto, K., *J. Am. Chem. Soc.* **1970,** *92* (22), 6651-6653.
353. Morishima, I.; Okada, K.; Yonezawa, T., *J. Am. Chem. Soc.* **1972,** *94* (5), 1425-1430.
354. Harvey, P.; Blamire, A. M.; Wilson, J. I.; Finney, K.-L. N. A.; Funk, A. M.; Senanayake, P. K.; Parker, D., *Chemical Science* **2013,** *4* (11), 4251-4258.
355. von Ammon, R.; Fischer, R. D., *Angewandte Chemie International Edition in English* **1972,** *11* (8), 675-692.
356. Corsi, D. M.; Platas-Iglesias, C.; Bekkum, H. v.; Peters, J. A., *Magn. Reson. Chem.* **2001,** *39* (11), 723-726.
357. Tao, J.; Perdew, J. P.; Staroverov, V. N.; Scuseria, G. E., *Phys. Rev. Lett.* **2003,** *91* (14), 146401.
358. Dolg, M.; Stoll, H.; Savin, A.; Preuss, H., *Theoretica chimica acta* **1989,** *75* (3), 173-194.
359. Tomasi, J.; Mennucci, B.; Cammi, R., *Chem. Rev.* **2005,** *105* (8), 2999-3094.
360. Brilliantov, N. V.; Denisov, V. P.; Krapivsky, P. L., *Physica A: Statistical Mechanics and its Applications* **1991,** *175* (2), 293-304.

361. Mazza, M. G.; Giovambattista, N.; Stanley, H. E.; Starr, F. W., *Physical Review E* **2007,** *76* (3), 031203.